Additive Manufacturing of Fatigue Resistant Austenitic Stainless Steels by Establishing the Process-Structure-Property Relationships

by

Jonathan W. Pegues

A dissertation submitted to the Graduate Faculty of
Auburn University
in partial fulfillment of the
requirements for the Degree of
Doctor of Philosophy

Auburn, Alabama
Dec 14, 2019

Keywords: Additive manufacturing, Crack initiation, Fatigue resistance, Austenitic stainless steels, Failure analysis, Microstructural analysis

Copyright 2019 by Jonathan W. Pegues

Approved by

Nima Shamsaei, Chair, Philpott-WestPoint Stevens Distinguished Associate Professor
Michael D. Roach, Associate Professor
Haresh V. Tippur, McWane Professor & Associate Chair for Graduate Studies
Michael Bozack, Emeritus Professor

Abstract

This work presents a multidisciplinary approach (relating microstructure features to mechanical properties) to utilize additive manufacturing as a tool to fabricate superior, fatigue resistant materials. The ultimate goal of the study was to establish the Process-Structure-Property relationships of an additive manufactured 304L stainless steel to determine if and how material can be tailored to enhance mechanical properties by controlling their microstructural grain size, orientations, and crystalline texture during their manufacture. The research centers on a unique ex-situ microstructural characterization technique to inform material selection and fabrication process to avoid the typical failure mechanisms associated with the material. Microstructural traits and their relationships to crack initiation and microstructurally short crack growth of the wrought and additive manufactured material is evaluated by optical and scanning electron microscopy, x-ray diffraction, and electron backscatter diffraction on representative samples as well as fatigue specimens through a systematic ex-situ experimental characterization process. The Process-Structure-Property relationships were established by correlating the resulting microstructural features to the material's mechanical properties before, during, and after fatigue testing. It was shown that austenitic stainless steels such as 304L possess certain characteristics that allow their fabrication through laser beam powder bed fusion, while minimizing the failure mechanisms associated with these alloys. The fatigue resistance of the additive manufactured material in the stress relieved condition was thus shown to be superior to the conventionally processed wrought material. Traditional solution annealing treatments, however, were shown to be detrimental to the additive manufactured material as they resulted in the crack initiation to shift from microstructural features, such as annealing twin and high angle grain boundaries, to process induced defects. These

profound results suggest that by understanding the Process-Structure-Property relationships additive manufacturing can be leveraged to fabricate materials with improved microstructures capable of enhancing their mechanical performance. Results from this study have progressed the understanding of additive manufactured 304L stainless steel by providing (i) the relationships between AM process and post-process conditions and eventual microstructural morphology/orientation, (ii) characterization of the insufficiently-documented fatigue resistance of AM materials, and (iii) a unique experimental approach for advanced understanding of the microstructure-property relationships that has, thus far, been camouflaged by the effects of process-induced defects.

Table of Contents

List of Tables

List of Illustrations

List of Abbreviations

2θ	Diffraction angle
2c	Crack length
a	Lattice parameter
c	Crack depth
d	d-spacing
H_s	Cyclic secondary hardening
M_s	Martensite start temperature
M_d	Martensite transformation limiting temperature
M_{d30}	Martensite thirty temperature
N, 2N	Cycles, Reversals
N_f, $2N_f$	Cycles to failure, Reversals to failure
R_ε	Strain ratio
T	Temperature
T_e	Equilibrium temperature
α’	Martensite (BCC) phase
$\frac{da}{dN}$	Microstructurally short crack growth rate
$\frac{d(\Delta\sigma/2)}{d(2N)}$	Secondary hardening rate
ε_a, $\Delta\varepsilon/2$	Strain amplitude
$\dot{\varepsilon}$	Strain rate

γ	Austenite (FCC) phase
$\Delta 2c$	Change in crack length
$\Delta\varepsilon_p/2$	Plastic strain amplitude
ΔG^*	Critical free energy barrier
$\Delta\sigma/2$	Stress amplitude
ΔT	Undercooling temperature
ΔT_s	Undercooling at martensite start temperature
Σ	Coincident site lattice relationship
$\Sigma 3-TB$	Sigma 3 type coincident site lattice
BCC	Body centered cubic
EBSD	Electron backscatter diffraction
FCC	Face centered cubic
GB	Grain boundary initiation feature
HCP	Hexagonal close packed
HIP	Hot isostatic pressing
IN	Inclusion initiation feature
IPF	Inverse pole figure
M	Martensite initiation feature
MM	Medium-medium mismatch
MH	Medium-high mismatch

MSC	Microstrucurally short crack
RT	Room temperature
SB	Slip band initiation feature
SEM	Scanning electron microscopy
SFM	Schmid factor mismatch
SGFS	Square gage fatigue specimen
SFE	Stacking fault energy
TFM	Taylor factor mismatch
TW	Twin boundary initiation feature
UEL	Ultimate uniform elongation
UTS	Ultimate tensile strength
XRD	X-ray diffraction

Chapter 1: Introduction and Dissertation Layout

This dissertation includes the compilation of several works which have passed rigorous peer review processes in respected journals. The purpose of this introduction section is to provide background information and the direction of the resulting works.

Additive manufacturing (AM) promises a revolution in the fabrication process of structural components in a variety of industries including aerospace, biomedical, defense, nuclear, and automotive. A process in which material is fabricated track-by-track and layer-by-layer, additive manufacturing offers many freedoms that are not available through traditional manufacturing processes. Its layer-by-layer joining process enables a wide design space with the ability to fabricate highly complex geometries and, arguably more importantly, the ability to control the localized thermal history [1, 2].

AM techniques can be classified based on either the energy source or feedstock, i.e. laser beam versus electron beam and/or powder versus wire. The laser-based systems are the most prevalent ones in industry with the two most common techniques being laser beam powder bed fusion (LB-PBF) and laser beam directed energy deposition (LB-DED). The main difference between these two systems is the method to deliver powder to the build area. The LB-PBF process uses a powder bed with a rake, and feed/build elevators to continuously lower the build platform, raise the feedstock, and spread the new powder layer over the bed. The laser beam then scans across the selected area to fuse the newly dispersed powder (i.e. create a melt pool) to the previously fused layer (i.e. the part). On the other hand, LB-DED uses a laser beam to create the melt pool while simultaneously adding powder through flow nozzles adjacent to the laser head. The substrate is moved through a computer numerical control (CNC) table system to adjust the part in relation to

the laser while the laser head adjusts its position based on the height of the build. In general, the LB-PBF systems have much finer resolution and are capable of creating much more complex parts, while the LB-DED systems are more suited for large scale parts and often require post-process machining to acquire the final desired shape.

1.1 Motivation

Although AM has seen a surge of interest over the last decade, the acceptance of this technology for fatigue critical parts has been hindered by the effects of process induced defects such as surface roughness, lack of fusion (LoF), and entrapped gas porosity. These defects act as stress concentrators inducing early fatigue life crack initiation, which severely limits the potential for producing reliable, fatigue resistant AM parts. The fatigue behavior of several popular materials, in machined and polished surface conditions, fabricated via both LB-PBF and LB-DED is compared with that of wrought counterparts in Figure 1 [3-5]. Regardless of the AM method employed, the additively produced materials possess lower fatigue resistance as compared to the wrought counterparts due to the process induced defects.

One of the most exciting aspects of AM is the ability to control the thermal history in order to tailor the microstructure in specific regions. This can help to improve the mechanical behavior in critical locations that may be more susceptible to early life fatigue crack initiation, i.e. regions with high stress concentrations. The microstructure of AM materials is intimately related to the thermal history experienced by the part during fabrication, which can be adjusted by manipulating the process parameters associated with AM fabrication. Several studies have shown that adjusting the most common process parameters (e.g. laser power, scan speed, hatch distance, and layer thickness) can result in measurable changes in the microstructure, i.e. grain size, secondary phases,

etc. [6-8]. Accordingly, this ability to essentially control the thermal history, combined with the layer-by-layer fabrication method leads to the possibility of creating functionally graded materials with improved microstructure in critical locations. For instance, the process parameters could be adjusted at locations near stress concentrations, such as holes or notches, to obtain higher cooling rates. This produces finer microstructure adjacent to such critical regions leading to higher localized strength and less susceptibility to crack initiation. Moving away from the critical area, a coarse microstructure may be preferred to improve crack growth resistance. Therefore, process parameters that lower the cooling rate and promote coarser microstructure could be used to functionally grade the microstructure. However, as the process induced defects dominate the fatigue behavior, any development on functionally graded microstructures may not be beneficial.

Austenitic stainless steel (SS) alloys have been shown to be more sensitive to microstructure than defects such as inclusions in wrought materials [9, 10], making them a prime candidate to study how additive manufacturing can be leveraged to create parts with improved fatigue resistance. Two of the most common austenitic stainless steels are 304L and 316L which are used extensively in the biomedical, nuclear, chemical, construction, and automotive industries [11, 12]. Previous research has shown that both of these austenitic stainless steels are susceptible to crack initiation at annealing twins [13-19]. Though annealing twin boundaries are coherent and low energy, the interaction between the slip bands and the boundary results in ledges along the boundary that are not coherent, facilitating secondary slip systems and dislocation sources creating plastic incompatibilities along the boundary [20]. This interaction of the persistent slip bands (PSBs) and the twin boundaries results in preferred crack initiation sites along twin boundaries in many face centered cubic (FCC) materials [14]. Control of annealing twins has thus been suggested as a means to improve the resistance to crack initiation in 304LSS [15], however, controlling the

microstructure to this extent is difficult through traditional manufacturing processes [21, 22]. In addition, the microstructure in austenitic stainless steels can become sensitized at temperatures between 425 to 870°C such that the corrosion resistance is reduced by depleting the Cr content in localized areas [12]. To avoid sensitization these steels are either supplied in the cold worked or solution annealed condition [23, 24]. Although, cold working is the most common way to strengthen these alloys, the improvement in strength coincides with a decrease in ductility such that, after cold working, the material is often annealed, resulting in a high density of annealing twins in the microstructure [25].

As mentioned previously, AM offers the opportunity to produce net shaped or near net shaped parts without the need for post processing heat treatment, such as the annealing step required for most austenitic stainless steels [26]. Austenitic stainless steels have exceptional high temperature properties and good weldability, and therefore, are prime candidate materials for use in additive manufacturing systems [27, 28]. Both 304LSS and 316L SS have been implemented in LB-PBF and LB-DED AM systems, however, very little work has been done to characterize the microstructure and its effects on the performance of these alloys, specifically under cyclic loading. While LB-DED can result in sensitization of austenitic stainless steels, the cooling rates associated with LB-PBF process results in minimal time to cool down to below the sensitization temperature range of these stainless steels and are therefore less susceptible to sensitization in the as-fabricated condition [29]. These facts lead to the hypothesis that, for the case of 304L and 316L alloys, LB-PBF can offer the opportunity to fabricate net shaped parts, avoiding the common crack initiation features, and thus, achieving an improved fatigue resistance compared to their wrought counterparts.

This study aims to better understand how localized thermal input control (process parameters) can be utilized to tailor the microstructure and improve the fatigue resistance of AM materials. Two austenitic stainless steels will be fabricated by LB-PBF, taking advantage of the high cooling rate to fabricate a microstructure that is more resistant to fatigue crack initiation. The knowledge gained by studying materials that are less sensitive to process induced defects can then be used to tailor microstructures that are more resistant to fatigue crack initiation despite the presence of process induced defects.

1.2 Objectives

The objectives of this research are to establish the process-structure-property relationships of 304LSS and 316L SS fabricated by LB-PBF as they are related to fatigue resistance and, in particular, fatigue crack initiation. Completion of these objectives will test the central hypothesis and establish the effect of processing and post-processing parameters on the microstructural features responsible for crack initiation and the resulting fatigue failure under uniaxial cyclic loading.

1. The first objective is to establish the structure-property relationships of a wrought austenitic stainless steel as baseline data for the proposed research. The microstructural effects on the uniaxial fatigue behavior of austenitic stainless steels can be readily captured through a systematic experimental investigation of the cyclic deformation behavior of 304LSS.

   Hypothesis 1a: The fatigue behavior of austenitic stainless steels is more sensitive to microstructural features such as grain/twin boundaries, persistent slip bands, and secondary phases than defects such as intermetallic inclusions.

2. The second objective is to establish the process-structure relationships of 304L and 316L SS alloys fabricated by LB-PBF. The effect of both processing and post-processing parameters on the

resulting microstructure will be evaluated. In particular, the energy density (i.e. process) and thermal treatments (i.e. post-process) will be investigated.

Hypothesis 2a: The as-fabricated microstructure of LB-PBF austenitic stainless steels will contain minimal Σ3 boundaries as a result of the high cooling rates.

Hypothesis 2b: Thermal treatments such as solution annealing can be used to recover the AM microstructure to that of the wrought counterpart.

3. The third objective aims to understand the deformation behavior of LB-PBF 304LSS and 316L SS under both force- and strain-controlled fatigue loading. The effect of process induced defects, surface condition, and thermal treatment will all be considered to firmly establish the static and dynamic mechanical properties of both alloys.

   Hypothesis 3a: The cyclic mechanical properties of the LB-PBF material in the machined/polished and as-fabricated thermal treatment condition will be improved as compared to that of the wrought counterpart.

   Hypothesis 3b: The improvement in cyclic mechanical properties will become more comparable to the wrought counterpart's properties for the specimens that undergo thermal treatments.

4. The final objective is to establish the structure-property relationships of the LB-PBF 304 and 316L SS alloys through systematic experimental investigation to the crack initiation and microstructurally short crack growth behavior.

   Hypothesis 4a: The crack initiation mechanisms of LB-PBF will be similar to that of the wrought counterparts, however, the shortage of such mechanisms in the microstructure of LB-PBF materials will result in their improved fatigue resistance.

1.3 Outline of Dissertation

The understanding of how materials fail is not a new endeavor rooted in the advancement of additive manufacturing processes. Researchers since the early 1800's have been studying the failures of metals at stresses well below their yield strengths. The challenge in additive manufacturing is applying our understanding of microstructural effects on the deformation and failure of materials with unique microstructural characteristics and defect distributions. This work addresses these challenges by first closing some knowledge gaps associated with the cyclic deformation behavior of wrought 304LSS which can show much different failure mechanisms than most engineering alloys. While the study of mechanical failure of additively manufactured materials is relatively new, the effect of detrimental microstructural features and porosity has been extensively studied [30]. In general, most metals fail under high cycle fatigue loading due to the presence of inclusions or pores that were not completely healed during the working stage. For metastable materials such as 304LSS, the failure mechanisms associated with crack initiation and crack growth can be complicated by the deformation induced martensite transformation (DIMT) from the face centered cubic structure of austenite (γ) phase to the body centered cubic martensite (α') phase. This DIMT results in a complex deformation behavior under both static and cyclic loading.

To understand the process-structure-property relationships of LB-PBF 304LSS, it is imperative to first understand the structure-property relationships of traditionally manufactured material. Chapter 2 investigates the relationship between multiple loading conditions including cyclic strain rate effects and mean strain on the DIMT behavior and the resulting fatigue performance of a commercially available wrought 304LSS material. The purpose of this chapter is to lay the foundation for experimental methods in the following chapters to ensure the results

successfully capture the failure mechanisms associated with this material and are consistent throughout the study.

Chapter 3 continues the investigation on the commercially available wrought 304LSS material by targeting the fatigue crack initiation (FCI) mechanisms responsible for cyclic failure. This chapter introduces an ex-situ experimental approach to capture the microstructural effects on FCI and microstructurally short crack growth using non-standard square gage specimens. This understanding of how the microstructure contributes to cyclic deformation and failure for wrought 304LSS is essential for establishing the Structure-Property relationship of LB-PBF 304LSS and how they can be leveraged during the AM process to avoid critical crack initiation features.

In Chapter 4 the initial static and cyclic behavior of the LB-PBF material is introduced for a typical AM process; fabrication, stress relief, machining, and testing. This investigation leverages the learnings from the previous chapters on the wrought material to capture and understand the cyclic deformation and crack initiation behavior of the additively manufactured material. This chapter establishes the baseline LB-PBF Structure-Property relationship for 304LSS compared to its wrought counterpart.

Chapter 5 continues building on the understanding of the Process-Structure-Property relationships for LB-PBF 304LSS by targeting the effect of common heat treatments for this material. This Chapter is critical for the LB-PBF material as it investigates a means of overcoming traditional challenges related to wrought materials, specifically in regards to strengthening mechanisms of the bulk material. As austenitic stainless steels are not particularly heat treatable, strengthening of these alloys is carried out through microstructural manipulation by applying large deformations which require additional annealing treatments to recover ductility.

In Chapter 6 the objectives and hypotheses are revisited individually to specifically relate the results discovered through the preceding chapters to the specific task/goal in the Process-Structure-Property investigations. The significance of each result is briefly summarized for each hypotheses/result combination to clearly outline the impact this work will have on the AM community.

Finally, in Chapter 7 the natural progression of this study is discussed to steer continued development in the Process-Structure-Property relationships of this material. Some suggested directions and significance of the expected discoveries and impacts on the technical communities are summarized.

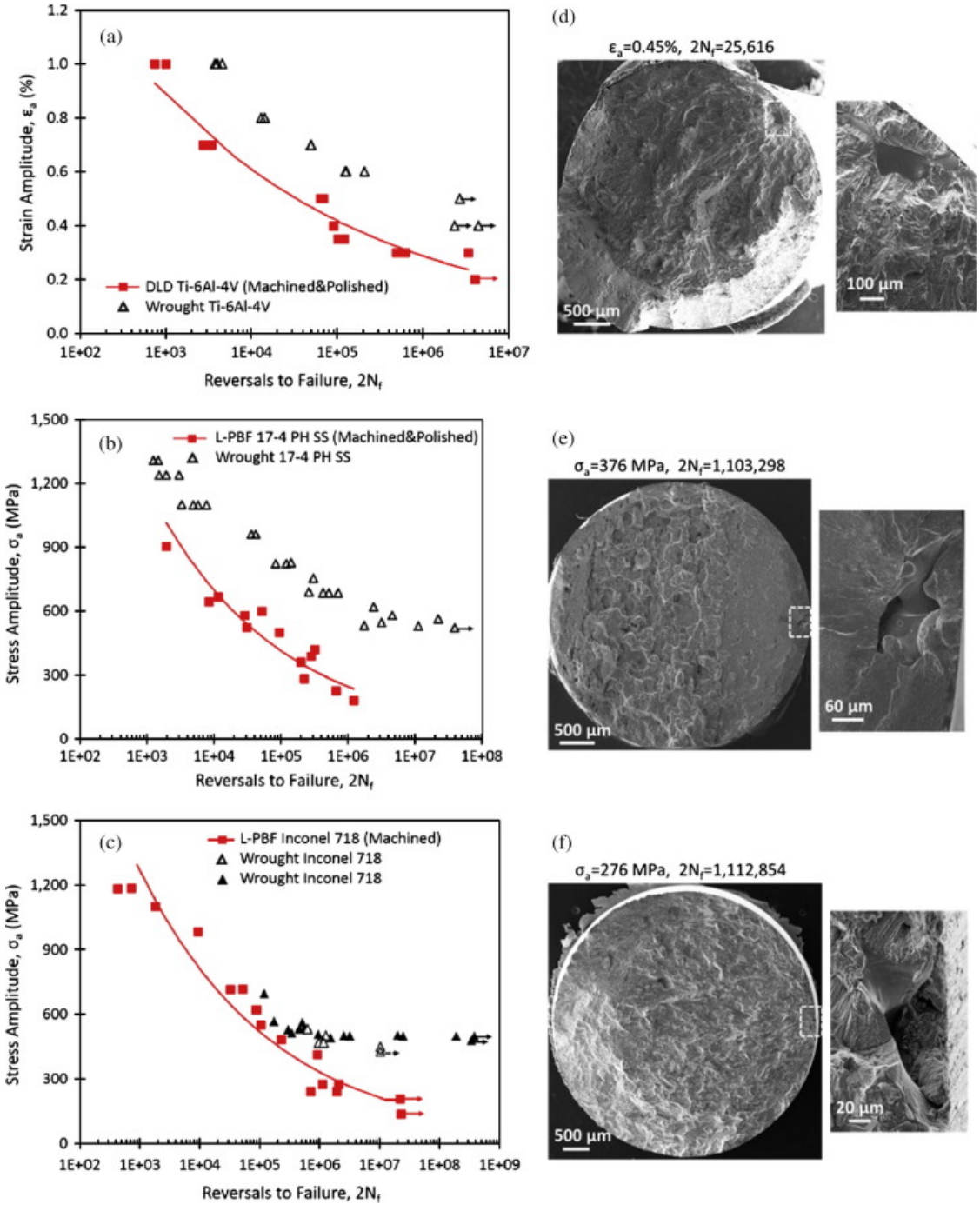

Figure 1: Fatigue data and corresponding fracture surfaces for (a), (d) DLD Ti-6Al-4V, (b), (e) L-PBF 17-4 PH SS, and (c), (f) L-PBF IN718.

Chapter 2: Cyclic Strain Rate Effect on Martensitic Transformation and Fatigue Behavior of an Austenitic Stainless Steel

The following chapter has passed rigorous peer-review process and has been published in Fatigue and Fracture of Engineering Materials and Structures in 2017.

Cyclic strain rate effect on martensitic transformation and fatigue behaviour of an austenitic stainless steel

Authors: JW Pegues, S Shao, N Shamsaei, JA Schneider, RD Moser

Publication date: 2017/12

Journal: Fatigue & Fracture of Engineering Materials & Structures

Volume: 40

Issue: 12

Pages: 2080-2091

Cyclic Strain Rate Effect on Martensitic Transformation and Fatigue Behavior of an Austenitic Stainless Steel

Jonathan Pegues[a],
Shuai Shao[b], Nima Shamsaei[a,*], Judy Schneider[c], and Robert D. Moser[d]

[a]Department of Mechanical Engineering, Auburn University, Auburn, AL, 36849, USA
[b]Department of Mechanical and Industrial Engineering, Louisiana State University, Baton Rouge, LA, 70803, USA
[c]Department of Mechanical and Aerospace Engineering, University of Alabama, Huntsville, AL, 35899, USA
[d]U.S. Army Engineer Research and Development Center, Vicksburg, MS, 39180, USA

[*]Corresponding author:
Tel: 334-844-4839
Email: shamsaei@auburn.edu

Abstract

In this study, the effect of strain rate on the cyclic behavior of 304L stainless steel is investigated to unveil the complex interrelationship between martensitic phase transformation, secondary hardening, cyclic deformation, and fatigue behavior of this alloy. A series of uniaxial strain controlled fatigue tests with varying cyclic strain rates were conducted at zero and non-zero mean strain conditions. Secondary hardening was found to be closely related to the volume fraction of strain-induced martensite which was affected by adiabatic heating due to increasing cyclic strain rates. Tests with lower secondary hardening rates maintained lower stress amplitudes during cyclic loading which resulted in longer fatigue lives for similar strain amplitudes. Fatigue resistance of 304L stainless steel was found to be more sensitive to changes in strain rate than the presence of mean strain. The mean strain effect was minimal due to the significant mean stress relaxation in this material.

Keywords: Fatigue; Secondary hardening; Cyclic deformation; Mean strain; Mean stress; 304L stainless steel

2.1 Introduction

The 300 series stainless steels (SS) are austenitic and stabilized at room temperature (RT) by alloying. This type of steel is an important family of structural materials and has a wide range of applications in the transportation, nuclear, construction, and food industries as they possess an excellent combination of strength, ductility, and resistance to corrosion [31-33]. Fatigue failure is claimed to be responsible for up to 90% of all the mechanical failures, and because many of the SS's applications involve cyclic loading, fatigue resistance is an especially important consideration for these alloys. Therefore, significant amount of studies have been conducted on the mechanical properties of the 304L stainless steel (304LSS) with an extensive focus on their fatigue behavior [34-44]. These studies have shown that (1) the SS undergo a diffusionless austenite to martensite phase transformation below the characteristic martensite start temperature, M_s *[45, 46]*, which can be affected by a number of factors, such as chemical composition and mechanical work [45-47]. (2) The transformation is sensitive to strain rate which leads to different degrees of adiabatic heating [37, 40]. (3) The martensitic phase in the SS is typically formed as a result of deformation and contributes to the strain hardening during monotonic loading and maybe the secondary hardening often observed during cyclic loading [34].

The microstructure of 304LSS comprises only Fe austenite, γ, at RT, which is a ductile face centered cubic (FCC) structure that can transform into martensite, α', which is body centered cubic (BCC) structure at very low temperatures. *Figure 2* shows the characteristic temperatures associated with the free energy of each phase. It is well established that when the SS is cooled at or below martensitic transformation starting temperature, M_s, in *Figure 2*, the FCC phase begins to spontaneously transform into a martensitic BCC phase. Although the free energies of γ and α' phases are identical at the phase equilibrium temperature, T_e, the spontaneous phase transformation

does not occur for temperatures above M_s. This phenomenon is commonly referred to as undercooling, whose extent is measured by $\Delta T = T_e - T$. The $\gamma \rightarrow \alpha'$ phase transformation is achieved by the nucleation and growth of critical α' nuclei, which requires the material to overcome a critical energy barrier (ΔG_s^*) associated with the creation of the γ-α' phase boundaries (process a → b → c in *Figure 2*). In general, the critical energy barrier ΔG^* is dependent on undercooling ΔT, such that $\Delta G^* \propto 1/\Delta T^2$ [48], as depicted by the hyperbola in *Figure 2*. It is apparent that when $T \rightarrow T_e^-$, $\Delta G^* \rightarrow \infty$ and phase transformation is not possible. Undercooling is therefore necessary for the critical energy barrier to be sufficiently low and surmountable by means of thermal fluctuation. For the case of martensitic transformation, the undercooling is $\Delta T_s = T_e - M_s$. As is evident from *Figure 2*, the M_s and T_e temperature are dependent on the slopes of the α' and γ lines, which, in turn, are sensitive to chemical composition. Eichelman and Hull [46] showed that M_s is highly sensitive to the carbon and nitrogen contents of SS.

With the aid of mechanical work, higher energy barrier (ΔG_d^*) is surmountable, which corresponds to a higher $\gamma \rightarrow \alpha'$ transformation temperature M_d (process a' → b' → c' *Figure 2*) [47]. The mechanical work can either be done by monotonic or cyclic loadings [34, 38, 39, 42, 44]. When $\Delta T < \Delta T_d$, the mechanical work that can be done before the failure of the material is not sufficient to provide the critical energy for the martensitic transformation; therefore, the austenitic phase is considered to be stable at this regime. M_d is also referred to as martensite transformation limiting temperature. Some investigations have revealed that the strain induced elevated martensitic start temperature, M_d, can be greater than RT for many austenitic stainless steels [45, 46]. Angel [45] proposed a relation between chemical composition and the M_{d30} temperature, where M_{d30} is the temperature at which applying 30% true strain results in 50% α' phase and can be an indication of the γ phase stability of the alloy for a given temperature. For

instance, an M_{d30} temperature at or above RT implies that the true M_d temperature is higher than RT, and therefore, the $\gamma \rightarrow \alpha'$ phase transformation would be expected given a sufficient amount of strain energy. For the particular alloy used in this study (304LSS), the M_{d30} temperature is estimated to be 20°C using Angle's criterion [45]. The proximity of M_{d30} to RT for this alloy implies that there is a strong possibility that the alloy's γ phase will be unstable during loading at RT.

The stability of the γ phase for austenitic stainless steels can also be influenced by strain rates as well [36, 41]. Lichtenfeld et al.[40] found that increasing strain rates in monotonic tensile tests resulted in reduced ultimate tensile strength (UTS) and ultimate uniform elongation (UEL) for a 304LSS alloy. This was attributed to adiabatic heating leading to a reduction in strain-induced martensitic transformation, resulting in reduced overall strain hardening. Hecker et al [37] found that by increasing the strain rate in a monotonically loaded specimen, there is an increase in shear band intersections, which are known to be α' nucleation sites. While increases in shear band intersections caused an increase in $\gamma \rightarrow \alpha'$ transformation for strains up to 25%, the increase in adiabatic heating ultimately suppressed the formation of martensite for strains greater than 25%.

Frequency (i.e. cyclic strain rate) effects for steels under uniaxial fatigue loadings are generally thought to be negligible for metals [49]. The frequencies commonly used in strain controlled fatigue tests are typically lower than 20 Hz, in which the increase in temperature is often insignificant, and therefore, ignored in most cases. It is generally accepted that any adverse or beneficial frequency effects are indistinguishable from the scatter that is typical in fatigue data. However, for 304LSS with an M_d temperature above the range of operational temperature, test frequency may affect the stability of the austenitic structure leading to inconsistent martensitic transformation. Olson and Cohen [50] showed that the $\gamma \rightarrow \alpha'$ transformation is highly sensitive

to temperature within the range of 0° - 50°C. The sensitivity to temperature was shown again by Hecker et al. [37] where they conducted uniaxial and biaxial tension tests at both low and high strain rates. They also showed that an increase in the strain rate could result in suppressed $\gamma \rightarrow \alpha'$ transformation due to the increased temperatures from adiabatic heating. Continuous martensitic transformation resulted in uniform elongation and an increase in strain hardening of 304LSS. In addition, tests in which martensitic transformation saturated in the early stages of elongation resulted in premature failure from early onset non-uniform elongation.

These observations on the monotonic behavior raise the question about the effect of strain rate on the cyclic behavior of 304LSS. Due to the intrinsic nature of cyclic loading, adiabatic heating from the increased cyclic strain rates may play an important role in the cyclic deformation and fatigue behavior of 304LSS. The martensite phase, α', corresponds to a higher yield strength and strain hardening rate which leads to an increased overall hardening of the material [48, 51] thus, suppression of the α' phase should result in a lower cyclic stress response. While there have been extensive studies conducted on how martensitic transformation affects the monotonic behavior for austenitic materials, there is a need to better understand how the cyclic and fatigue behavior is related to transformation phenomenon in these alloys. The transformation behavior of 304LSS is important in understanding the secondary hardening often observed during the cyclic loading of this alloy.

It is worth noting that secondary hardening has been observed in some cases during cyclic loading of 304LSS, while being absent in some other cases [35, 36, 51]. Colin et al. [36] observed secondary hardening, after a period of cyclic softening, for small strain amplitudes, and interestingly, an improvement in the fatigue life in the presence of secondary hardening. However, they only observed secondary hardening in high cycle fatigue tests. This could be related to

variations in chemical composition which affect M_d and ultimately the phase transformation behavior. In addition, variations in testing frequency could have a significant impact on the secondary hardening behavior in which increasing the frequency (i.e. cyclic strain rates) allows a greater amount of adiabatic heating within the specimen and limiting the amount of phase transformation that could occur by increasing the specimen temperature closer to M_d. However, systematic studies towards the correlation between martensitic transformations with secondary cyclic hardening are yet to be performed.

The purpose of this research is to investigate the relationship between martensitic transformation and secondary hardening through x-ray diffraction (XRD), scanning electron microscopy (SEM), and electron backscatter diffraction (EBSD). Due to the sensitivity of the material to temperatures within the $M_s - M_d$ range, the effect of strain rate and the resulting adiabatic heating were also of particular interest. Frequencies (and therefore cyclic strain rates) were varied in order to investigate the effects of adiabatic heating on the cyclic secondary hardening as well as the fatigue life for this material.

2.2 Material and Experimental Methods

2.2.1 Material

The material used for this study was a commercially available, cold drawn and annealed type 304L stainless steel delivered in lengths of six feet with a diameter of ¾ inches. This particular stainless steel is a low carbon alloy (< 0.03%) as shown by chemical composition in Table 1. The as-received 304LSS microstructure was characterized using several microscopy methods to determine grain size and initial phase fractions. The initial microstructure was fully austenitic with an average of 54 μm equiaxed grains. Present in the microstructure were annealing twins from post

process annealing to remove the cold working effects in the material. Fatigue specimens were machined longitudinally into cylindrical round specimens with uniform gage section per ASTM standard E606 [52], as shown in *Figure 3*. The specimens were then mechanically polished in the longitudinal direction using a series of 500, 800, 1200, 2000 grit silicon carbide grinding papers in order to eliminate scratches and surface discontinuities and minimize their effects on fatigue behavior.

2.2.2 Experimental Set-up

A series of uniaxial strain controlled fatigue tests were conducted on a closed loop servo-hydraulic MTS 810 fatigue testing frame with a load capacity of 100 kN. Strain was measured and controlled using an MTS extensometer and MPT testing software. Both zero and nonzero mean strain conditions including strain ratios of $R_\varepsilon = -1$ (fully reversed), $R_\varepsilon = 0$ (tension-release), and $R_\varepsilon = 0.5$ (tension-tension) were selected to determine any mean strain effects on cyclic deformation and fatigue behavior of 304LSS. Strain amplitudes between 0.2% and 1.0% were selected to include high and low cycle fatigue tests for the material with a series of two to five tests conducted for each strain level. Multiple frequencies were also chosen for each strain amplitude in order to generate a range of strain rates from 0.008 s^{-1} to 0.040 s^{-1}. Surface temperature was recorded for selected tests using an Optris Laser Sight thermometer. Temperature measurements taken from the surface provide an estimation of adiabatic heating occurring for each test. An approximate load drop of 40% as compared to mid-cycle load was considered as the failure criterion in this study.

2.2.3 Metallographic Specimen Preparation

Gage sections were removed from fatigued specimens approximately 5 mm from the fracture surface for a qualitative view of the phase transformation throughout the specimen without the effect of the plastic wake associated with crack propagation. After the specimens were cut using a low speed diamond saw, they were mounted and metallographically prepared using standard metallographic procedures. The specimens were etched for optical microscopy (OM) using a tint etchant with a 1:2 ratio of HCl and H_2O with 1g of sodium metabisulfite for 10 seconds. An optical microscope was then used to capture the images which were digitally analyzed using ImageJ software to characterize the grain size and area fraction of the α' phase. After OM imaging, a final polish was made using vibratory polishing to 0.2 μm with a silica lubricant prior to imaging with a scanning electron microsope (SEM).

2.2.4 XRD/EBSD Calibration

With trace amounts of *α'* phase expected in lower strain amplitude tests (i.e. high cycle fatigue regime), many of the peaks associated with BCC reflection planes would be indistinguishable from the background noise using XRD. It was, therefore, imperative to insure the phase analysis through EBSD was consistent with XRD for strain amplitudes in which a sufficient amount of intensity peaks were obtained. While imaging in the SEM at 20 kV excitation voltage, EBSD analysis was used to map the phases in the specimen. EBSD imaging was conducted on 450 μm by 450 μm area with step size of 1.5 μm, as shown in *Figure 4*. Multiple scans were made across the specimen to ensure 400 - 500 randomly selected grains were analyzed. In addition to the SEM/EBSD phase analysis, bulk XRD analysis was also conducted on the polished specimens using a Rigaku Ultima III with Cu kα x-rays with a 2θ range of 40° - 100° and

a scan rate of $0.02°\cdot s^{-1}$. Correlation between results obtained from XRD and SEM/EBSD analyses was used to verify the phase fraction calculations using SEM/EBSD. Three specimens were chosen for XRD and consisted of an as-received condition, a 40% monotonically strained (MT40), and a 1% fully reversed strain amplitude ($FR\varepsilon_a1.0$) test. A minimum of 3 diffraction peaks were obtained in each of the two strained specimens for the phase fraction analysis, as shown in *Figure 4*, where the intensities for each condition are normalized to the maximum intensity in the as-received condition.

Comparing XRD results of 304LSS in as-received, $FR\varepsilon_a1.0$, and MT40 conditions, there is an obvious reduction in the γ phase, as indicated by changes in peak heights, with increases in the *α'* phase due to monotonic or cyclic deformation. This is indicated by intensity rises and falls for the respective FCC and BCC reflection planes, as seen in *Figure 4*. The areas under the XRD peaks were then calculated and separated to determine the phase fractions for each specimen. These fractions were then compared with the EBSD results to determine if the two methods were in agreement. *Table 2* lists the lattice parameters, *a*, distance between planes known as d-spacings, *d*, and XRD phase fraction results for $FR\varepsilon_a1.0$ to the corresponding EBSD phase fractions. The *γ* and *α'* phase estimations from XRD and EBSD were found to be very comparable with less than 8 % difference. The lattice parameters obtained from XRD and presented in *Table 2* are also consistent with known lattice parameters of 304LSS. This gave confidence in the EBSD results for the lower strain amplitudes in which XRD was not capable in separating the smaller *α'* intensity peaks.

2.3 Experimental Results

2.3.1 Cyclic Behavior

The stress response of 304LSS alloy under the strain controlled condition is separated into two distinct stages: cyclic softening followed by cyclic secondary hardening. Cyclic secondary hardening, H_s, is defined for strain controlled fatigue tests as the difference in maximum stress amplitude near failure and the minimum stress amplitude at the end of cyclic softening, as indicated in *Figure 5*(a). These stages can be clearly seen in the stress responses for multiple strain amplitudes of fully reversed strain controlled fatigue tests at strain rates lower than 0.024 s^{-1} in *Figure 5*(b). Both of these stages are the result of microstructural changes within the material during cyclic loading. *Table 3* lists the secondary hardening, H_s, values for all fatigue tests along with the associated strain amplitude, $\Delta\varepsilon/2$, strain rate, $\dot{\varepsilon}$, stress amplitude, $\Delta\sigma/2$, , and reversals to failure, $2N_f$ for each test. A quantity to measure the rate at which secondary hardening occurs over increasing number of reversals, i.e. $\frac{d(\Delta\sigma/2)}{d(2N)}$, is defined as the secondary hardening rate.

Cyclic softening occurs as the dislocation structure rearranges until it reaches a more stable configuration, while secondary hardening has been attributed to the interaction of multiple slip systems and formation of dislocation cell structures with martensite formation being suggested as a possible contributor as well [35]. For the case of 304LSS, there have been studies that report the transformation process is γ(FCC) → ε(HCP) → α'(BCC)[8,21], while others indicate a γ(FCC) → α'(BCC) transformation could occur without the intermediate ε transformation [35, 53]. For this investigation, it must be noted that only the final area fractions of phase compositions were analyzed, and no conclusions could be made about the transformation behavior prior to failure. However, there was no evidence of ε phase using XRD or EBSD, which may be attributed to the

resolution of XRD and EBSD systems utilized. Transmission electron microscopy analysis could identify the ε phase, however, this analysis was beyond the scope of the present work.

Increase in specimen temperature during cyclic loading had a direct correlation with increase in strain rate, which is consistent with reported results for 304LSS in the literature [54]. Surface temperature stabilized within a couple hundred cycles and maintained a steady temperature until failure. For strain rates of 0.008 s^{-1}, there was an observed increase of 3 to 4 °C above RT (24 °C), while for strain rates of 0.040 s^{-1}, there was an increase of 8 to 10 °C. Although this increase in temperature may seem insignificant, *Figure 2* shows that even small changes in temperature within the M_s - M_d region can affect the transformation behavior of the material.

2.3.2 Fatigue Behavior

The strain life fatigue data of 304LSS including zero and non-zero mean strain tests are presented in *Table 3* and *Figure 6*, where $\Delta\varepsilon/2$ represents strain amplitude, R_ε is strain ratio, defined as minimum to maximum strain, $\Delta\sigma/2$ is stress amplitude taken at the mid-life cycle, and H_s is total secondary hardening. Tests that exceeded 10^6 cycles were considered to be runout and terminated. Stress amplitudes reported were taken at the mid-life cycle which was stabilized for the lower strain amplitudes ($\Delta\varepsilon/2$ <0.75%). For the higher strain amplitudes ($\Delta\varepsilon/2 \geq 0.75\%$), the stress amplitude did not reach a stable condition and immediately entered a secondary hardening stage after an initial period of cyclic softening. For these strain amplitudes (i.e. $\Delta\varepsilon/2 \geq 0.75\%$), the stress amplitudes were taken at mid-life as well, although this does not indicate stabilized stress response. Fatigue lives for mean strain data contained more scatter, however, mean strain had negligible impact on the fatigue behavior of this material. This is due to the extreme ductility of the material

in which the mean stress fully relaxes under mean strain conditions due to severe plastic deformation [36].

There is typically greater scatter in high cycle fatigue data and less scatter in low cycle fatigue data [49]. However, as evident in *Figure 6*, there is a large amount of scatter even in the low cycle fatigue regime as indicated by the circled data points. Higher frequencies were found to cause an increase in the fatigue life especially for the circled outliers in the fatigue data in *Figure 6*. Specifically for the fully reversed strain amplitude of 0.75%, the test with the shortest life of 1,514 reversals had a test frequency of 0.8 Hz, while the test frequency of 1.33 Hz resulted in a much greater fatigue life of 5,056 reversals. Furthermore, while there is significant mean stress relaxation resulting in mean strain fatigue tests exhibiting similar stress response and fatigue life as fully reversed tests, there is more scatter in the mean strain fatigue data ($R_\varepsilon = 0$ and $R_\varepsilon = 0.5$), as compared to the fully reversed data ($R_\varepsilon = -1$) for a given strain amplitude. This could be a result of the variation in the initial tensile mean stress and the number of cycles before full mean stress relaxation in mean strain fatigue tests as well as the fact that 304LSS is very sensitive to the load history [54]. In addition, there was no change in the endurance limit of $\Delta\varepsilon/2 = 0.2\%$ for mean strain conditions or increased frequencies.

Fracture surfaces were analyzed to determine if inclusions at or near the surface were the cause of crack initiation. *Figure 7* shows a representation of a typical fracture surface with fatigue crack growth direction indicated by the arrow. Fatigue cracks grew until an approximate 40% reduction in semi-stabilized load occurred after which the specimens were mechanically pulled apart. There is a clear separation between crack growth and the area that was pulled apart after a sufficient load drop. The crack growth area was found to be smooth, flat, and semi-elliptical while the pulled apart area surface contained dimples characteristics, common to fracture of ductile

metals. Fatigue cracks initiated at the surface for all fatigue specimens, with and without mean strain, with no indication of inclusions or voids contributing to the crack initiation process.

2.4 Discussion on Experimental Observations

2.4.1 Martensite Formation and Secondary Hardening

Strain-induced martensitic transformation was found to occur at strain amplitudes as low as 0.25%. This is due to the extreme ductility of 304LSS in which plastic deformation occurred even at small strain amplitudes [55]. For the case of the FRε_a1.0 sample in *Figure 4*, the γ(200) intensity peak decreased significantly as the α'(110) and α'(220) orientations increased in intensity. EBSD analysis was successful in separating the two phases, and multiple scans were taken across each specimen ensuring more than 500 grains were analyzed in order to obtain a representative estimation of the area fraction of α' phase. A typical phase fraction area for a fully reversed $\Delta\varepsilon/2$ = 0.75% test is shown in *Figure 4* with the red areas indicating the α' phase and the green areas representing the γ phase. The α' phase in the absence of the ε phase has been reported to have a blocky irregular shape. However, when it is formed in the presence of the ε phase, it becomes more lath like [38]. As shown in *Figure 4*, only blocky type martensite was found in all EBSD phase maps, indicating the ε phase was non-existent in this study. The α' phase has been shown to be associated with shear bands intersecting twin boundaries, grain boundaries, slip bands, or other shear bands in monotonic tests [39, 44]. While nucleation of the α' phase was not captured in this study, *Figure 4* indicates that nearly all α' areas are associated with either a twin boundary or grain boundary under cyclic loading.

As mentioned previously, the α' phase is formed as a result of a diffusionless, displacive phase transformation; therefore, its chemical composition is the same as the γ phase. The α' is a

harder phase than γ phase due to the following intrinsic properties associated with the BCC lattice structure: 1) the BCC-Fe has significantly higher elastic constants than FCC-Fe, i.e. C11=242 GPa, C12 =147 GPa, C44=112 GPa for BCC-Fe and C11=154 GPa, C12 =122 GPa, C44=77 GPa for FCC-Fe [56]; 2) BCC lattice has a higher Peierls barrier than the FCC lattice [57], because none of its slip systems are close-packed; 3) BCC crystals have many more slip systems than FCC crystals (48 versus 12), which leads to more frequent interactions between dislocations, and thus, much more strain hardening even at the early stage of plastic deformation. It is, therefore, expected that the nucleation and growth of α' phase would lead to hardening of the material. Indeed, in the previous studies [35, 39, 41, 42], the formation of α' phase has been directly linked to the strain hardening of 304LSS under monotonic loading conditions. However, under cyclic loading, the role of the martensite in secondary hardening still remained unclear [36].

In order to better understand the relationship between martensite formation and secondary hardening, EBSD phase maps were analyzed for selected tests. Martensite was shown to have occurred in all cyclically loaded specimens that exhibited secondary hardening. *Figure 9* shows the correlation of secondary hardening to the volume fraction of martensite for the selected specimens after failure. With increasing $\gamma \rightarrow \alpha'$ transformation, there is an increase in the secondary hardening under cyclic loading showing a clear relationship between cyclic secondary hardening and martensite formation.

Therefore, one can conclude that the martensitic transformation occurs during the cyclic loading of 304LSS, which results in an α' phase that is intrinsically harder than the γ phase. Qualitatively, it seems that the higher volume fractions of α' phase leads to higher secondary hardening. Accordingly, the effects of strain rate on seconary hardening, martensitic transformation, and fatigue behavior can be better understood.

2.4.2 Effects of Strain Rate on Fatigue Behavior

As discussed in the introduction and Section 2.3.1, increases in strain rates lead to increased temperature due to the adiabatic heating from cyclic loading. Previous studies [37, 50] on tensile deformation have already shown the sensitivty of α' formation to temperature, which can be affected by adiabatic heating due to increasing monotoinc strain rate. To investigate this behavior under cyclic loading, the adiabatic heating, and therefore, the temperature within the specimens are adjusted by controlling loading frequencies. The M_d temperature, which is the limiting temperature to martensitic formation, is above RT for the utilized 304LSS in this study. At this temperature range, the critical energy barrier *(ΔG*)* for $\gamma \rightarrow \alpha'$ transformation is very sensitive to the change in the degree of undercooling ΔT, i.e. $\Delta G^* \propto 1/\Delta T^2$. A small increase in specimen temperature reduces ΔT, and thus, significantly reduces the rate of $\gamma \rightarrow \alpha'$ transformation per loading cycle. Therefore, the adiabatic heating due to the increase in strain rate in the fatigue test ultimately reduces the secondary hardening rate.

Figure 10 presents the stress amplitude versus number of reversals at varying high/low strain rates ($\dot{\varepsilon} = 0.012 \sim 0.040\ s^{-1}$), for different strain amplitudes ($\Delta\varepsilon/2 = 0.30\% \sim 0.75\%$), and strain ratios ($R_\varepsilon$ = -1~0.5). As shown in *Figure 10*b and 9d, the secondary hardening rate is evidently higher for tests with lower strain rates. However, in *Figure 10*a and *Figure 10*c for mean strain tests, although lowering the strain rate did not lead to a higher secondary hardening rate, it caused the material to exhibit a higher stress amplitude after the initial cyclic softening stage. This could be the result of early onset of $\gamma \rightarrow \alpha'$ transformation before the conclusion of the cyclic softening. The higher stress amplitude led to early failure of specimens before entering the secondary hardening region. It is also interesting to note that the stress amplitude at failure was similar for each strain amplitude regardless of the strain rate or mean strain condition.

Additionally, the sensitivity to changes in strain rates increases by an increase in strain amplitude/level. Accordingly, smaller changes in strain rates are required to considerably change the fatigue life, as indicated in *Figure 10*. The test with lower strain rates reach this failure stress sooner due to either higher secondary hardening rate in fully reversed tests or higher cyclic stress amplitude in mean strain tests.

Figure 11 presents the mid-cycle stress and strain amplitudes for lower and higher strain rates. Since tests with mean strains yielded similar cyclic deformation behavior as the fully reversed ones, they were included in this analysis as well. Due to the suppressed $\gamma \rightarrow \alpha'$ phase transformation owing to adiabatic heating, the cyclic strain hardening for higher strain rates ($> 0.024\ s^{-1}$) is lower than lower strain rates ($\leq 0.024\ s^{-1}$). Additionally, the fatigue behavior for strain amplitudes at 0.30% or lower showed very little sensitivity to increases in strain rates due to the low amounts of plastic deformation associated with these strain levels. Strain amplitudes greater than 0.30%, however, showed increasingly higher stress responses for strain rates of $0.024\ s^{-1}$ or less as indicated in *Figure 11*. Although there is a significant amount of scatter in the data, which is attributed to varying degrees of softening/hardening for each test, it is clearly evident that lower strain rates result in greater hardening for a given strain amplitude over 0.3%. Low strain rates had a noticeably larger cyclic stress response at mid cycle than test with higher strain rates. Cyclic stress amplitudes at mid cycle were similar for lower strain amplitude tests, however, as the strain amplitude increased, the lower strain rate tests began exhibiting higher stress responses. While these differences may be small, the increase in stress typically resulted in shorter fatigue lives for 304LSS specimens.

As seen in *Figure 10*, fatigue lives of tests at lower strain rates were found to be considerably shorter, which is also attributed to the $\gamma \rightarrow \alpha'$ phase transformation. Baudry and

Pineau [34] showed that for a given plastic strain amplitude, there is a decrease in fatigue life due to an increase in the martensitic phase transformation in a Fe-18Cr-6.5Ni-0.19C stainless steel alloy. They observed, from temperature controlled fatigue tests, that crack initiation and propagation are accelerated by the $\gamma \rightarrow \alpha'$ transformation. The effect of strain rate on the fatigue life of 304LSS is further demonstrated in *Figure 12*, which presents the plastic strain-life and strain-life plots for low and high stain rate fatigue tests including zero and non-zero mean strains. There is an observable separation in plastic strain-life by changing the strain rate, while this beneficial effect appears to lessen in high cycle fatigue for total strain-life behavior. For instance, the plastic strain-life has approximately a factor of two difference in fatigue life for high and low strain rates at all strain amplitudes. This is most likely due to plastic deformation being the driving force of $\gamma \rightarrow \alpha'$ transformation.

For total strain-life behavior, there is also a factor of two difference in fatigue life in higher strain amplitudes; however, this decreases in the lower strain amplitudes. At lower total strain amplitudes, the plastic to elastic strain ratio is very small such that the effect of plastic strain on fatigue life diminishes, so it won't be as noticeable (see *Figure 12*(b)). Additionally, there was no significant change in fatigue behavior by increasing the strain rate up to 0.024 s^{-1} in either plastic or total strain amplitudes as there was no appreciable change in temperature for these strain rates. However, for strain rates greater than 0.024 s^{-1}, some enhancement in the fatigue resistance of 304LSS was observed. For this particular 304LSS alloy, it appears that an increase in temperature for $\Delta T \approx 6℃$ within the $M_S - M_d$ range is sufficient to improve the fatigue behavior. It is import again to note that chemical composition is an important factor in stability of the γ phase, and thus, the sensitivity to adiabatic heating will vary from alloy to alloy.

In summary, increases in cyclic strain rates result in higher adiabatic heating for a given strain amplitude which leads to a lower rate of $\gamma \rightarrow \alpha'$ phase transformation. The reduction in $\gamma \rightarrow \alpha'$ phase transformation results in a lower secondary hardening rate as well as longer fatigue life. Therefore, the fatigue behavior of 304LSS is sensitive to strain rates due to the martensitic phase transformation, which is in turn dependent on the stability of the austenitic phase in this alloy. This finding has important implications for the use of 304LSS where the operating temperature falls within the $M_s - M_d$ temperature range. These characteristic temperatures are highly dependent on the chemical composition of this austenitic stainless steel.

2.5 Conclusions

Microstructure has long been understood to play a pivitol role in the cyclic behavior of engineering materials such as 304L stainless steel. For this reason, it is of great interest to link the macroscopic behavior of materials to their microstructural characteristics. Through this study, it has been shown that:

1) Mean strain had little effect on fatigue life, secondary hardening, or martensite formation. This is due to the ductility of 304L stainless steel fully relaxed mean stress for mean strain conditions. The mean strain fatigue specimens also had very similar α' volume fractions after failure as the fully reversed specimens with the same strain amplitude.
2) The austenite to martensite transformation in 304L stainless steel can even occur at very low strain amplitudes. The α' phase was observed in fatigue specimens with strain amplitudes as low as 0.25%.
3) The area fraction of α' can be correlated to the amount of total secondary hardening, H_s, defined as the increase in stress amplitude from the end of the cyclic softening stage to the maximum stress before failure.

4) Increases in the strain rate and the corresponding elevated temperature can reduce the rate of which secondary hardening, H_s, occurs. Tests at lower strain rates experienced less adiabitic heating and exhibited greater strain hardening behavior than tests at higher strain rates. This is due to the sensitivity of martensite formation to the adiabatic heating under cyclic loading in the M_s - M_d temperature range.
5) Increasing strain rates improved fatigue lives of the 304L stainless steel, specifically in the low cycle fatigue regime. The stress at failure was essentially the same for similar strain amplitudes, and thus, the increase in temperature at higher strain rates resulted in lower rates of secondary hardening, and higher number of reversals needed to reach failure.

Finally, the main finding from this study is the observation that the fatigue resistance of 304L stainless steel is more sensitive to changes in strain rate than the presence of mean strain.

Acknowledgments

Effort sponsored by the Engineer Research & Development Center under Cooperative Agreement number W912HZ-15-2-0004. The views and conclusions contained herein are those of the authors and should not be interpreted as necessarily representing the official policies or endorsements, either expressed or implied, of the Engineer Research & Development Center or the U.S. Government. This work was done while Jonathan Pegues, Shuai Shao, and Nima Shamsaei were at Mississippi State University.

Table 1: *Chemical composition of austenitic stainless steel in % weight (remainder Fe).*

% C	% Co	% Cr	% Cu	% Mn	% Mo	% N	% Ni	% P	% S	% Si
0.029	0.150	18.063	0.450	1.347	0.384	0.072	8.588	0.032	0.030	0.283

Table 2: Lattice parameter, a, and d-spacings, d, for a given angle, 2θ obtained from XRD as well as area phase fractions from both XRD and EBSD for the 1.0% fully reversed strain amplitude FRεa1.0.

(hkl)	Phase	2θ (°)	a (nm)	d (nm)	γ(FCC) fraction (%)	α'(BCC) fraction (%)
111	γ	43.5	0.360	0.207	**XRD Results**	
110	α'	44.5	0.288	0.203	83.7	16.3
200	γ	50.7	0.360	0.180		
200	α'	64.7	0.287	0.144	**EBSD Results**	
220	γ	74.7	0.360	0.127	84.9	15.1
211	α'	82.2	0.287	0.117		
311	γ	90.7	0.360	0.108		

Table 3: Experimental results for strain-controlled fatigue tests of 304LSS with and without mean strains.

$\Delta\varepsilon/2$ (%)	$\dot{\varepsilon}$ (s^{-1})	$\Delta\sigma/2$ (MPa)	H_s (MPa)	Reversals to Failure ($2N_f$)
R_ε = -1 (Fully Reversed)				
0.2	0.04	285	NA	>2,594,000
0.2	0.008	284	NA	>2,000,000
0.2	0.016	326	NA	>2,000,000
0.25	0.030	296	16	446,772
0.25	0.030	291	8	241,452
0.3	0.012	314	14	130,728
0.3	0.024	317	18	120,824
0.3	0.010	303	8	82,676
0.4	0.040	320	14	35,244
0.4	0.016	329	16	21,266
0.4	0.016	327	11	15,694
0.5	0.016	359	20	9,066
0.5	0.016	351	22	7,980
0.5	0.020	354	65	6,076
0.5	0.020	342	7	4,506
0.75	0.040	373	22	5,056
0.75	0.024	371	15	1,514
1	0.032	436	26	838
1	0.020	452	80	600
R_ε = 0 (Tension-Released)				
0.2	0.024	331	NA	>2,600,000
0.3	0.024	324	26	219,826
0.3	0.024	310	11	100,126
0.4	0.040	329	56	49,338
0.4	0.016	340	10	17,502
0.4	0.016	333	69	13,836
R_ε = 0.5 (Tension-Tension)				
0.2	0.016	366	NA	>2,139,038
0.3	0.040	306	9	116,032
0.3	0.012	319	3	49,074
0.3	0.012	322	3	29,736
0.4	0.008	361	32	39,656
0.4	0.008	342	44	34,208
0.4	0.040	322	36	32,984
0.4	0.040	319	10	27,348
0.4	0.016	381	13	17,553

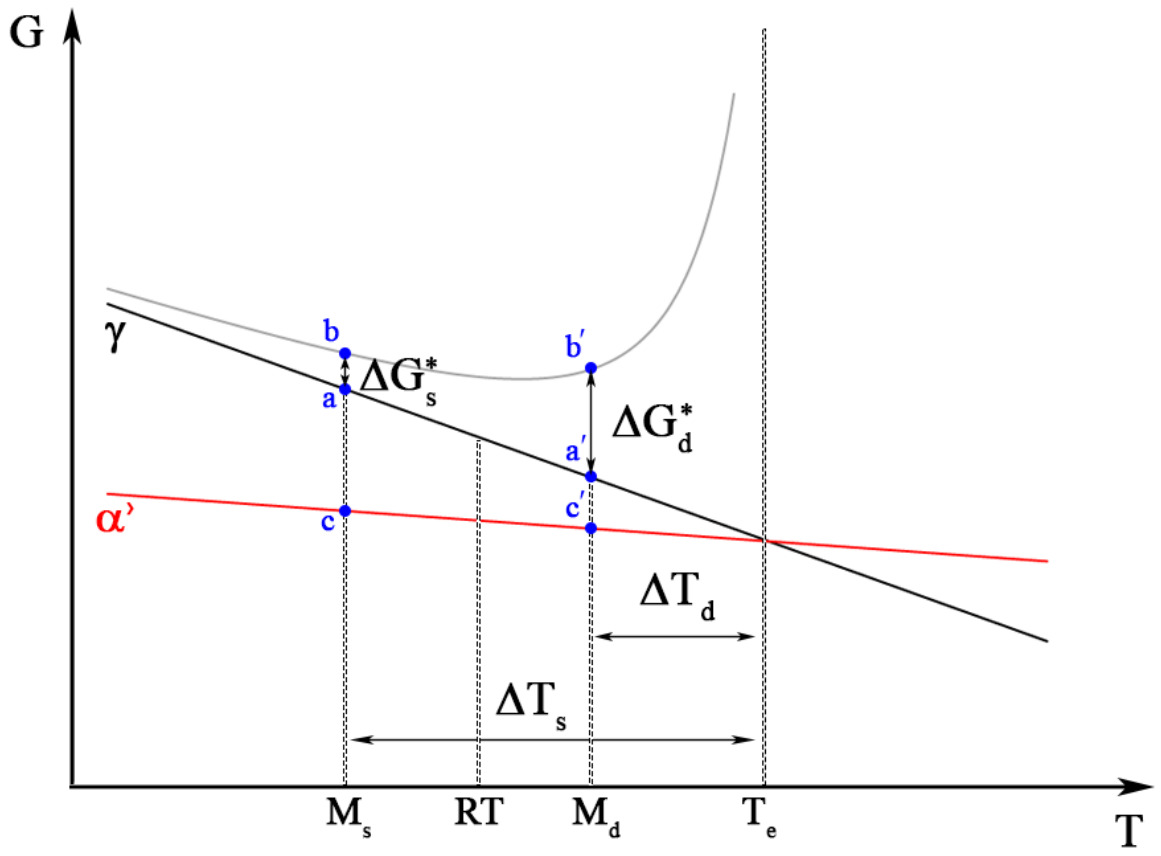

Figure 2: Gibbs free energy diagram depicting the characteristic martensite temperatures Ms, and Md. The hyperbolic curve represents the critical free energy as a function of temperature (i.e.,G_γ (T)+ΔG^* (T)) of a γ matrix containing a given number of critical

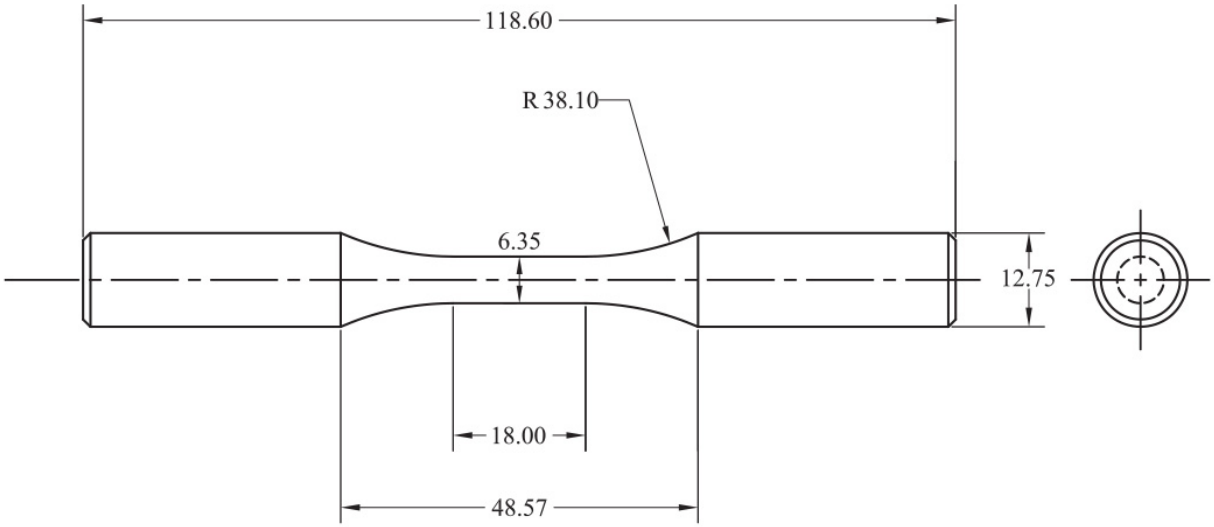

Figure 3: Dimensions and configuration of uniaxial fatigue specimens, designed per ASTM standard E606. All dimensions in mm.

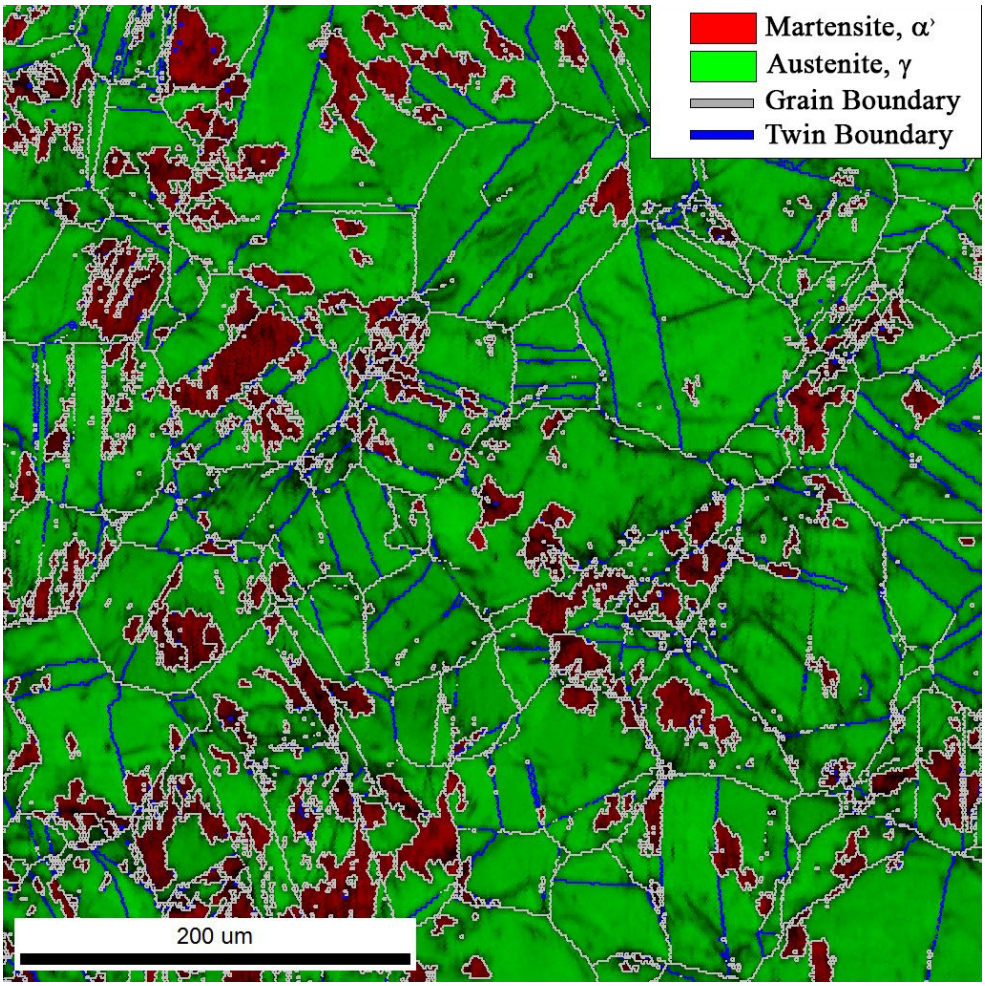

Figure 4: EBSD image quality phase map for Rε = 0.5 and Δε/2 = 0.3% with a strain rate of 0.040 s-1.

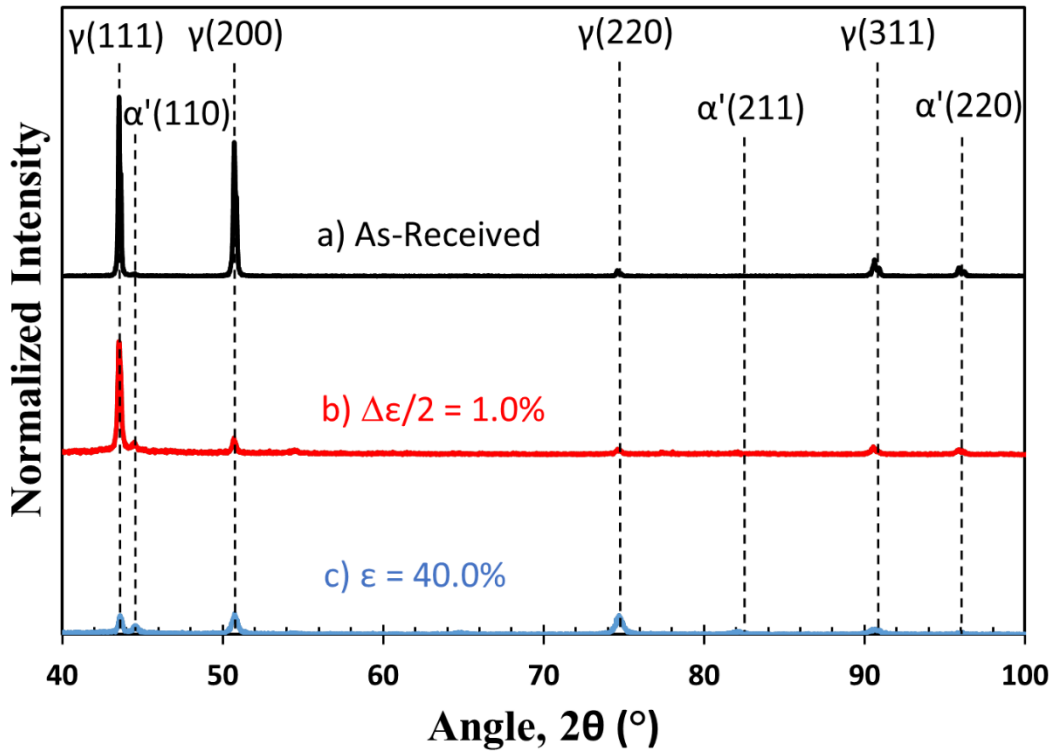

Figure 5: X-Ray diffraction phase analysis for a) as-received, b) FRε_a1.0, and, c) MT40 specimens showing the progression of γ austenite to α' martensite for the respective reflection planes. Peaks for each condition are normalized to the maximum intensity in the as-received condition.

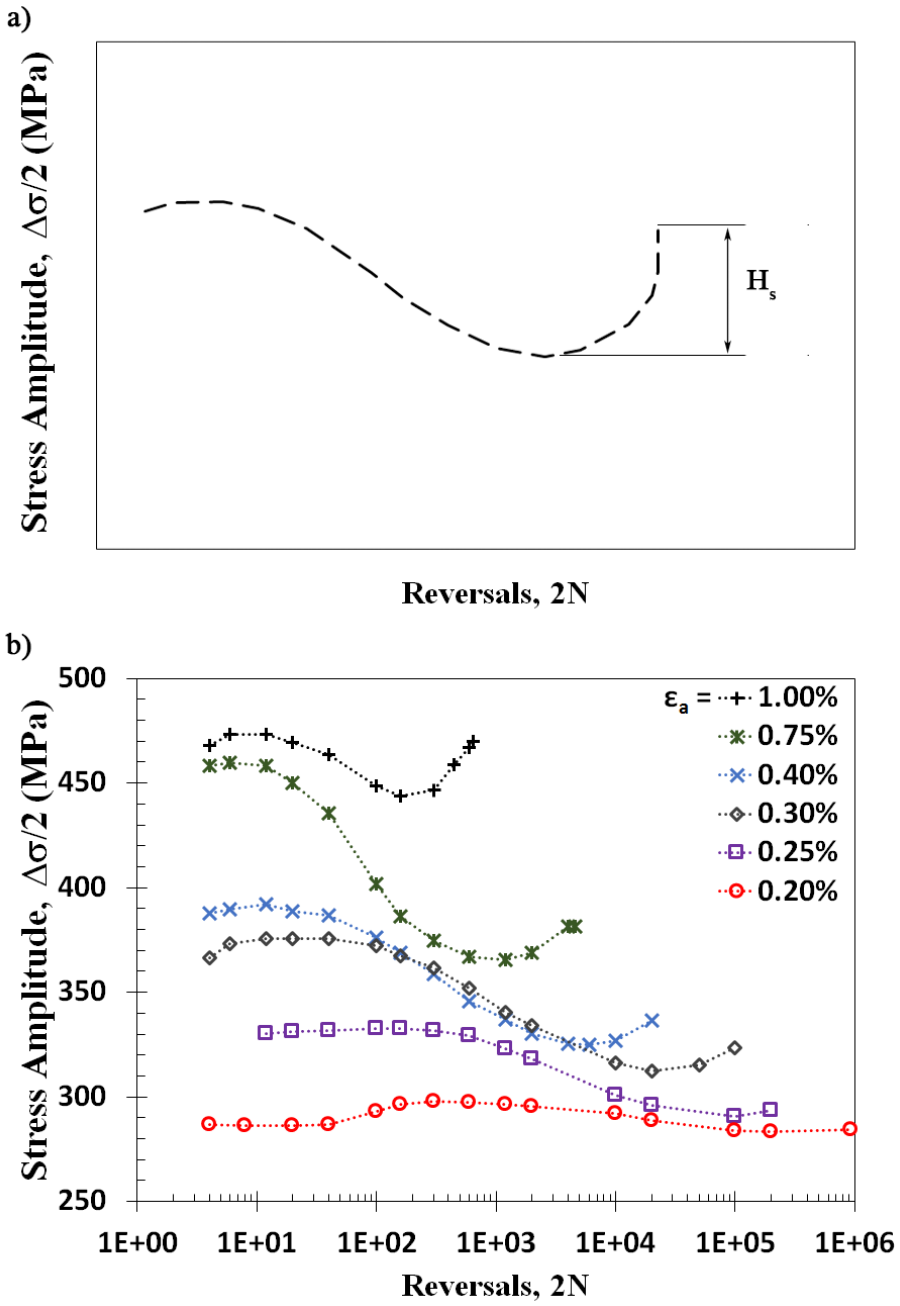

Figure 6: a) Secondary cyclic hardening, H_s, is defined as the difference between the peak stress amplitude near the end of fatigue life and the minimum stress amplitude due to cyclic softening. b) Typical stress response of uniaxial strain controlled fully reversed fatigue specimens for strain rates < 0.024 s^{-1} highlighting the distinct softening and secondary hardening that occurs in 304LSS.

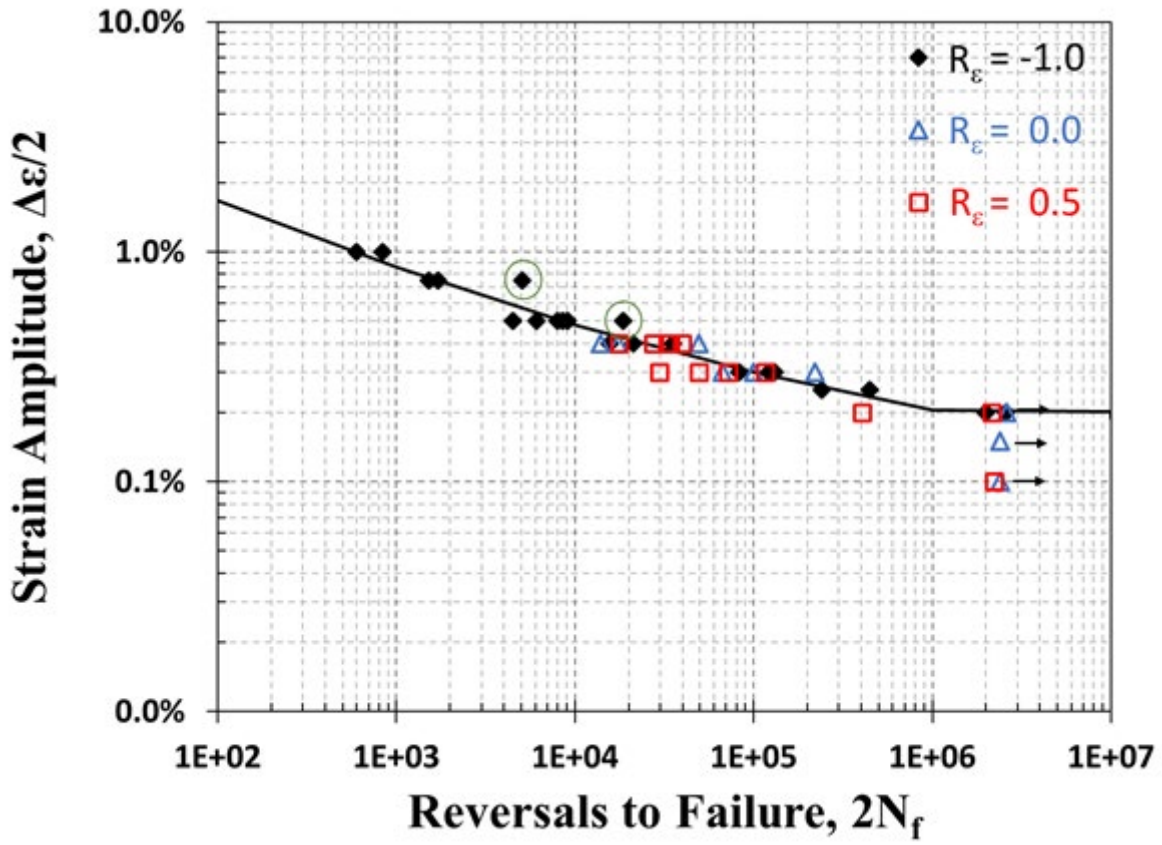

Figure 7: Strain life fatigue data for 304LSS including zero and non-zero mean strains.

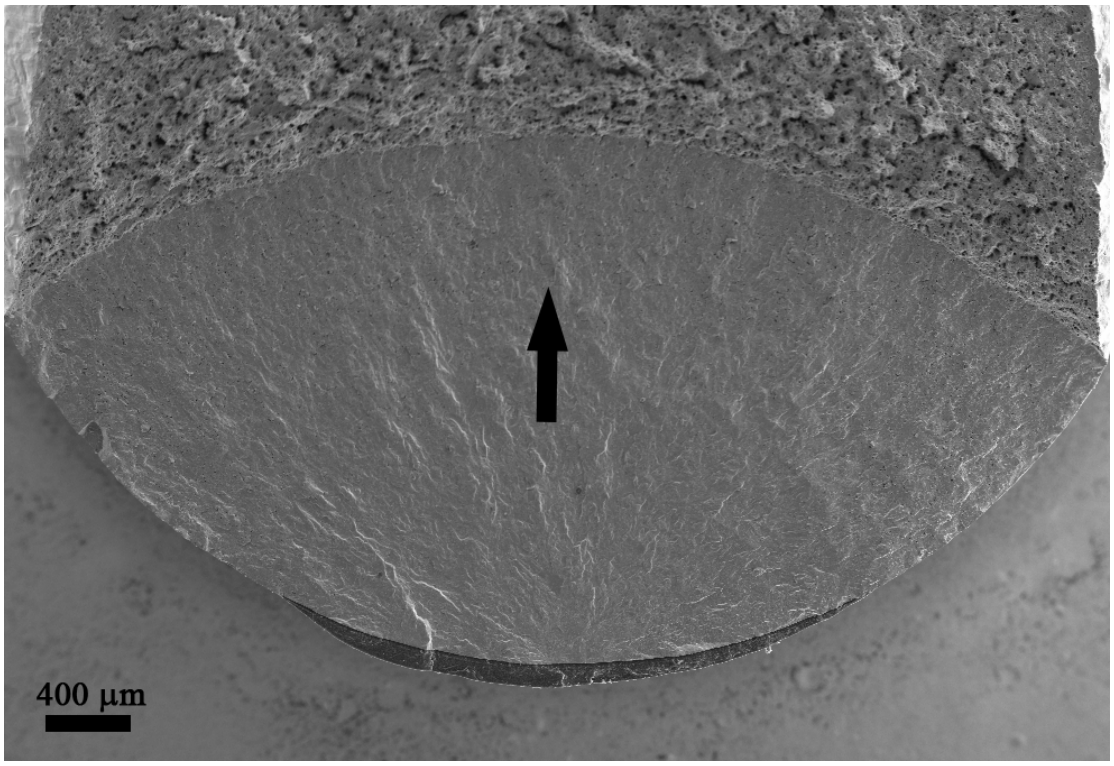

Figure 8: Fracture surface of a fatigued specimen. Arrow and box indicate the direction of crack growth and crack initiation site, respectively.

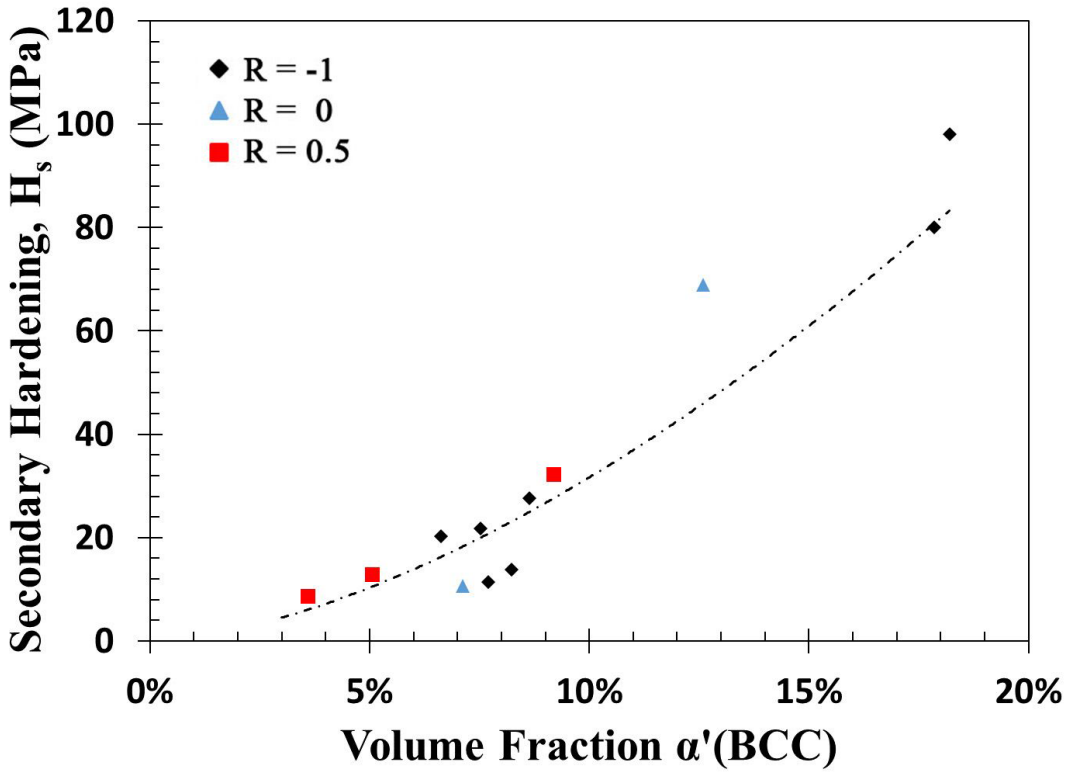

Figure 9: Cyclic secondary hardening relation to the area fraction of martensite of selected fatigue specimens after failure.

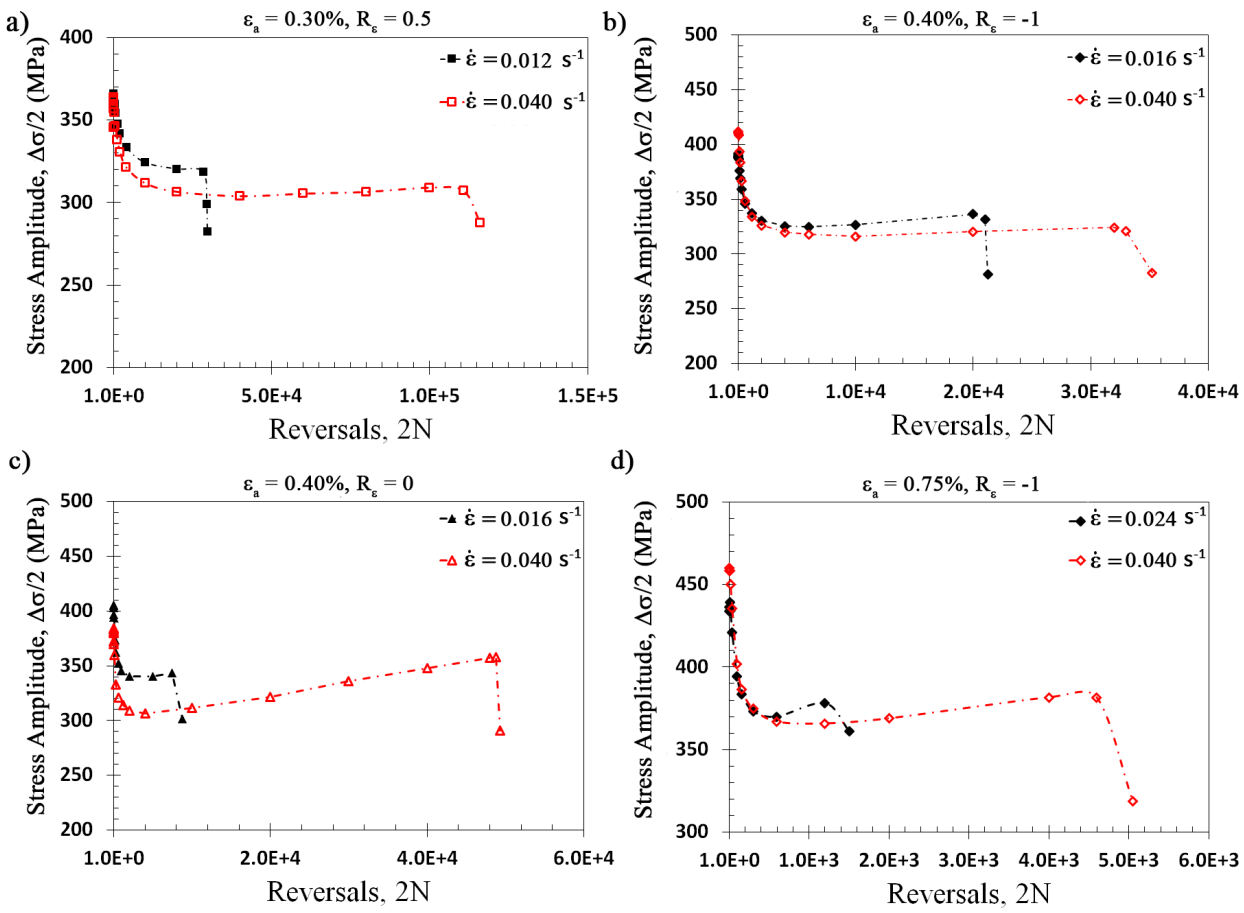

Figure 10: Stress response for uniaxial strain controlled fatigue test at a) $\Delta\varepsilon/2$ = 0.30% and R_ε = 0.5, b) $\Delta\varepsilon/2$ = 0.40% and R_ε = -1, c) $\Delta\varepsilon/2$ = 0.40% and R_ε = 0, and d) $\Delta\varepsilon/2$ = 0.75% and R_ε = -1 with varying strain rates.

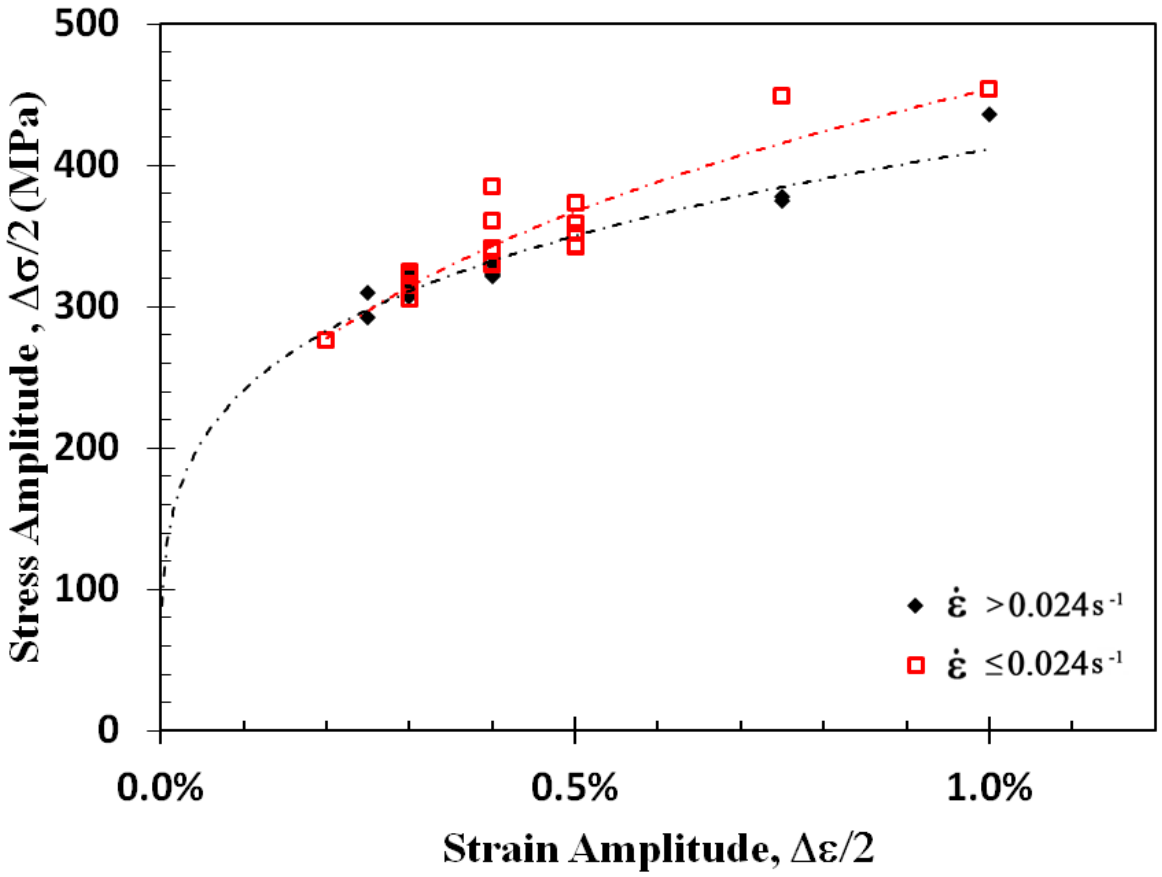

Figure 11: Cyclic stress amplitudes versus strain amplitudes for all fatigue data at high and low strain rates.

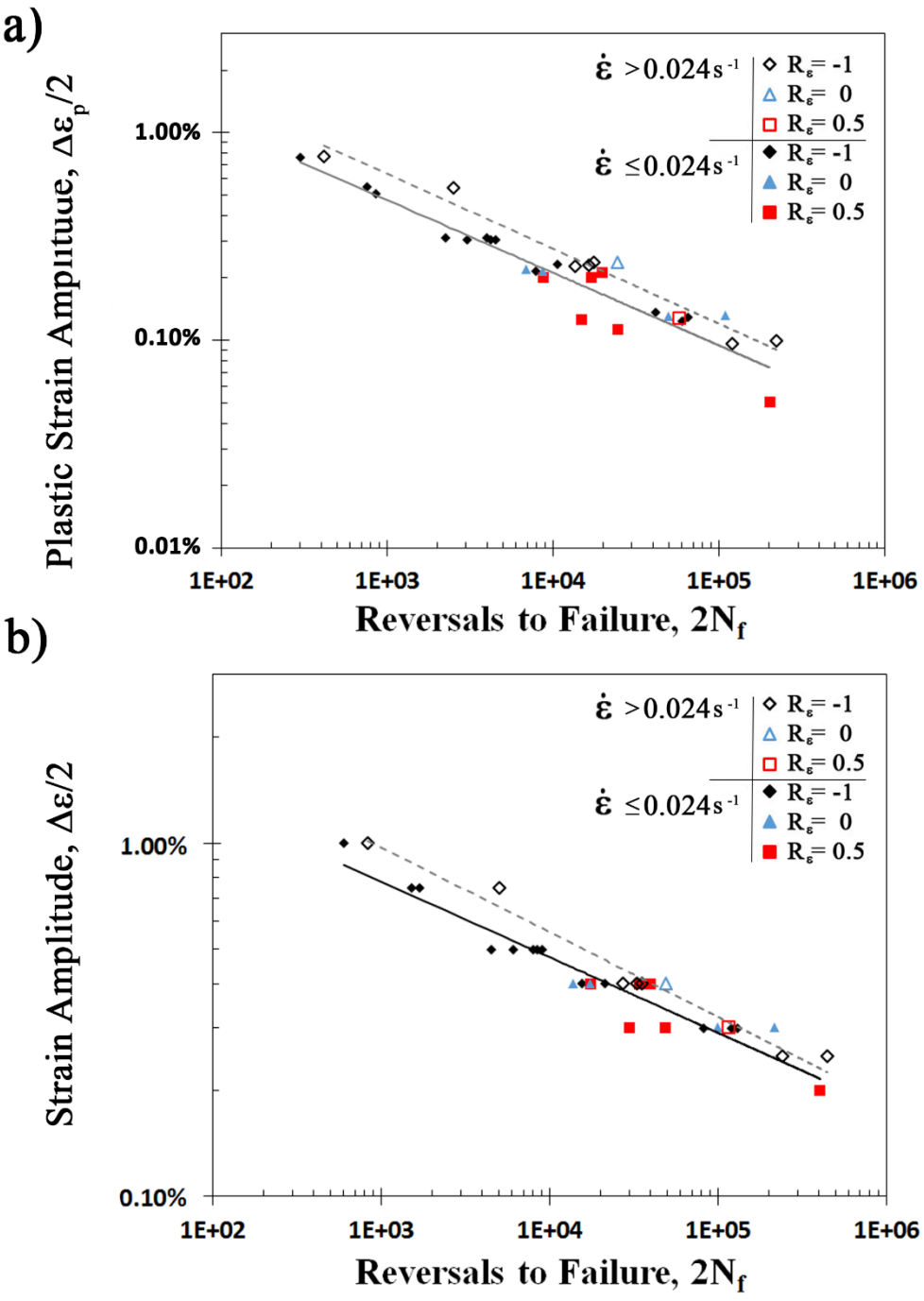

Figure 12: a) Plastic strain amplitude versus fatigue life and b) total strain amplitude versus fatigue life for tests with strain rates of $\dot{\varepsilon} \leq 0.024$ s^{-1} and $\dot{\varepsilon} > 0.024$ s^{-1}.

Chapter 3: Influence of Microstructure on Fatigue Crack Nucleation and Microstructurally Short Crack Growth of an Austenitic Stainless Steel

The following chapter has passed rigorous peer-review process and has been published in Materials Science and Engineering A in 2017.

Influence of microstructure on fatigue crack nucleation and microstructurally short crack growth of an austenitic stainless steel

Authors: Jonathan W Pegues, Michael D Roach, Nima Shamsaei

Publication date: 2017/11/7

Journal: Materials Science and Engineering: A

Volume: 707

Pages: 657-667

Publisher: Elsevier

Influence of Microstructure on Fatigue Crack Nucleation and Microstructurally Short Crack Growth of an Austenitic Stainless Steel

Jonathan W. Pegues[1], Michael D. Roach[2], Nima Shamsaei[1]

[1]Laboratory for Fatigue & Additive Manufacturing Excellence (FAME), Department of Mechanical Engineering, Auburn University, Auburn, AL 36849

[2]Department of Biomedical Materials Science, University of Mississippi Medical Center, Jackson, MS 39216

Corresponding author:

Tel: 334-844-4839

Email: shamsaei@auburn.edu

Abstract

In this study, the effect of microstructure on crack nucleation and microstructurally short fatigue crack growth is investigated for a metastable austenitic stainless steel. Fatigue tests were conducted at an intermediate fatigue life regime between 10^4 and 10^6 cycles such that martensitic phase transformation occurs given sufficient localized deformation. Through the use of scanning electron microscopy, along with electron backscatter diffraction, several micro-cracks were analyzed and compared. The influence of microstructural features such as twin boundaries, slip band intrusions/extrusions, grain boundaries, inclusions, and martensitic transformed areas on the crack initiation life is discussed. The initiation stages of crack nucleation and the subsequent microstructurally short crack growth for each microstructural feature are compared revealing that twin boundaries and slip bands are the most dominant initiation features. However, the initiation mechanism governing crack nucleation for each feature was different. Additionally, the phase

transformation behavior showed only minor effects on the microstructurally short crack growth leading up to an engineering crack. It was found that while the cracks that propagated more quickly had larger transformed martensitic zones around the crack tip, this was due mostly to the size of the crack. Interestingly, the initiation life in the transitional fatigue regime was observed to be more sensitive to crack initiation feature than the martensitic transformation.

Keywords: Crack Initiation; Microstructurally Small Crack Growth; Martensitic Transformation; Microstructure; 304L Stainless Steel; Fatigue

3.1 Introduction

Traditionally, fatigue life is separated into the initiation stage and the fatigue crack propagation stage. The crack initiation stage can be further separated into the life to nucleate a micro crack and the subsequent microstructurally short crack (MSC) growth that continues until the crack is long enough not to be directly influenced by the microstructure. The crack initiation is heavily affected by the microstructural features, and thus, there is a need to fully understand the microstructure-fatigue property relationships. It is well established that cracks initiate at a variety of microstructural features such as twin boundaries (TB), grain boundaries (GB), slip band extrusion/intrusions (SB), and inclusions (IN) in many austenitic stainless steels [13, 14, 16, 18, 19, 51]. Previous research studies have shown that crack initiation in the high cycle fatigue regime (fatigue lives of $N_f > 10^6$) is dominated by twin boundaries rather than other microstructural features [13, 14, 16, 18, 19], while crack initiation during low cycle fatigue (fatigue lives of $N_f < 10^4$) is dominated by inclusions for many austenitic stainless steels [51]. This is in contrast to most metals which typically show crack initiation at inclusions in the high cycle regime and other microstructural features such as slip bands and grain boundaries in the low cycle regime. Additionally, the majority of the high cycle fatigue life is spent initiating an engineering crack [49, 58], defined as a fatigue crack with a length on the order of a few average grain diameters. In contrast, the majority of the low cycle fatigue life is spent in the crack propagation stage where plastic deformation results in much quicker crack initiation [49]. The transitional fatigue regime between the low and high cycle regime ($10^4 < Nf < 10^6$) would then be expected to show a mixture of low and high cycle crack initiation behavior since the ratio of plastic and elastic strain is near unity.

For metastable austenitic stainless steels such as 304L (304LSS), the effect of microstructure on crack initiation can be complicated by the austenite, γ (FCC), to martensite, α' (BCC), phase transformation (γ → α' phase transformation) [10, 38, 43, 59-62]. During high cycle fatigue, the plastic strain is not typically large enough to show significant initiation of the γ → α' transformation [35]. As the load approaches the transitional fatigue regime, the increase in plastic strain may result in martensitic transformation. The effect of this phase transformation leads to cyclic hardening of the material from a combination of (1) the higher strength of the α' phase, (2) the increased dislocation density from the γ → α' phase transformation [63, 64], and (3) the subsequent interaction of these dislocations. The transformation from austenite to martensite also results in an increase in volume of approximately 2% [61], which can affect the growth behavior of MSC due to transformation induced crack closure [65]. In contrast, Pineau and Pelloux [43] showed that fatigue crack growth rates were higher in a martensitic stainless steel when compared to stable austenitic stainless steels. It remains, however, to understand how the γ → α' phase transformation during cyclic loading affects the MSC growth behavior for nucleated cracks and the life to initiate a dominant crack in the material.

The primary purposes of this investigation are to determine the effect of microstructure on fatigue crack initiation and to study the development of martensite in the vicinity of microstructurally short cracks (MSC) in a commercially available 304L stainless steel. Additionally, the effects of microstructure and the γ → α' transformation on the crack initiation stage are investigated in a transitional fatigue life regime (i.e. $\frac{\varepsilon_p}{\varepsilon_e} \approx 1$).

3.2 Material and Experimental Program

3.2.1 Material and Specimen Design

The 304LSS used in this study was delivered in cold drawn and annealed ¾" diameter bars with the chemical composition listed in *Table 4* and the reported mechanical properties listed in *Table 5*. Two specimen types were used for this study, as shown in *Figure 13*. Traditional cylindrical fatigue specimens with uniform gage section as indicated in *Figure 13*(a) were machined longitudinally from the as received bar. These specimens were carefully ground smooth using a series of 500, 800, and 1200 grit silicon carbide papers. Round cornered square gaged fatigue (SGF) specimens were also machined longitudinally from the bar as shown in *Figure 13*(b) and ground smooth with silicon carbide papers. Before testing, SGF specimens were electrolytically polished using a Struers Lesctropol 5 with a perchloric acid electrolyte (A2, Struers) at 45 V for 40 s and not allowed to exceed 32° C. The electro-polishing allowed high quality diffraction patterns to be obtained using EBSD even after substantial cyclic loading. The EBSD maps were conducted using EDAX-TSL software at an acceleration voltage of 20 kV with step sizes ranging from 0.1 – 0.5 μm using a hexagonal scan grid.

The as received microstructure consisted of equiaxed grains with a high density of annealing twins. *Figure 14* details the as-received microstructure for the cross-section of a selected SGF specimen after electro-polishing and before testing. *Figure 14*(a) is an inverse pole figure map (IPF) from electron backscatter diffraction (EBSD) showing equiaxed grains with a high density of annealing twins. *Figure 14*(b) presents the grain size distribution for the given IPF map showing an average grain size around 54 μm for the scanned area. The average grain size was verified using a grain boundary etch and lineal intercept method. *Figure 14*(c) gives a representation of the martensite phase distribution throughout the microstructure and shows a

fully austenitic microstructure. While the microstructure was shown to be fully austenitic, there were some trace amounts of δ-ferrite. These δ-ferrite were elongated in the direction of the cold drawing and were removed by the electro-polish, which resulted in elongated voids in the longitudinal direction of the SGF fatigue specimens. *Figure 14*(d) presents the fraction of twin boundaries (blue) for the selected area. Annealing twins are known to have a specific misorientation of 60° which have an allowable deviation of 8.66° from the ideal Σ = 3 boundary according to the Brandon criterion. Thus, twin boundaries were defined as the ones with 60° ± 8.66° misorientation, while grain boundaries were defined as all other boundaries above 5° misorentation.

3.2.2 Fatigue Testing

A series of interrupted and non-interrupted fully reversed uniaxial load controlled fatigue tests were conducted on a closed loop servo-hydraulic MTS 810 fatigue testing frame with a load capacity of 100 kN. Non-interrupted tests using the specimen design shown in *Figure 13*(a) were conducted at stress amplitudes of 300, 330, 350, and 400 MPa with sinusoidal wave forms in order to construct a stress-life (σ_a-$2N_f$) curve. An extensometer was used to record the cyclic strain and the generated stress-strain behavior was used to determine a stress level that was within the transitional fatigue regime. Due to a limited number of samples from the same production batch of material, only two tests were conducted for each stress amplitude except for the runout stress amplitude, for which only one test was conducted.

Previous research has shown that for a Fe-18Cr-6.5Ni-0.19C stainless steel, plastic strain amplitudes greater than 0.18% are capable of generating significant amounts of the α' phase [43] while another study reported the α' phase transformation to occur at total strain amplitudes as

low as 0.2% [10]. The cyclic stress and strain data showed that a stress amplitude of 330 MPa produced a plastic strain amplitude of 0.18% and a plastic to elastic strain ratio of approximately 0.9 at half life. This ratio was determined to be in the desired transitional region of the fatigue life.

Interrupted tests using the SGF specimens shown in *Figure 13*(b) were then performed at a stress amplitude of 330 MPa, which approximately corresponded to the transition from the low to the high cycle fatigue regime. Tests were interrupted every 10,000 cycles until multiple micro-cracks were observed on each surface using scanning electron microscopy (SEM) after which tests were interrupted every 3,000 – 5,000 cycles. MSC growth rates (da/dN) were calculated as $(2c_i - 2c_{i-1})/(N_i - N_{i-1})$ where i is the current cycle count. Due to the tortuosity of the MSC crack growth, the crack lengths (2c) were calculated by summing the straight line lengths of the surface cracks from tip to tip. During the interrupted period, the specimen was removed from the testing equipment and carefully aligned in the SEM stage as described in the following section. Interrupted testing was then continued until multiple cracks of approximately 200 μm were observed. At this length, the crack initiation stage (i.e. the combination of crack nucleation and microstructurally short crack growth stages) was assumed to be completed with only the long crack propagation stage remaining.

3.2.3 SEM/EBSD Data Collection

Scanning electron microscopy was used to detect micro-cracks between 20 – 50 μm on the surface of the SGF specimens during the interrupted fatigue testing. Once a crack was discovered, a secondary electron image was taken of the surrounding surface to record the

position of each crack on the surface. During subsequent interruption periods, each crack was located and new cracks were detected.

After imaging, the specimen was tilted so that the surface was at an angle of 70° from the electron beam in order to capture EBSD maps. Surface grain orientation and phase distribution maps were collected along with Taylor and Schmid factor maps for the γ phase by applying the loading direction and the primary FCC slip system of {111} planes in the <110> direction to the grain orientation datasets. Previous research has shown that a relatively large mismatch of Schmid factors of adjacent grains can increase the localized stress across the given boundary which can result in crack initiation along the boundary [66]. Additionally, Taylor factor mismatches (TFM) have been suggested to be an important factor for twin boundary cracking. A large TFM across a twin boundary can be indicative of a strain incompatibility resulting in twin boundary cracking [10, 16, 67]. For grain and twin boundary cracks, the Schmid factor mismatch (SFM) and Taylor factor mismatch (TFM) values between grains on either side of the boundary were of particular interest as they can be indicative of stress concentrations and elastic incompatibilities across the boundaries. Taylor factors were further classified as either low (2.24 – 2.68), medium (2.69 – 3.16), or high (3.17 – 3.64) with the subsequent mismatches being low-low (LL), low-medium (LM), low-high (LH), medium-medium (MM), medium-high (MH), or high-high (HH) as described by Roach et al [16].

Crack initiation features were classified as either twin boundary (TB), grain boundary (GB), slip band (SB), inclusion (IN), or martensite (M) cracks. Four SGF specimens were tested under the given conditions and a total of sixty-seven cracks were analyzed to obtain a variety of crack initiation feature types for data analysis.

3.3 Experimental Results

3.3.1 Cyclic Behavior

The stress-life plot presented in *Figure 15* along with the SGF specimens data indicate that crack nucleation, MSC growth, and long crack growth stages were all considerable at a stress amplitude of 330 MPa. Under the constant amplitude load control conditions, cyclic softening and cyclic hardening were observed as an increase and decrease in strain amplitude, respectively. *Figure 16* presents the cyclic stress-strain behavior associated with the stress amplitude of 330 MPa. Stage (1) represents the cyclic softening stage in which a repeated stress amplitude results in a larger strain amplitude for the proceeding cycle. This occurs as the microstructure moves into a more stable configuration by an increasing of mobile dislocations [59, 68]. Stage (2) represents the cyclic hardening stage in which the same stress results in a lower strain amplitude. At this stage, the microstructure aligns into a more stable configuration which results in the activation of multiple slip systems for a given grain and results in the interaction of the activated slip systems. Additionally, the intersection of the activated slip systems results in $\gamma \rightarrow \alpha'$ phase transformation further contributing to the cyclic hardening observed in the material [59]. Previous research has shown a strong correlation between secondary hardening and the volume fraction of the α' phase [10]. These stages are evident in *Figure 16*(a). *Figure 16*(b) presents the hysteresis loops for the first cycle as well as cycle 20,000 showing a small amount of tensile cyclic creep which may be attributed to a small amount of pre-strain left over from the drawing process [68].

The interrupted cyclic tests on SGF specimens present an opportunity to observe the changes in microstructure on the surface over the early stage of the fatigue crack initiation. Periodically, when collecting initiation and crack propagation EBSD maps, surface maps were taken over larger areas to observe any microstructural changes on the surface without the influence

of the growing crack. The rotation of the grains was readily observable during the interrupted load controlled fatigue tests as indicated by *Figure 17* showing the same area of the microstructure after a) 20,000 cycles and b) 35,000 cycles (loading direction is horizontal in respect to *Figure 17*). The superimposed inverse pole figures (IPF) in *Figure 17* shows the rotation for each grain on opposing sides of a twin boundary with increasing cycles. This rotation of the grains is attributed to cyclic creep that has been shown to often occur in pre-strained low carbon steels [68].

The α' phase in *Figure 17* appears as the much smaller and irregular shaped grains within the γ grains. Notice that grains A and C show mainly one active slip system as indicated by the single direction of the slip traces within each grain. However, as the grain axis rotates towards the loading axis, other slip systems can become active and deformation may occur on two slip systems. Chai and Laird showed cyclic creep is likely to occur during fatigue loading due to dislocation motion being favored in a particular direction when some pre-strain is present in the material [68]. For the 304LSS investigated, the rotation of the grain axes is similar to the rotation observed for grains under large monotonic tensile/compression strains [69]. In this case, grains with tensile cyclic creep rotate towards a {112} pole, while grains with compressive creep rotate to a {111} pole. These rotations occur until the grain axis reaches the boundaries in which the resolved stress is equal for two slip systems resulting in double slip. For the tensile case, this occurs between the [001] and [111] boundary on the stereographic triangle, while compression occurs between the [001] and [011] boundaries [69]. These tensile and compressive rotations are evident in IPF stereographic triangles for grains A, B, and C in *Figure 17*.

The interaction of multiple slip systems can be very important in the martensitic phase transformation behavior as these intersections often result in the nucleation of the α' phase within

a grain rather than at the grain boundary [39]. This is also evident in *Figure 17* where the α' phase shows nucleation and growth in grains that are not associated with grain or twin boundaries.

Fracture surfaces of the traditional fatigue specimens showed no sign of initiation due to particle, voids, or other types of inclusions at or near the surface. Cracks appeared to initiate at the surface and were semi-elliptical in nature. As such, the MSC cracks observed were considered to be semi-elliptical with a total length of 2c and a depth of c.

3.3.2 Martensite Formation

Studies have shown that the α' phase tends to develop at grain boundary/shear band intersections [70] as well as intersecting shear bands [71]. For FCC materials, dislocations typically pile up at higher angle grain boundaries, which in the case of metastable austenitic stainless steels results in γ → α' phase transformation along the boundary. Additionally, grains oriented in such a way to promote slip across more than one slip system will result in γ → α' phase transformation at intersecting shear bands within the grain. This is evident in *Figure 17* where grain C experiences γ → α' phase transformation within the grain for areas in which the rotation of the grain axis promotes slip in two systems causing the transformation within the grain rather than at a grain or twin boundary.

Phase maps were collected using EBSD on the cross section of the traditional specimens and the surfaces of the SGF specimens (*Figure 14*(c)) to investigate any differences in the transformation behavior on the surface as compared to within the specimens. Phase maps from the cross section of the traditional specimens were taken approximately 5 mm away from the crack as to not be influenced by the growing crack. The phase transformation away from the surface was

found to be comparable to the phase transformation at the surface in the absence of a growing crack. The parent austenite to martensite transformation showed the typical Kurdjumov-Sachs relationship in which $\{111\}_{\gamma} \parallel \{110\}_{\alpha'}$ and $<110>_{\gamma} \parallel <111>_{\alpha'}$. Additionally, the α' phase in the absence of the ε (HCP) phase has been reported to have a blocky irregular shape; however, when it is formed in the presence of the ε phase, it becomes more lath like [38]. Only blocky type martensite was found in all EBSD phase maps, indicating the ε phase was either non-existent or unobservable in this study. While nucleation of the α' phase was not captured in this study, nearly all α' areas were associated with either a twin boundary, grain boundary, or intersecting slip traces under cyclic loading.

3.4 Crack Initiation Mechanisms

Fractography provided little evidence into the initiation mechanisms during the fatigue tests on traditional specimens, and therefore, the interrupted test specimens were used to capture crack nucleation and MSC growth information for the stress amplitude of 330 MPa. As previously mentioned, the crack initiation stage includes nucleation and MSC growth leading up to an engineering crack with a length up to a few average grain diameters (roughly 100 - 200 μm for 304LSS). The crack initiation microstructural feature for each micro-crack was determined using EBSD. The nucleation of a micro-crack at a microstructural feature was determined for twin boundaries, grain boundaries, and inclusions by capturing the micro-crack while it was short enough to be mostly contained within or associated with a single microstructure feature. For cracks that initiated transgranularly without any evidence of microstructural inclusion, they were required to be contained within a single grain. Cracks that did not meet these criteria were not considered in the crack nucleation analysis.

3.4.1 Crack Nucleation Features

3.4.1.1 Inclusions (IN)

In this study inclusions are used in a broad sense to include intermetallic particles, voids, and oxides. For most engineering alloys, inclusions play a large role in crack initiation [72-75]. However, for the 304LSS alloy tested, this was not the case. Inclusions only accounted for roughly 10% of all analyzed crack initiation features. An example of a crack that initiated from an inclusion is shown in *Figure 18* where the loading direction is horizontal in respect to the figure. The star burst shape in *Figure 18* represents the plane traces of the {111} planes for the given orientation and the arrows highlight the direction of the crack initiation out of the void. Notice that each arrow is parallel to one of the {111} plane traces indicating the crack is likely initiating along a primary {111}<110> slip system in the FCC material.

3.4.1.2 Slip Bands (SB)

Very ductile metals with low stacking fault energy (SFE) can behave in a very similar way to very pure metals that do not have major inclusions in which cracks initiate primarily by slip. In these cases, cyclic deformation occurs due to slip in individual grains leading to an intrusion/extrusion topography at the surface. It has been shown that very narrow closed crack nuclei typically develop at the bottom of these intrusions [76]. Austenitic stainless steels generally fall into this category of low SFE metals and as such the {111} <110> slip systems play an important role in the deformation behavior. The slip behavior was observed to increase during fatigue loading of the interrupted SGF specimens in which slip traces on the surface increased in density with many eventually resulting in slip traces in two directions. These slip bands are shown

to be aligned with the {111} plane as indicated by the {111} dark lines across the grains in Figures 5 and 6. Nearly all grains containing slip traces on the surface had one primary slip system activated as indicated by the single direction of the slip band traces in *Figure 17* and *Figure 18*. However, many grains did show two active slip systems as can be readily observed by the crossing slip traces in the upper left grain in *Figure 18*.

Slip bands accounted for nearly 30% of crack initiations during the interrupted load control fatigue testing. Cracks that initiated transgranularly rather than intergranularly were almost exclusively along a {111} plane trace that contained a slip system with relatively large Schmid factors (> 0.45). These cracks were considered to be initiated by intrusion/extrusion as described by Neumann and Tonnessen [76]. In these cases, where slip bands were considered as the initiation mechanism, the cracks were mostly oriented on the surface at a large angle with the loading direction with more than half of them having an angle greater than 70° with respect to the loading direction. It should be noted, however, that observation of surface cracks gives only a two-dimensional representation. In addition, given the relatively high Schmid factors (> 0.45), the SB cracks are most likely not perpendicular to the surface.

3.4.1.3 Grain Boundaries (GB)

As previously mentioned, GB are defined as any boundary with a misorientation to its neighbor grain larger than 5° and not considered a twin boundary. The vast body of available research on the influence of microstructure on fatigue behavior for many alloys indicates the importance of gaining a better understanding of the role of GB on the crack initiation [72, 73, 76-78]. For the 304LSS alloy investigated, grain boundary cracks were largely uncommon throughout the MSC specimens tested accounting for roughly 13% of all initiation features. A grain boundary crack is shown in *Figure 19* including (a) grain orientations, (b) phases, (c) Schmid factors, and

(d) Taylor factors (loading direction is horizontal in respect to *Figure 19*). The loading direction is horizontal with respect to *Figure 19*. In this image, there is a clear indication of more than one active slip system as indicated by the slip traces in the left most grain. As seen, there are two active slip systems in this figure; one parallel to the grain boundary and one at an angle to the grain boundary.

Nearly all cracked grain boundaries were similar in that the misorientation between the two grains was large with many of the GB cracks ranging from 40° - 60°, agreeing with a previous report on the crack nucleation behavior [78]. GB with high misorientations may result in elastic incompatibilities that can lead to intergranular crack initiation [77]. A (111) plane associated with each grain was observed to be somewhat parallel with the boundary that initiated the crack as shown with the star bursts highlighting the {111} plane traces in *Figure 19*(a). The fact that the grain boundary is nearly parallel with the slip plane trace can result in higher stresses due to dislocation pileup at the grain boundary. Interestingly, these grain boundary cracks were near twin misorientation falling just outside of the Brandon criterion. It is believed that these boundaries are so near the twin misorientation that they show similar character to the twin boundary cracks, which are discussed later.

Previous research has shown that a large SFM of grain boundaries can be an indication of dislocation impingement across the boundary, resulting in stress concentrations along the boundary [66, 79]. While *Figure 19*(c) shows a relatively small SFM of 0.04, it was shown by Zhang et al. [66] that the SFM effect was highly dependent on the SFE of the material. For an austenitic stainless steel with a SFE similar to the SFE of 304LSS (15 mJ/ mm^2), the range of SFM for the transition from SB to intergranular cracking should be within 0.02 – 0.05. As evident in *Figure 19*(c), the SFM falls within the required range reported by Zhang et al. [63].

Interestingly, every grain along a cracked grain boundary that had a relatively low Schmid factor (< 0.4) also had a high Taylor factor. This is interesting because research has also suggested that high mismatches between Taylor factors result in localized strain incompatibilities, which may cause intergranular cracking [67, 79]. *Figure 19*(d) shows a low-medium (LM) Taylor factor mismatch (TFM) between the neighboring grains that nucleated the crack. While not all grain boundary cracks had large TFM values, nearly every grain boundary crack had at least one high Taylor factor associated with it indicating the importance of the misorientation between grains in crack nucleation.

3.4.1.4 Twin Boundaries (TB)

Crack initiation at twin boundaries has been previously observed [14, 16, 67, 80], and is somewhat surprising due to the low energies associated with twin boundaries. The elastic incompatibility on the surface of a twin pair results in high shear stress concentrations at the interface of these boundaries which can lead to crack initiation. For FCC materials, the Σ3 twins run parallel to a {111} slip plane for both grains along the twin boundary, and thus, local plasticity arises along a dominant slip system (i.e. {111}<110>) parallel to the twin [14]. Neumann and Tonnessen [76] showed that TBs cracked due to persistent slip bands near the high localized shear stresses at the TBs which had a modified Schmid factor higher than 0.44.

Twin boundaries showed the highest frequency in crack initiation for this 304LSS alloy where they accounted for nearly half of the crack initiation sites. Cracks that initiated at twin boundaries showed the tendency to occur along the plane of maximum shear stress (≈45° from loading axis), but quickly propagated into the adjacent grains along the plane of maximum principal stress. This result is in agreement with previous research in which simulations showed that TBs oriented at 45° from the loading direction were susceptible to early intergranular fatigue

crack formation as a result of strain localization along the TB [81]. A technique described elsewhere [80] has been shown to give reasonable results when determining if a twin boundary is coherent or incoherent past the surface interpretation provided by EBSD analysis. In this case, the twin trace normal is plotted on a {111} pole figure for both grains adjacent to the twin boundary. If the twin trace normal coincides with the incident planes, then the twin can be called coherent with reasonable certainty. The Brandon criteria allows for slight deviations in misorientation such that twin trace normals that fall slightly off of the coincident planes can still be considered coherent. This method is shown in *Figure 20* where the {111} incident planes for the adjacent grains along the twin boundary are plotted on a {111} pole figure (loading direction is horizontal in respect to *Figure 20*). The boundary trace normal is plotted from the center of the pole figure and falls within the vicinity of the coincident planes indicating the twin boundary is coherent. From this method, it was found that every crack initiated from a twin fell within the range given by the Brandon criterion to be considered coherent.

3.4.1.5 Crack Nucleation Summary

As discussed in the previous sections, crack nucleation occurred at many microstructural features. *Figure 21* details the frequency of each microstructural feature associated with the nucleation of the analyzed micro-cracks along with comparison of SFM, TFM, and crack initiation angles with respect to loading direction. *Figure 21*(a) clearly indicates that, similar to the initiation mechanism for the high cycle fatigue regime [14], TB are the dominant crack initiation feature for the transitional fatigue regime. However, SBs also show a significant initiation frequency compared to twin boundaries.

As previously mentioned, GBs that contain relatively large SFM values can be indicative of plastic incompatibility, in addition to any elastic incompatibilities. The added stress

concentrations along the boundary can ultimately lead to intergranular crack initiation along the GB. *Figure 21*(b) presents the SFM for grain and twin boundaries. Cracked twin boundaries showed on average lower SFM values with roughly 60% of them having a SFM of 0 – 0.01 as compared to grain boundaries with almost 67% of them having a SFM of 0.03 – 0.04. While the SFM for grain boundaries may appear to be relatively low as well, for materials with low SFE (such as 304LSS), it was shown that a lower difference in Schmid factors (0.02 – 0.04) would still promote intergranular cracking rather than slip band cracking [79]. Additionally, high TFM are indicative of fatigue crack susceptibility due to strain incompatibilities along the boundary. *Figure 21*(c) shows similar behavior when comparing TFM of twin boundaries and grain boundaries. Twin boundaries tended to initiate when a TFM was present, which is in agreement with previous research [16]. The fact that GB cracks showed similar TFM across their boundary as TB cracks could be the result of many cracked GBs (approximately 40%) having misorientations very close to the Σ3 twin boundary misorientation, falling just outside of the Brandon criterion. Additionally, more than 50% of the GB cracks that had similar misorientations as TB showed similar crack initiation angles relative to the loading direction as TB cracks. It should be noted, however, that the sample size of GB cracks compared to TB and SB cracks was quite small.

Though TB and SB were observed to be the most predominant crack initiation feature for 304LSS in this study, the crack initiation mode between these features differs. Twin boundaries generally cracked as a result of strain localization which are triggered by strain incompatibilities along the boundaries with most of them being orientated on the surface around the direction of maximum shear (45°) as indicated in *Figure 22*(d). Slip bands, however, initiated almost exclusively near perpendicular (90°) on the surface; however, it must be noted that EBSD gives only a two-dimensional representation and the crack may not be fully perpendicular below the

surface. In this case, the crack initiation behavior appears to be similar to the one described by Neumann and Tonnessen [76].

Grain boundaries showed a mixture of both 45° and 90° from the direction of loading. The observed differences in the crack initiation angles for the most frequent initiation features highlights the significance of twin and grain boundary orientation on the fatigue crack initiation of 304LSS. These findings indicate that the fatigue behavior of 304LSS could be potentially improved by minimizing the number of twin boundaries within the material and by controlling their relative angles with respect to loading direction through proper manufacturing and post-manufacturing processes.

3.4.2 Microstructurally Short Crack Growth Behavior

Martensite was rarely able to be unambiguously determined as the source of crack initiation and as such showed the lowest frequency of all crack initiation features. In general, most initiation sites had very little transformation occurring until a crack was more than a grain diameter in length. Roth et al. [18] also reported similar results for the high cycle fatigue behavior of a 304LSS alloy. All cracks showed development of α' transformed areas near the crack tip. Typically, the α' phase began to develop at the crack tip as the crack propagated to a length of 15 – 20 μm. As the crack grew through the microstructure and developed a larger plastic zone ahead of the crack tip, martensitic zone sizes grew as well. As for crack nucleation, martensite formation did not appear to play a significant role. However, as discussed in the introduction, crack initiation includes the life to nucleate a crack and the subsequent MSC growth up until a crack reaches a length of a few average grain sizes. Previous research has shown that fatigue crack growth rates are higher in the

martensitic phase as compared to the austenitic phase [43]. For this reason, it was of particular importance to study the effect of the transformed α' zone at the crack tip on the MSC rates.

An α' zone size was calculated as the average diameter measured across the transformed portion of a crack tip as shown in *Figure 22* (the loading direction is horizontal with respect to the figure). Multiple measurements were taken perpendicular to the change in crack length, Δ2c, from the previous cycle. In many instances, the crack propagated into an area of previously transformed martensite which resulted in a large increase in zone size for the given measurement. A representation of one of these areas can be seen directly below the zone size measurement in *Figure 22*. These areas were included in the average α' zone measurements to account for their effects on the crack growth behavior. These measurements were then averaged to obtain an average zone size for the propagating crack at each interruption schedule along with the calculated standard error.

The crack growth data compared to α' zone sizes is given in *Figure 23* where each data point is taken at the end of every interruption schedule for a single crack. For analysis, at least two and up to four cracks were included for each initiation type in order to obtain MSC growth behavior for multiple cracks shown in *Figure 23*. Additionally, all analyzed micro-cracks were far enough from other cracks as to not be influenced by other growing cracks. The data set for *Figure 23* contains the largest crack observed for each initiation feature in order to compare the MSC growth rates for the fastest growing crack in each category. The α' zone size is plotted versus crack length in *Figure 23*(a) indicating an increase in α' zone size with increasing crack length regardless of the initiation mechanism involved**.** This zone size increase can be attributed to the growing plastic zone at the crack tip promoting phase transformation around the crack front as described by Roth et al [18]. It can be seen in *Figure 23*(a) that the smallest α' zone sizes for GB and TB cracks were similar in size to those for the largest slip band and inclusion initiated cracks. This is a result of

GB and TB cracks having longer crack lengths (2c) for a given interruption schedule, and thus, maintaining larger α' zone sizes throughout their associated fatigue life.

The size of the transformed zone around the crack tip showed some level of correlation to MSC growth rates up to crack lengths of 500 μm, as indicated in *Figure 23*(b). Comparing *Figure 23*(a) and (b), it can be observed that the increase in MSC growth rates coincide with increasing crack length. It can also be noticed from *Figure 23*(b) that the α' zone size for GB and TB cracks tended to develop at a much higher rates compared to slip band and inclusion initiated cracks. Again, this is a result of GB and TB cracks having longer lengths as compared to other microstructural features for a given cycle count, indicating that they are susceptible to earlier crack initiation compared to other microstructural features. What is interesting, however, is the similarity of many GB to TB cracks including their orientation, nucleation behavior, and MSC growth behavior. It was previously mentioned that many GB cracked showed a similar misorientation across the boundary to cracked TB, with just enough deviation to fall outside of the Brandon criteria for Σ3 twin boundaries. The GB cracks that were similar to TB cracks showed approximately 33% longer crack lengths than other GB cracks for a given cycle. These GB cracks had very similar crack lengths and growth rates as TB cracks, as shown in *Figure 23*. Additionally, GB and TB cracks were 50% – 65% longer than other cracks for a given cycle, further indicating that these types of cracks initiate earlier and as a result grow faster than other microstructural features. These results show that crack initiation life for a transition fatigue regime is more sensitive to crack initiation feature than the martensitic transformation zone that occurs at the crack front. Specifically TB cracks and GB cracks with similar misorientations to twin boundaries were observed to have much longer lengths than other microstructural features for a similar number of cycles indicating that these cracks nucleated and developed faster than other microstructural

features. As such, grain and twin boundary cracks reach the end of the crack initiation stage well before cracks from other initiation mechanisms, and most likely, are the initiation features to form a dominant crack to failure.

3.5 Conclusions

Through the use of SEM and EBSD, several micro-cracks were observed and analyzed to understand the initiation mechanisms in the transitional fatigue life regime. The effect of $\gamma \rightarrow \alpha$' phase transformation on the crack initiation behavior was also investigated. The following conclusions can be made regarding the nucleation and MSC growth of a micro-crack of 304L stainless steel:

1. Martensitic transformation was found to occur during fatigue loading at 330 MPa, which is within the transition fatigue life regime. Localized plasticity at the crack tip results in martensite formation around the crack tip for cracks reaching 10 μm – 50 μm.
2. For fully reversed fatigue loading within the transition fatigue life regime, twin boundaries were the leading crack initiation feature. However, other microstructural features, such as slip bands and grain boundaries, contributed to crack initiation as well.
3. Slip bands were shown to be the second most frequent crack initiation feature. Slip band cracks, however, reached the end of the crack initiation stage later in the fatigue life as compared to twin and grain boundary cracks. Cracks that initiated from twin and grain boundaries were roughly 66% longer than cracks that initiated from slip bands. Therefore, twin and grain boundary cracks will most likely be the ones to grow to failure.
4. Twin boundaries predominately cracked at an angle close to 45° to the loading direction while slip bands were nearly perpendicular (90°) to the loading direction. Grain boundary cracks showed a tendency to initiate at both 45° and 90° in relation to the loading direction.

5. Martensite zone size at the crack tip was found to correlate to the crack length in the crack initiation stage as a result of the developing plastic zone as the crack grows in size. Grain and twin boundary cracks were found to initiate at an earlier stage of fatigue life and develop larger α' zone sizes in the initiation stage.
6. Crack initiation life was found to much more sensitive to initiation feature than martensite formation near the crack. Specifically, twin boundaries showed the greatest frequency of all crack initiation features and were the most likely to lead to a dominant crack as a result of an earlier crack initiation as compared to the other microstructural features. Additionally, grain boundaries with similar misorientations as twin boundaries initiated cracks in a similar manner to twin boundary cracks.

In summary, the crack initiation behavior of 304L stainless steel is dominated by twin boundaries in the transition fatigue regime. While other microstructural features such as slip bands showed significant initiation sites, the MSC growth from these features was slow as compared to that of TB and GB micro-cracks. Although limited in number, GB micro-cracks that initiated in a similar fashion as TB and grew at similar rates. Finally, these results show that the crack initiation life could be improved by limiting the number of TB or controlling the direction of them in relation to the loading direction of the material through proper manufacturing and/or post manufacturing processes.

Acknowledgements

Much of this work was done while Jonathan Pegues and Nima Shamsaei were at Mississippi State University.

Table 4: Chemical composition of austenitic stainless steel in % weight (remainder Fe).

% C	% Co	% Cr	% Cu	% Mn	% Mo	% N	% Ni	% P	% S	% Si
0.029	0.150	18.063	0.450	1.347	0.384	0.072	8.588	0.032	0.030	0.283

Table 5: Reported mechanical properties of the as-received 304L stainless steel.

Elastic Modulus (GPa)	Yield Stress (MPa)	Tensile Strength (MPa)	Elongation (%)
189	276	636	55

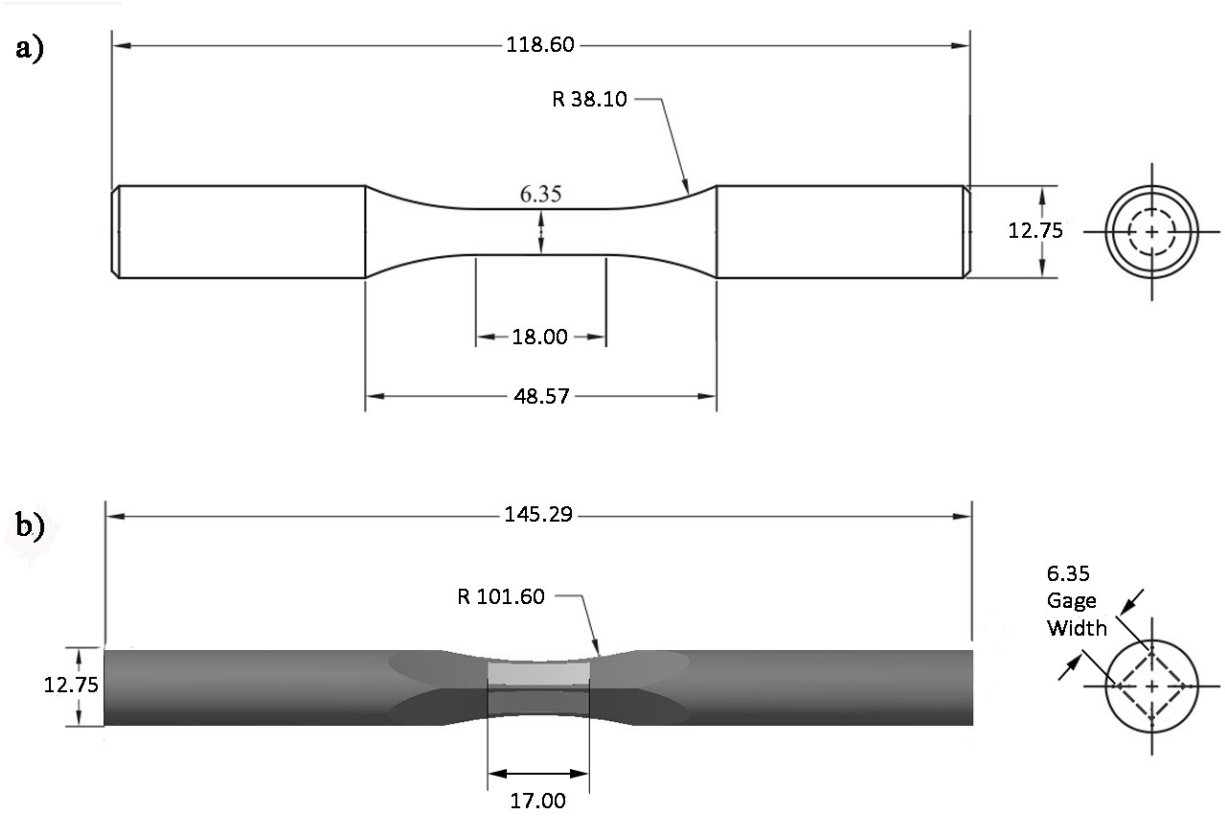

Figure 13: Specimen design for traditional cylindrical fatigue specimen with uniform gage section and b) square gage fatigue specimen with rounded corners and electrolytically polished surface. All dimensions are in mm.

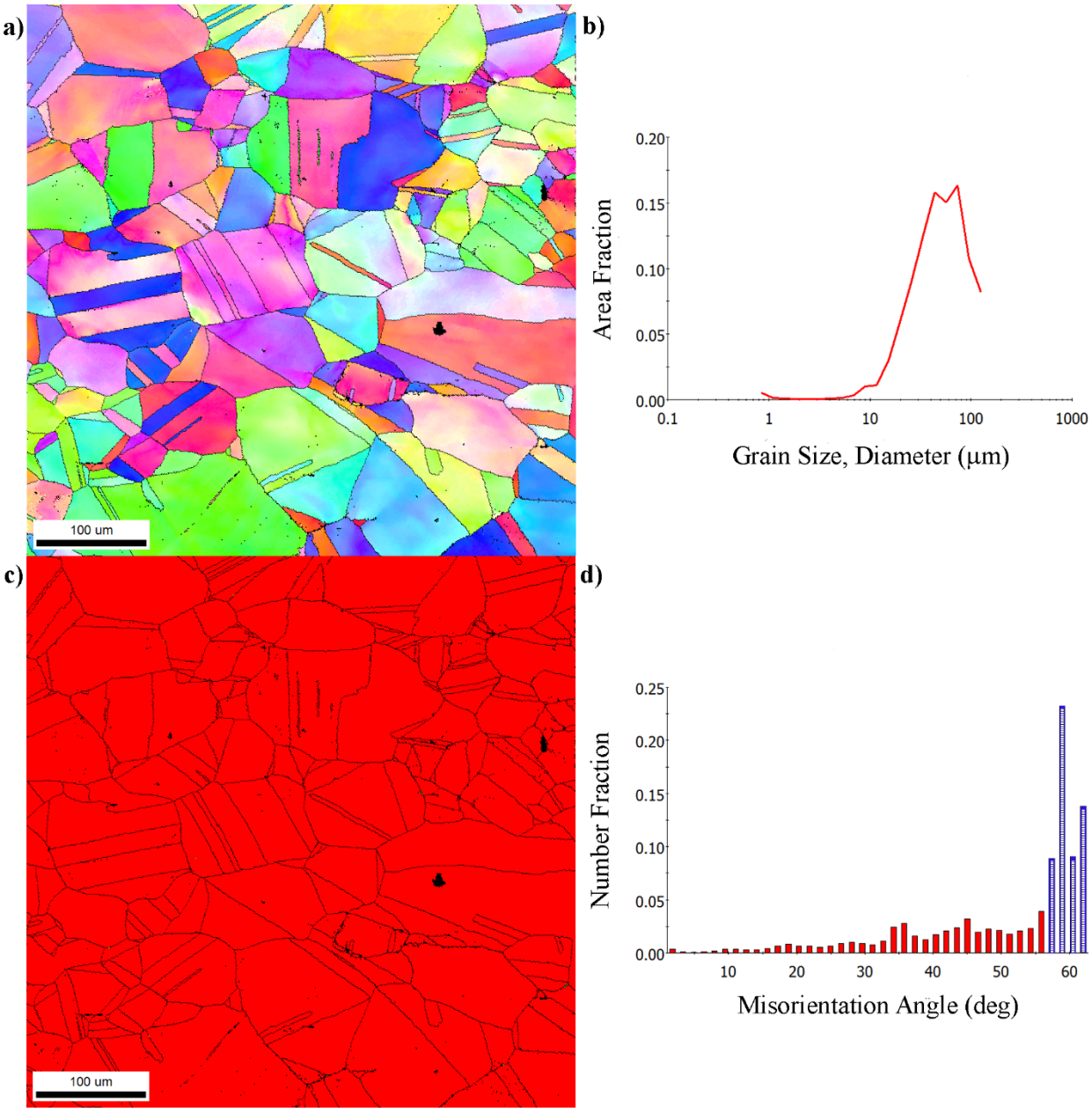

Figure 14: As-received microstructure detailing a) grain orientation in the normal direction, b) grain size distribution, c) phase distribution, and d) grain boundary misorientation.

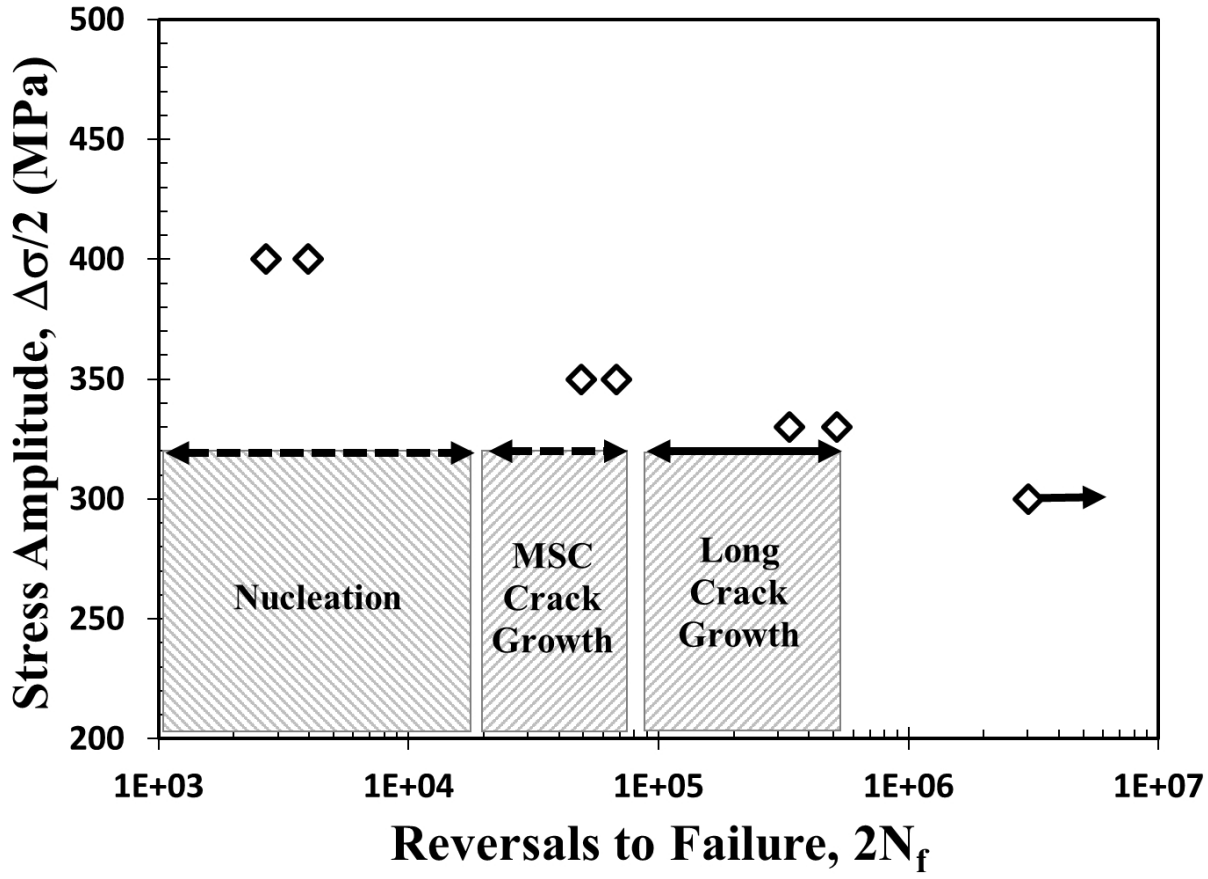

Figure 15: Stress life (S-N) plot including the crack nucleation, microstructurally short crack (MSC) growth, and long crack growth for a stress amplitude of 330 MPa.

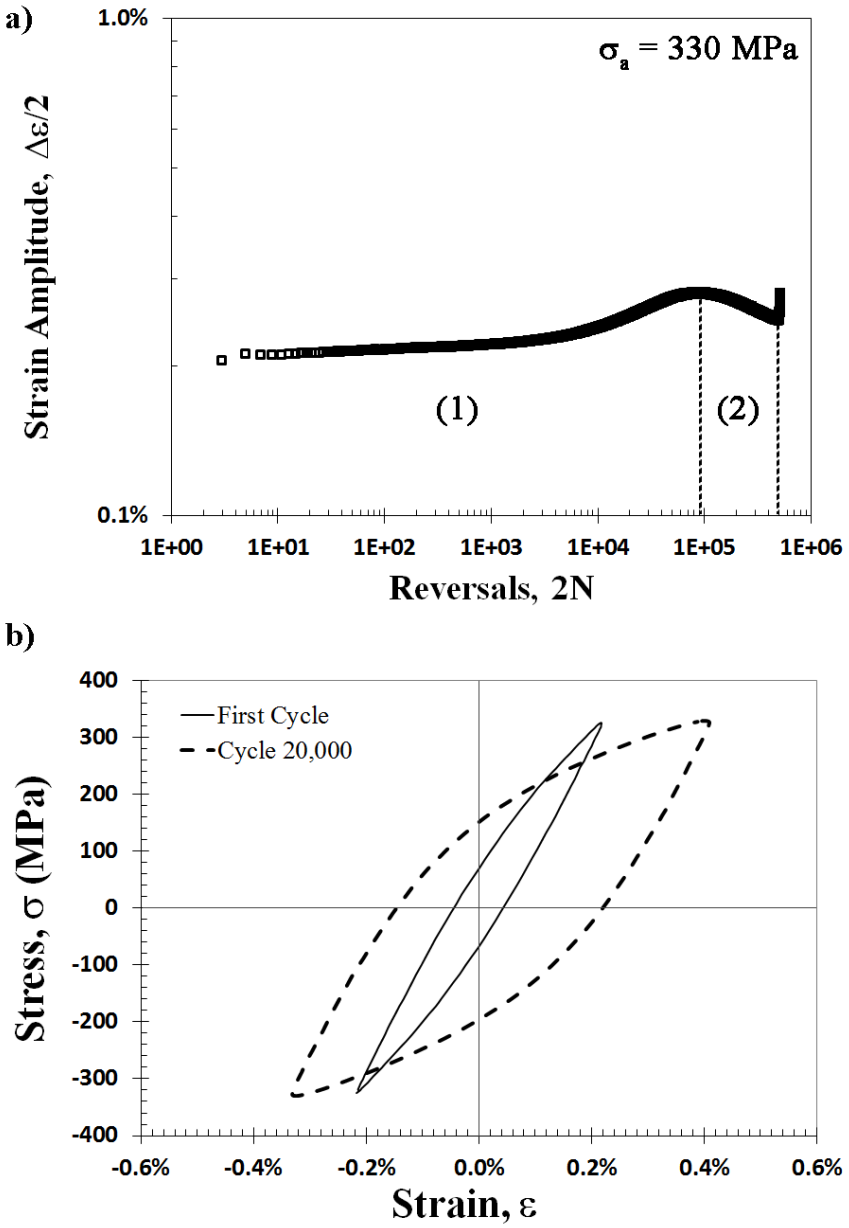

Figure 16: Strain response for a fully reversed fatigue test at a stress amplitude of 330 MPa detailing a) the cyclic softening stage (1) and cyclic hardening stage (2) and b) the stress-strain hysteresis loops for the first cycle and cycle 20,000.

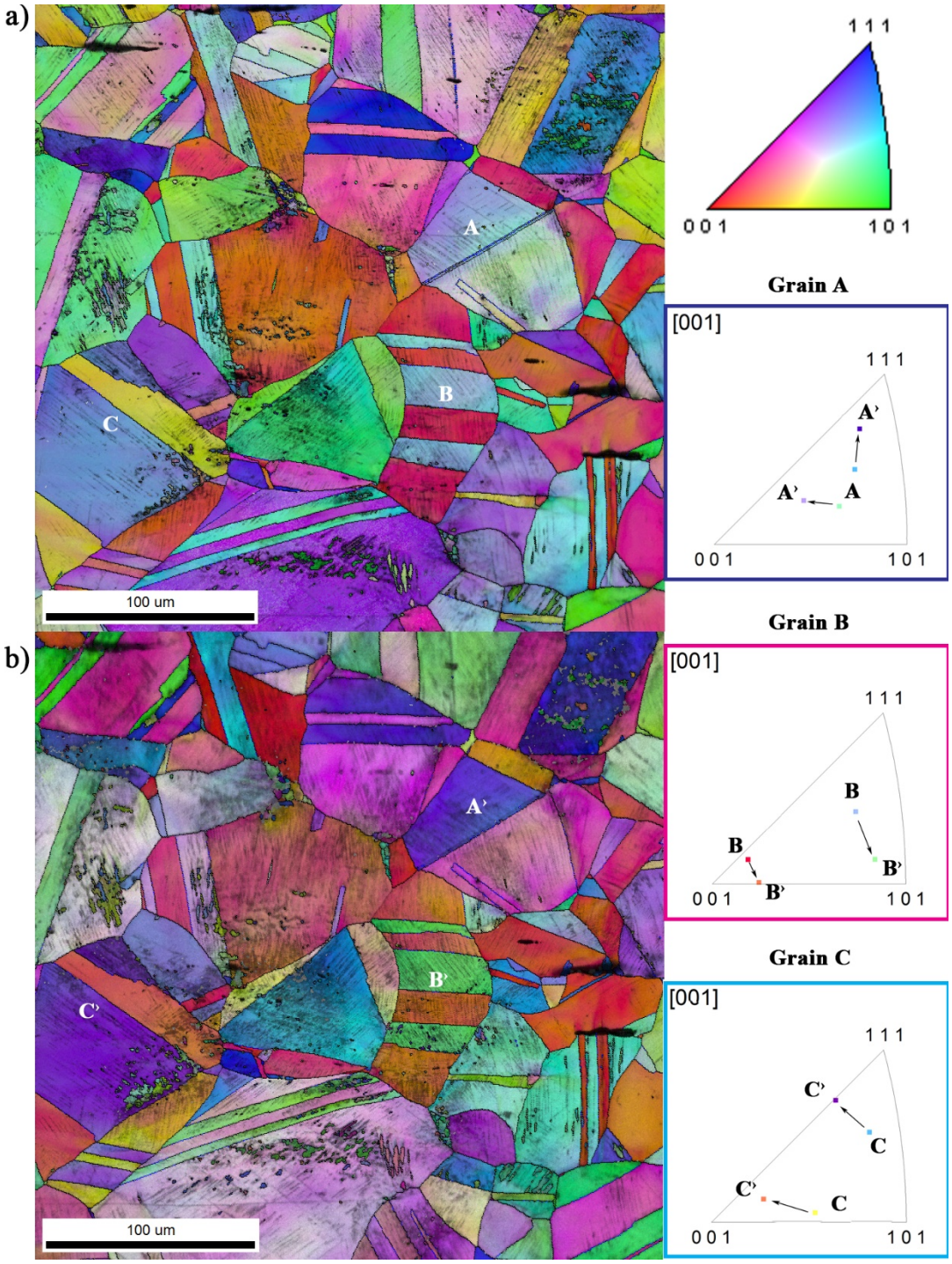

Figure 17: Inverse pole figure maps in the normal direction of a selected area showing the rotations of the grains due to cyclic loading to accommodate multiple slip systems within each grain as shown on the IPF triangles (a) after 20,000 cycles and (b) after 30,000.

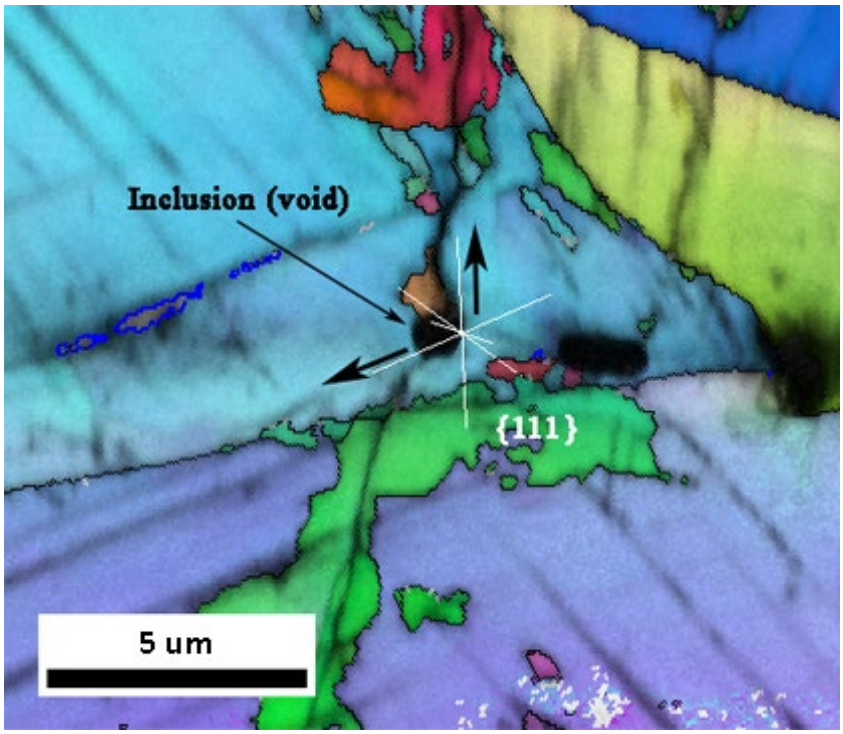

Figure 18: Inverse pole figure maps collected by EBSD showing crack initiation from an etched out δ-ferrite inclusion.

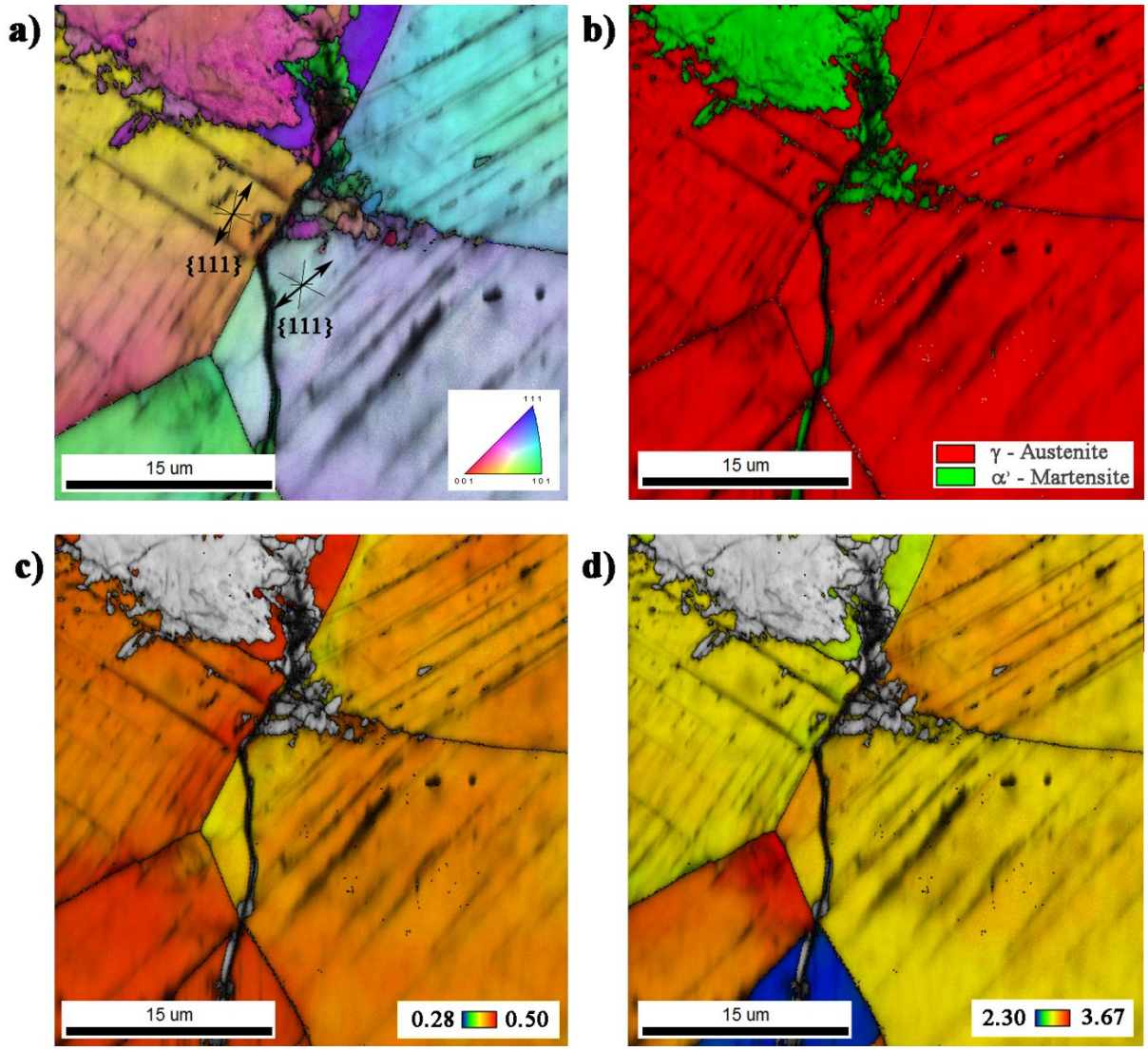

Figure 19: EBSD maps for a grain boundary crack showing a) inverse pole figure, b) phase map, c) Schmid factor map, and d) Taylor factor map.

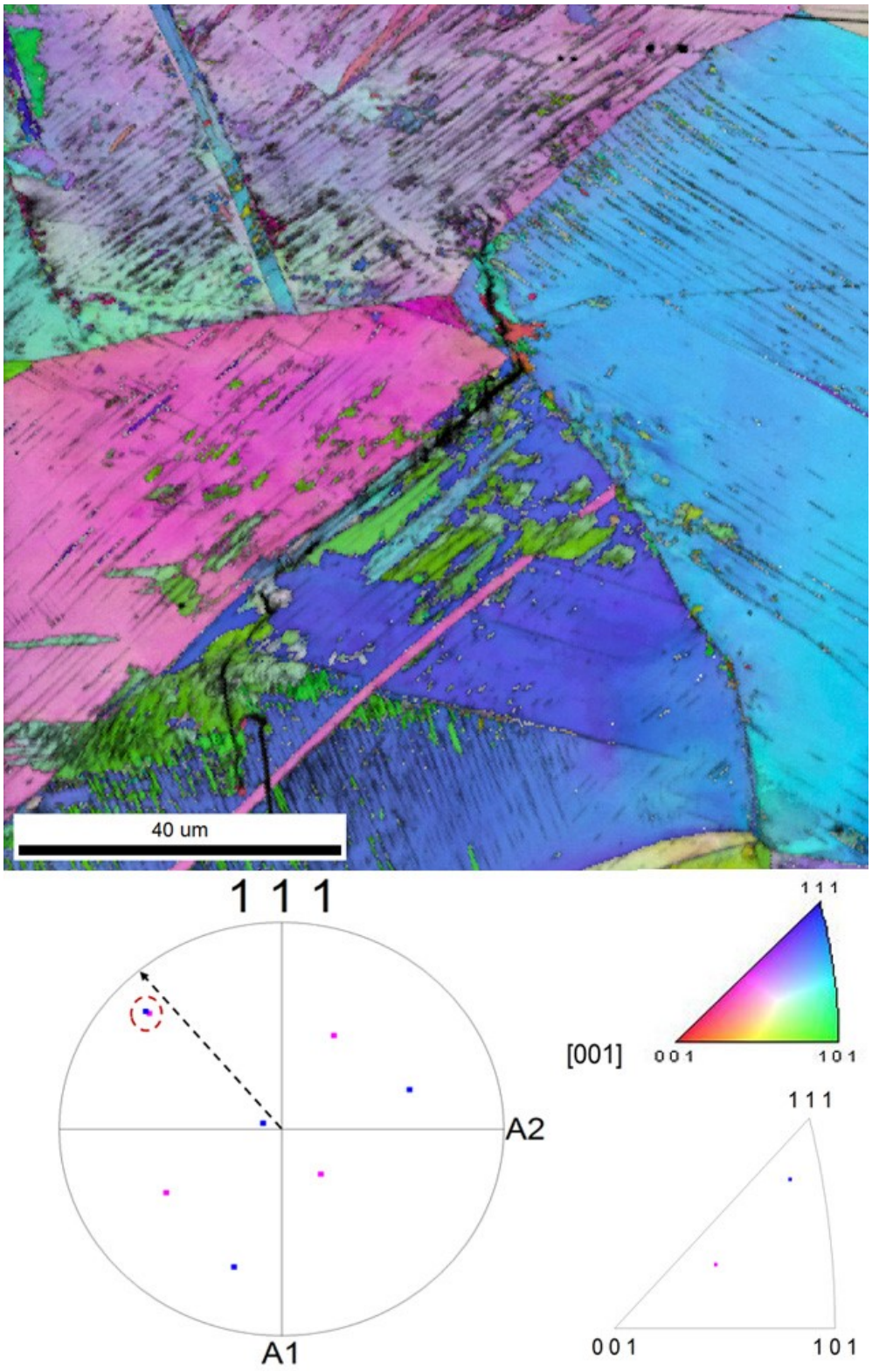

Figure 20: Inverse pole figure map of a cracked coherent twin boundary.

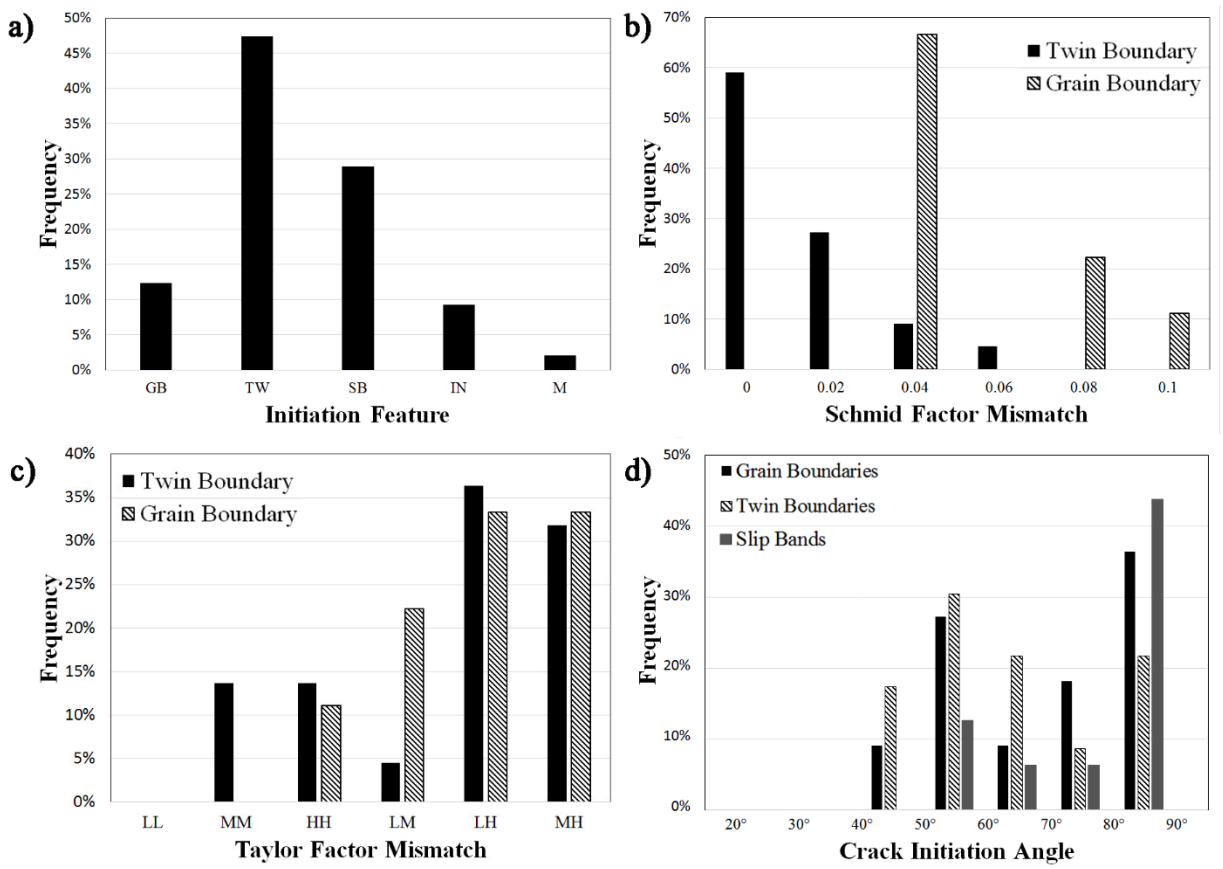

Figure 21: Histograms showing the relative frequency of a) initiation features, b) Schmid factor mismatch, c) Taylor factor mismatch, and d) crack initiation angle.

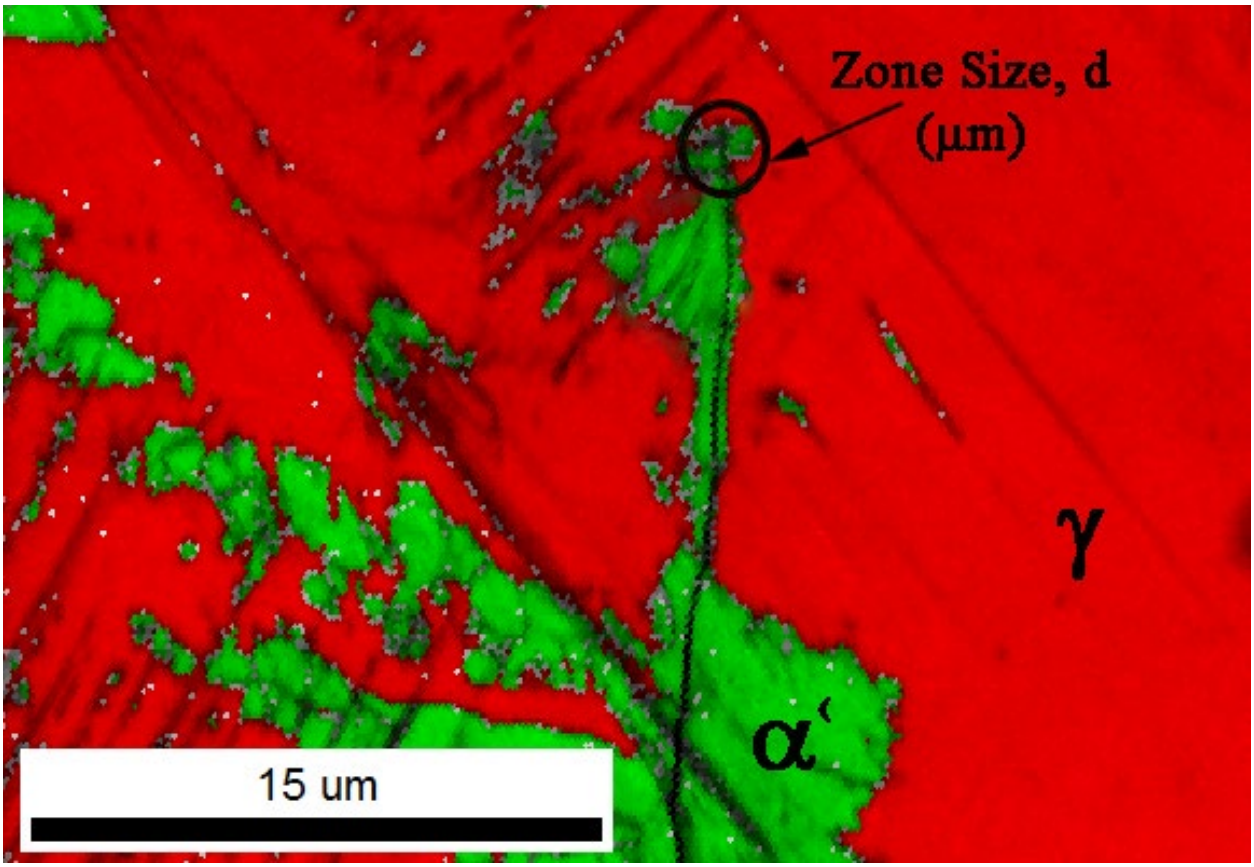

Figure 22: Representation of the transformed α' zone size measured across the transformed crack tip.

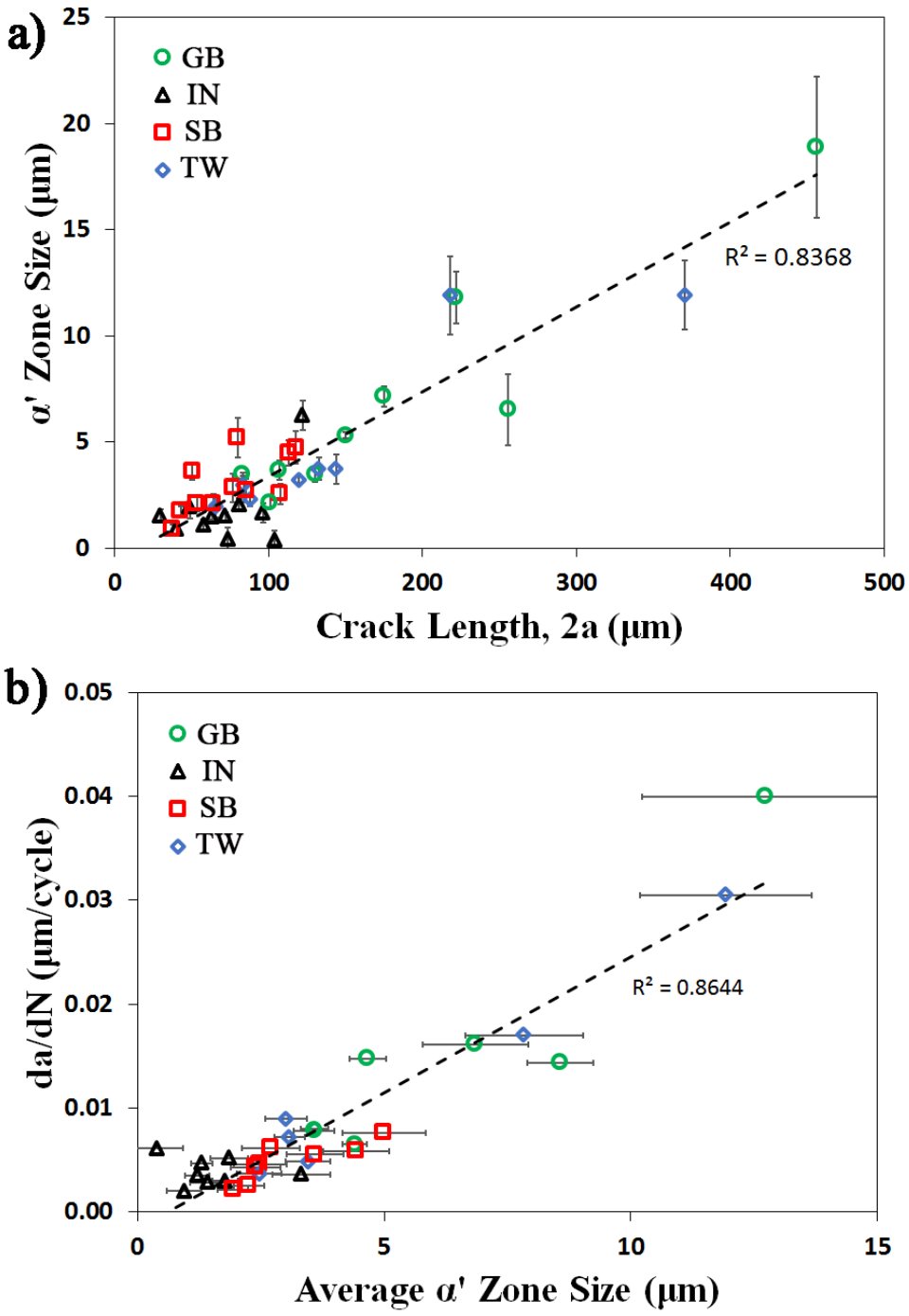

Figure 23: MSC growth data showing a) α' zone size versus crack length, and b) MSC crack growth rates versus average α' zone size.

Chapter 4: Additive Manufacturing of Fatigue Resistant Austenitic Stainless Steels by Understanding Process-Structure-Property Relationships

The following chapter has passed rigorous peer-review process and has been published in Materials Research Letters in 2019.

Additive manufacturing of fatigue resistant austenitic stainless steels by understanding process-structure–property relationships

Authors: Jonathan W Pegues, Michael D Roach, Nima Shamsaei

Publication date: 2019

Journal: Materials Research Letters

Volume: 8

Issue: 1

Pages: 8-15

Publisher: Taylor & Francis

Additive Manufacturing of Fatigue Resistant Austenitic Stainless Steels by Understanding Process-Structure-Property Relationships

Jonathan W. Pegues[a,b] Michael D. Roach[c] and Nima Shamsaei[a,b]

[a] *Department of Mechanical Engineering, Auburn University, Auburn, AL 36849, USA;*

[b] *National Center for Additive Manufacturing Excellence (NCAME), Auburn University, Auburn, AL 36849, USA;*

[c] *Department of Biomedical Materials Science, University of Mississippi Medical Center, Jackson, MS 39216, USA*

Corresponding author:

Tel: 334-844-4839

Email: shamsaei@auburn.edu

Abstract

The limited understanding of additive manufacturing process-structure-property inter-relationships raises some concerns regarding the structural reliability, which limits the adoption of this emerging technology. In this study, laser beam-powder bed fusion is leveraged to fabricate an austenitic stainless steel with a microstructure containing minimal known crack initiation features. Ex-situ microstructural observations of the crack initiation features and mechanisms are carried out for interrupted fatigue tests via electron backscatter diffraction mapping of the micro-cracks. Results show that the additive manufactured stainless steel alloy has improved fatigue resistance compared to its wrought counterpart as a result of the unique microstructural features.

Keywords: Laser beam-powder bed fusion; Crack initiation; Microstructure; Twin boundary; Cyclic deformation

Impact Statement

Using an experimental ex-situ microstructural investigation, the fatigue resistance of additive manufactured 304L stainless steel was shown to be superior to the wrought counterpart by avoiding the typical failure mechanisms.

4.1 Introduction

Additive manufacturing promises to revolutionize the fabrication process of structural components in several industries including aerospace, biomedical, defence, energy, and automotive. The layer-by-layer fabrication process results in a wide design-space with the freedom to create complex geometries and, more importantly, the ability to have direct localized control of the thermal history. There is an intimate relationship between the thermal history and the resulting microstructure [8], such that tailored, or even functionally graded, microstructures may be realized through additive manufacturing [82]. For example, in areas where high strength and resistance to fatigue crack initiation (FCI) is required, high cooling rates may be beneficial to produce finer microstructures. On the other hand, as larger grains are beneficial for areas where crack growth is critical, a reduction in the cooling rate can lead to a coarsening of the microstructure [83].

The extension of additive manufacturing to fatigue critical applications has been hindered by process induced defects such as lack-of-fusion (LoF), gas entrapped pores, and surface roughness [1, 4, 84]. Defects act as stress concentrators inducing early FCI, severely limiting the potential for producing reliable, fatigue resistant additive manufactured (AM) parts. This study aims to better understand process-structure-property relationships as they relate to the fatigue performance of LB-PBF 304L stainless steel (304LSS). Such understandings can be leveraged to enhance the localized microstructure at critical areas and to fabricate more fatigue resistant parts. To date, the majority of research efforts regarding structure-property relationships of AM parts have focused on understanding the structure-property relationships as they are related to the measured quality of the material based on the processed induced defects [85-89]. This work, however, focuses on selection of materials that are less sensitive to defects to better understand the microstructure's role in FCI of AM materials. The results presented in this study give early

insight into the true potential of additive manufacturing to produce targeted microstructure for application specific desired properties.

4.2 Crack Initiation in Austenitic SSs

Austenitic stainless steels (SSs) in their wrought form are known to be more susceptible to FCI at annealing twin boundaries (Σ3-TB) and high angle grain boundaries (HAGB) than nano/micro-scale defects such as intermetallic inclusions and voids [14, 15, 90, 91]. Austenitic SSs can become sensitized in the temperature range of 425°C to 850°C; therefore, these alloys are material is typically formed through cold working methods followed by solution annealing to recover their ductility [23, 24]. The annealing procedure results in a high density of Σ3-TB in the material, increasing the susceptibility to early life FCI [15, 92].

The deformation behaviour at Σ3-TB and HAGB has been shown to result in both elastic and plastic incompatibilities across the boundary [15, 60, 90, 91, 93-95]. For low applied stresses, such as those in the high-cycle fatigue (HCF) regime, the small differences in elastic deformation for Σ3-TBs oriented near 45° from the loading direction result in elastic mismatches across the boundaries. The resulting high localized stresses near these specific Σ3-TBs promote FCI along the boundary. This FCI behaviour can be exacerbated when higher loads are applied resulting in larger regions of localized stress and even greater slip activity near the Σ3-TB, expediting the crack formation. Additionally, HAGB are also capable of promoting FCI in wrought austenitic SSs as dislocations are not easily transferred across the grain boundary. As these dislocations pile up, edge dislocations of different signs attract each other resulting in the accumulation of vacancies and the formation of micro-cracks [96].

While microstructural features such as Σ3-TB/HABG are difficult to avoid in the manufacturing of wrought materials, additive manufacturing provides a means to produce net shaped/near-net shaped parts without the need for post-processing steps such as forming and /solution annealing. Austenitic SSs exhibit exceptional toughness and have been successfully implemented in laser beam-powder bed fusion (LB-PBF) processes [97, 98]. The cooling rates associated with the LB-PBF process result in minimal time to cool through the sensitization temperature range of these SSs, which are therefore not considered to be susceptible to sensitization in the as-fabricated condition.

4.3 Ex-situ Experiments to Observe FCI Mechanisms

Rectangular LB-PBF specimen blanks with dimensions of 13 mm x 13 mm x 70 mm were fabricated horizontally on an EOS-M290 and stress relieved at 400°C for 1 hr before being removed from the substrate. The process parameters followed manufacturer recommended parameters for 316L SS with a laser power of 195 W, scan speed of 1083 mm/s, and a hatch distance of 90 μm. The powder feedstock was provided by LPW with a particle size distribution of 15 μm – 45 μm and composition given in *Table 6*. Specimens were then machined to a cylindrical uniform gage section following ASTM-E606 [99]. The specimens were polished in the longitudinal direction using a series of silicon carbide grinding papers to a mirror finish. Non-traditional square gage specimens were also machined from specimen blanks with dimensions 13 mm x 13 mm x 104 mm to investigate the FCI mechanisms associated with LB-PBF 304LSS. The surfaces of these crack initiation specimens (CIS) were electro-polished to provide a pristine surface for electron backscatter diffraction (EBSD) analysis, as previously described for the wrought material [15].

All standard cylindrical uniform gage section specimens were tested until failure on an MTS servo-hydraulic test frame with a 100 kN capacity, some under force-controlled and some under strain-controlled conditions. In addition to fatigue testing, quasi-static tension tests were performed until failure at a strain rate of 0.001 s^{-1}. The CIS were tested under force-control only and were interrupted periodically and investigated using a Zeiss FE-SEM with an EDAX EBSD detector and OIM software. Micro-cracks were located and mapped using EBSD to observe the microstructural characteristics associated with FCI.

4.4 Establishing Process-Structure-Property Relationships

Differences in microstructure in relation to the drawing and build direction for wrought and LB-PBF(304LSS), respectively, are shown in Figure 1. The YXZ plane relates to the faces which were perpendicular to the build direction while the ZXY plane relates to the faces parallel to the build direction. The LB-PBF microstructure analysis revealed a strong <011> texture as a result of the <001> easy growth direction and the high solidification rate [100-102]. Additionally, the LB-PBF microstructure evolution results in a much finer average grain size (12 μm and 13 μm in the YXZ and ZXY planes, respectfully) than the wrought counterpart (54 μm equiaxed). The LB-PBF material also showed a high density of low angle grain boundaries (LAGB) (>15°) and a low density of HAGB (>45°) and Σ3-TB (~60°), as shown by the misorientation histograms in Figure 1. This contrasts with the wrought material which shows a higher density of HAGB and Σ3-TB boundaries. The measured grain boundary lengths and number fractions for LAGB (5° - 15°), grain boundaries in the range of 15° - 45°, HAGB (45° - 54°), and Σ3-TB are given in *Table 7*.

The cyclic deformation behaviour of wrought 304LSS results in complex stress responses as affected by microstructural characteristics and evolution [103]. The cyclic deformation

behaviour for the LB-PBF 304LSS under strain-controlled conditions, given in Figure 25, is similar to what had been observed for its wrought counterpart [103]. The stress response (force divided by cross-sectional area) in Figure 25a reveals three distinct deformation stages. Initial work hardening is observable for strain amplitudes lower than 0.5% and occurs during the first 10-100 cycles. All stain amplitudes showed cyclic softening, which has been shown to occur in 304LSS due to the geometric softening effect where the cyclic deformation behaviour results in a rotation of the grain axis towards the loading axis [15]. The final stage is characterized by a second cyclic hardening regime which has been termed as secondary hardening [54]. This stage has been correlated to the deformation induced martensitic phase transformation that occurs for 304LSS [103].

The complex stress response of 304LSS results in non-stabilized hysteresis loops during cyclic loading as the stress amplitude evolves through the related deformation stages. The half-life hysteresis loops are presented in Figure 25b along with the quasi-static tensile behaviour in the same strain range. The initial work hardening of the material at the strain amplitude of 0.2% results in a higher peak stress at half-life compared to the quasi-static tensile behaviour. The next strain amplitude step of 0.5%, conversely, falls below the quasi-static stress-strain curve. Comparing the 0.5% strain amplitude hysteresis loop to the stress response given in Figure 25a reveals that the initial work hardening stage occurs earlier in the fatigue life than the 0.2% strain amplitude and the subsequent cyclic softening in the 0.5% test results in the hysteresis loop deteriorating below the quasi-static stress-strain curve. Increasing the strain amplitude results in further cyclic softening as observed for strain amplitudes of 0.75% and 1.0%. It must be noted, however, that the stress response is not stable throughout the fatigue life and that, depending on the cycle at which the hysteresis loop is captured, different cyclic stress-strain curves can be obtained.

Figure 25c shows the cyclic stress-plastic strain relationship for both wrought and LB-PBF 304LSS. The LB-PBF material shows a slightly lower cyclic hardening rate, as indicated by the lower slope of the curve, as well as a lower fatigue strength coefficient (σ_a at ε_{a-p} = 1.0%). However, the LB-PBF material exhibits a much higher cyclic yield strength (σ_y' = 424 MPa) than the wrought material (σ_y' = 334 MPa). This is mostly attributed to the finer microstructure and smaller slip length of the LB-PBF material.

The quasi-static tensile engineering stress-strain and fatigue behaviour of the LB-PBF material in comparison to its wrought counterpart are presented in *Figure 26*a-c. In *Figure 26*a, the LB-PBF material shows a slightly higher tensile yield strength and elongation to failure with a slightly lower ultimate strength. The increased yield strength can be related to the finer microstructure observed for the LB-PBF material. It should be mentioned, however, that the wrought material was evaluated using standard E8 test specimen geometry while the AM materials was evaluated using the cylindrical uniform gage section fatigue specimens that do not strictly meet the ASTM E8 [104] requirements.

The strain-life fatigue data and curves are shown in *Figure 26*b. Surprisingly, the strain-life fatigue results show the LB-PBF material exhibiting slightly better fatigue resistance in the low-cycle fatigue (LCF) regime, while the intermediate and HCF behaviour is very similar to the wrought counterpart. The improved LCF resistance can also be explained by the finer microstructure and higher cyclic yield strength of the LB-PBF material making it more resistant to slip, resulting in a reduced level of extrusions and intrusions on the surface. The similarity of the wrought and LB-PBF HCF fatigue behaviour suggests that defects such as LoF and gas entrapped pores, which typically deteriorate the HCF performance of most AM materials, are not

greatly influencing the LB-PBF 304LSS .

The stress-life fatigue data and corresponding Basquin curves are shown in *Figure 26*c. Remarkably, under force-controlled conditions, the LB-PBF 304LSS exhibited significantly better fatigue resistance across all stress levels. The fatigue life of LB-PBF material for any given stress amplitude was one-two orders of magnitude longer than the wrought material. While most AM materials fail under cyclic loading due to the presence of process induced defects [4, 87, 105, 106], the majority of the dominating cracks in the LB-PBF 304LSS specimens appear to initiate at the surface in a similar fashion to what was observed for the wrought counterpart. *Figure 27* details two fracture surfaces from (a) strain control testing at $\varepsilon_a = 0.3\%$ and (b) force control testing at $\sigma_a = 400$ MPa. In both cases a dominant crack initiates at the surface without any indication of the presence of defects (indicated by 1 in image) and coalesces with a smaller crack which shows evidence of FCI at a defect (indicated by 2 in image). Surprisingly, in these cases and for many other specimens, the dominant crack did not initiate from a defect indicating that microstructural features are responsible for crack initiation. The dominating effects of microstructure rather than defects present in the material occurs despite the fact the defect sizes observed are typically much larger than the average microstructure size. Previous works have shown improved fatigue performance of AM titanium alloys after hot isostatic pressing (HIP) which resulted in defect sizes that were smaller than the grains [107-109]. For the present study, however, no HIP was performed and defects present in the material were much larger than the grain size, as indicated by the FCI at point 2 in *Figure 27*a.

Considering the fact that the majority of the fatigue life in HCF regime is spent in nucleating a crack, the observed differences in the 304LSS microstructural features in *Figure 24*,

such as Σ3-TB and HAGB, are most likely responsible for the improved HCF behaviour. Under strain-controlled conditions, the similar HCF behaviour between wrought and LB-PBF 304LSS can be explained by the deformation in the gage section being strictly controlled by the utilized control mode. Contrastingly, under force-controlled conditions, the deformation for the LB-PBF material with a higher cyclic yield strength would be expected to be less severe than the wrought counterpart. The lower cyclic deformation would directly translating translate to an improved fatigue resistance of the LB-PBF 304LSS as observed in *Figure 26*c.

The ex-situ CIS analysis was carried out to elicit the mechanisms responsible for the improved fatigue resistance of LB-PBF 304LSS. For the stress amplitude of 330 MPa, cracks from both the wrought and LB-PBF material are shown in Figure 28 on the left with their corresponding inverse pole figure (IPF) orientation overlays on the right. The crack for the wrought material (Fig. 4a) developed into a dominant crack approximately 310 μm long by 35,000 cycles, while the longest crack observed in the LB-PBF material (Fig. 4c) was still in the initiation stage at 76 μm long by 100,000 cycles. The overlays of the EBSD orientation data on the LB-PBF cracks in Figure 28 show the relationship between the crack and underlying microstructure. The crack in Figure 28c occurred at a HAGB approximately 51° and propagated along the boundary until it reached the LAGB, at which the crack propagation slowed down significantly. The crack shown in Figure 28b initiated at a Σ3-TB boundary which was surprising considering the lack of these boundaries within the microstructure of the LB-PBF 304LSS. Interestingly, the Σ3-TB is oriented approximately 45° from the loading direction similar to what was observed for the wrought material [15].

The microstructural CIS investigation revealed that the majority of cracks in the LB-PBF

material initiated at HAGB. After initiating, these cracks slowed considerably once they encountered LAGB with additional testing up to 300,000 cycles failing to result in a dominant crack. This observation is in contrast with the previous observations for the wrought material that FCI was dominated by Σ3-TB [15]. The solidification characteristics of LB-PBF process, and subsequently, the presence of <011> texture results in a high density of LAGB and minimal density of HAGB, as shown in *Figure 24*. The nature of FCI in 304LSS and the unique microstructure for LB-PBF 304LSS, lead to a reduction in Σ3-TB, which are more susceptible to early life FCI, shifting the dominant FCI mechanism of the LB-PBF 304LSS to HAGB. More importantly, the higher cyclic yield strength of LB-PBF 304LSS results in much less cyclic deformation, even at stress amplitudes approaching the quasi-static yield stress. This is noticeable in Figure 28, where the slip lines, that are easily distinguishable in Figure 28a for the wrought material, are mostly absent in Figure 28b-c for the LB-PBF material. This combination of finer microstructure and lower HAGB/Σ3-TB density results in the improved fatigue performance for LB-PBF 304LSS compared to its wrought counterpart.

4.5 Conclusions

These profound results show that while most AM materials are susceptible to early fatigue failures, austenitic SSs can be successfully fabricated via LB-PBF to offer superior strength, ductility, and more importantly fatigue resistance compared to their wrought counterparts. Taking advantage of the intimate relationships among the localized thermal input during the AM process and the resulting microstructure and mechanical properties, not only can the fatigue strength of these materials be improved, the microstructure can be tailored to meet specific service loading requirements to enhance the overall fatigue performance. Increasing or decreasing the supplied

energy density can lead to lower/higher cooling rates which in turn can lead to coarser/finer microstructures, respectively. This means that in areas more susceptible to FCI, such as holes/notches, the parameters can be adjusted to increase the cooling rate, resulting in finer microstructure and higher local strength and FCI resistance. Away from these areas of increased stress, the parameters can be further adjusted to give lower cooling rates and coarser microstructure, which can improve the crack growth resistance.

These findings for LB-PBF 304LSS offer early insight into how additive manufacturing can be used to fabricate superior fatigue resistant materials by further establishing the process-structure-property-performance relationships and taking advantage of the design-space offered by these techniques. It is important to note, however, that the internal porosity also is intimately related to the local thermal input and deviations outside of an optimal process window could result in defects dominating the fatigue behaviour despite the improved microstructure. More in-depth studies focusing on various process/post-process effects on the resulting microstructure, dislocation density, and deformation characteristics as well as the local behaviour at notches are needed to fully establish the process-structure-property relationships for LB-PBF 304LSS. This study indicates the true potential of additive manufacturing may be realized through the ability to fabricate net-shaped parts with microstructures tailored to meet specific performance requirements as dictated by the service loading conditions. This ability to tailor microstructure through additive manufacturing for an increased resistance to crack initiation and/or growth can expedite the adoption of this technology for fatigue critical applications across many industrial sectors to deliver lighter, stronger, and safer products.

Acknowledgements

Partial funding for this work was provided by the National Science Foundation under Grant No. 1657195.

Disclosure Statement

No potential conflict of interest was reported by the authors.

Table 6: Chemical composition by weight % of the LB-PBF (AM) powder feedstock and wrought (WR) material provided by manufacturer.

	C	*Cr*	*Cu*	*Mn*	*N*	*Ni*	*O*	*P*	*S*	*Si*
AM	0.017	18.40	<0.10	1.20	0.09	9.40	0.03	0.012	0.005	0.55
WR	0.029	18.06	0.45	1.35	0.07	8.59	NA	0.032	0.030	0.28

Table 7: Grain boundary lengths and fractions for both wrought and LB-PBF 304LSS.

		5° - 15° (LAGB)	*15° - 45°*	*45° - 54° (HAGB)*	*Σ3-TB ±8.66*
LB-PBF	Length (mm)	43.8	33.5	14.4	1.51093
	Fraction	0.144	0.11	0.047	0.005
Wrought	Length (mm)	1.31	7.74	4.08	9.95063
	Fraction	0.014	0.082	0.043	0.105

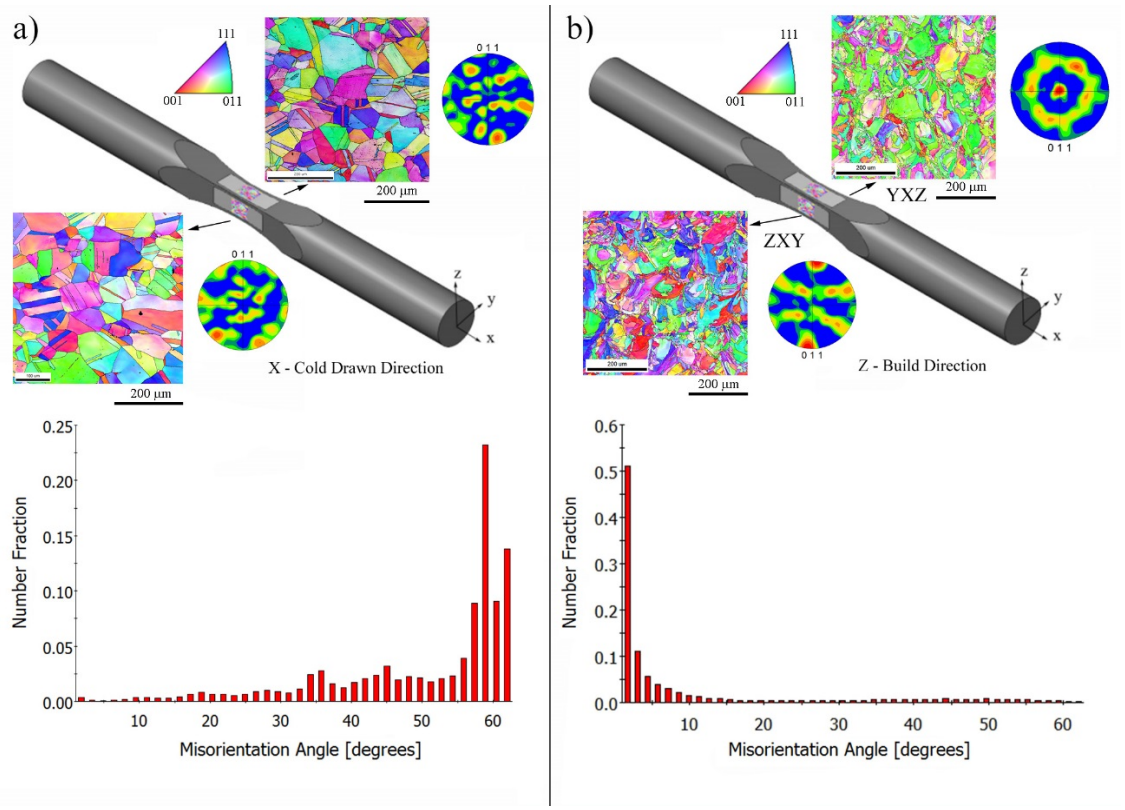

Figure 24: Microstructure; analysis for a) cold drawn and annealed wrought 304LSS and b) LB-PBF 304LSS for each face in relation to the drawing or build directions respectively.

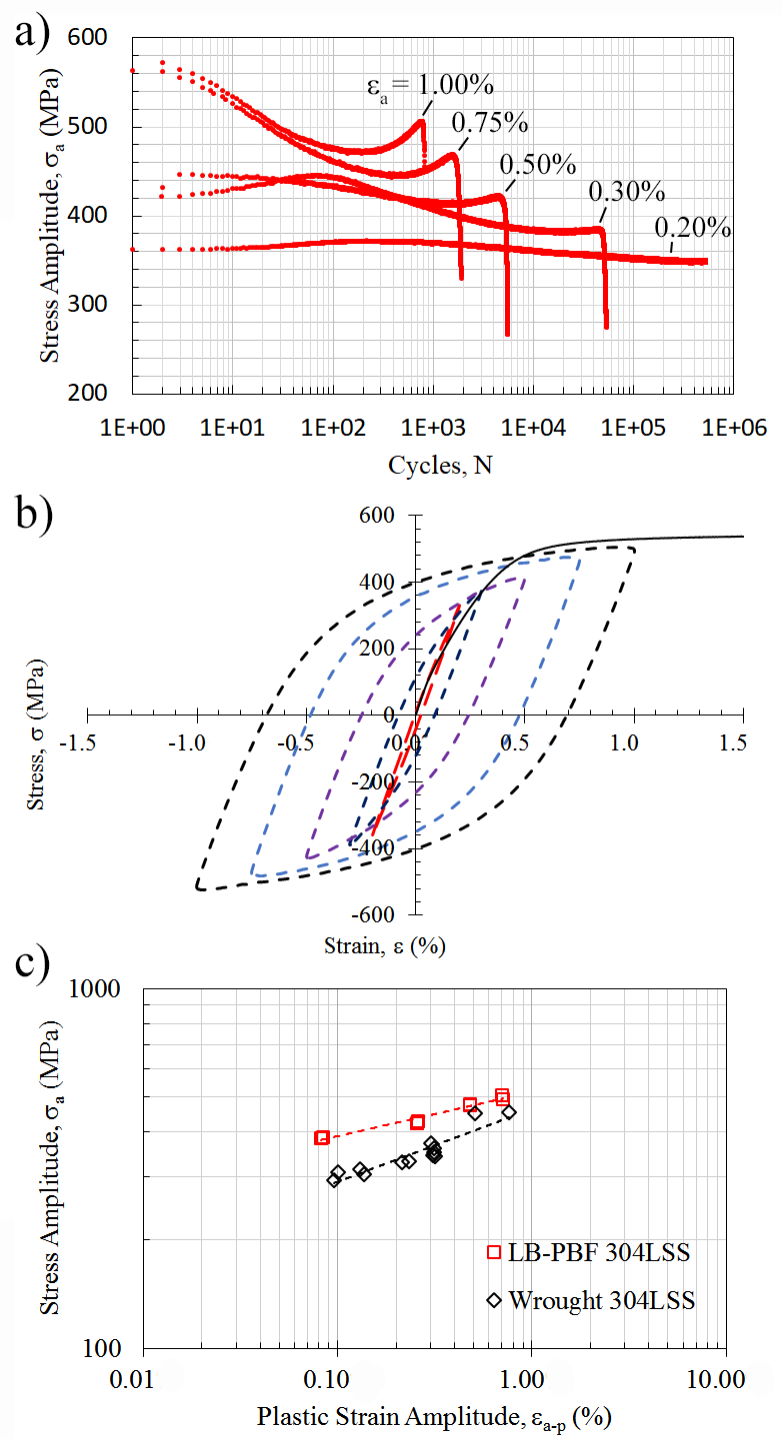

Figure 25: Cyclic deformation behavior of LB-PBF showing a) stress response under strain-controlled conditions, b) cyclic stress-strain hysteresis loops for 1.0%, 0.75%, 0.5%, 0.3%, and 0.2% strain amplitudes, and c) strain hardening behavior in comparison with wrought material.

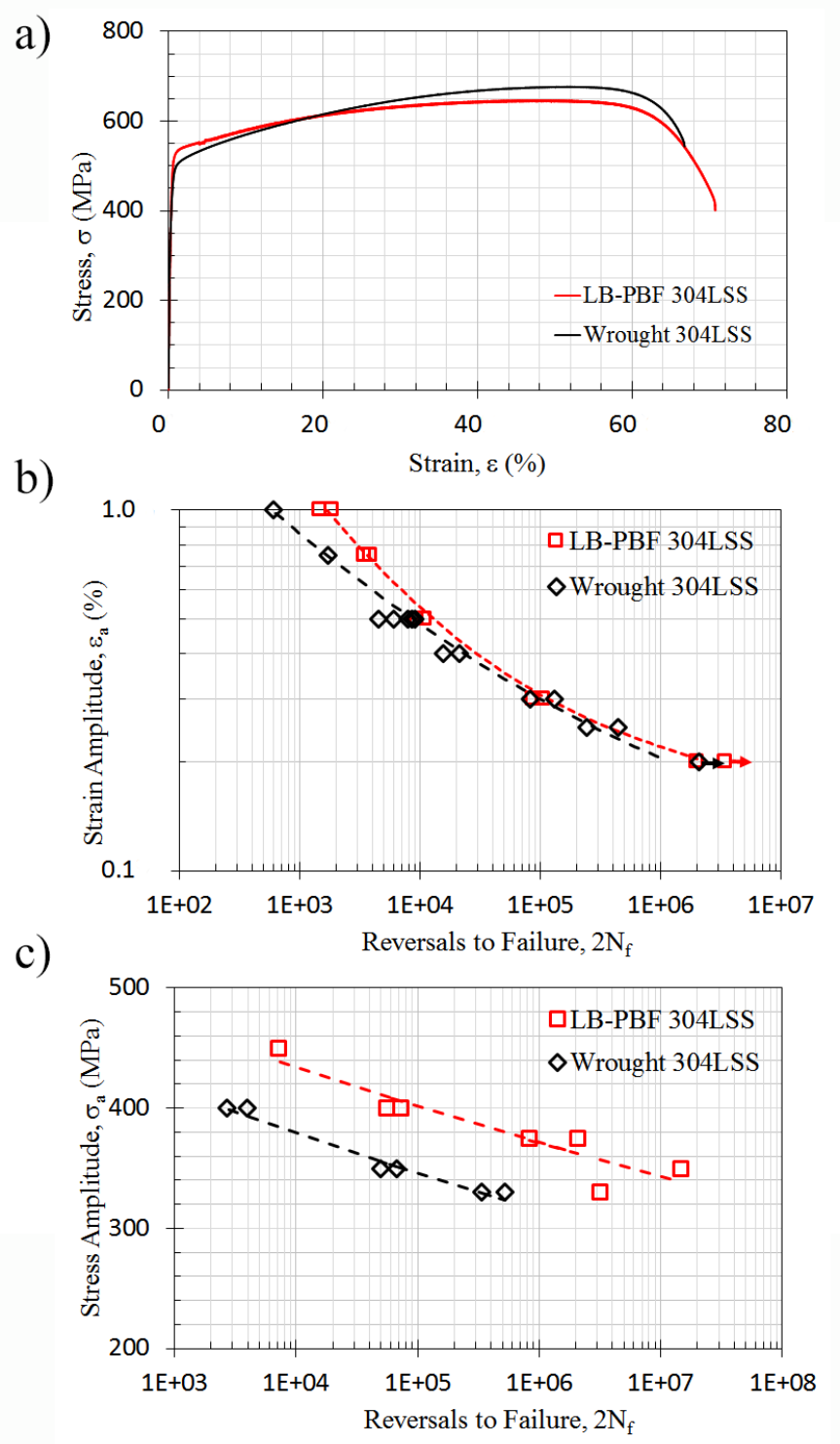

Figure 26: Comparison of LB-PBF and wrought 304LSS mechanical behavior: a) quasi-static tensile behavior, b) strain-life fatigue behavior, and c) stress-life fatigue behavior for both wrought and LB-PBF 304LSS.

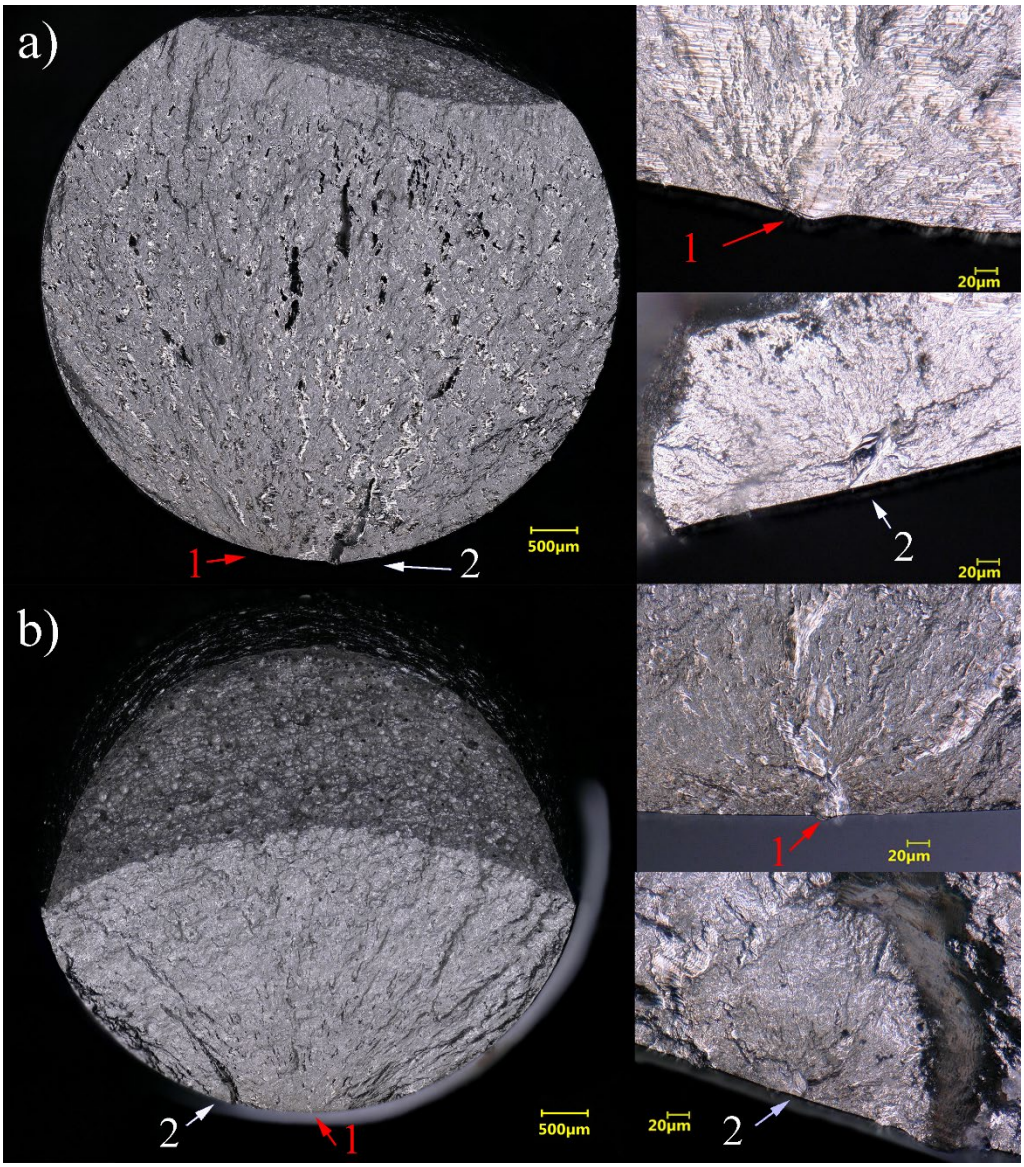

Figure 27: Fracture surfaces of (a) strain control test at εa = 0.3% and (b) force control test at σa = 400 MPa.

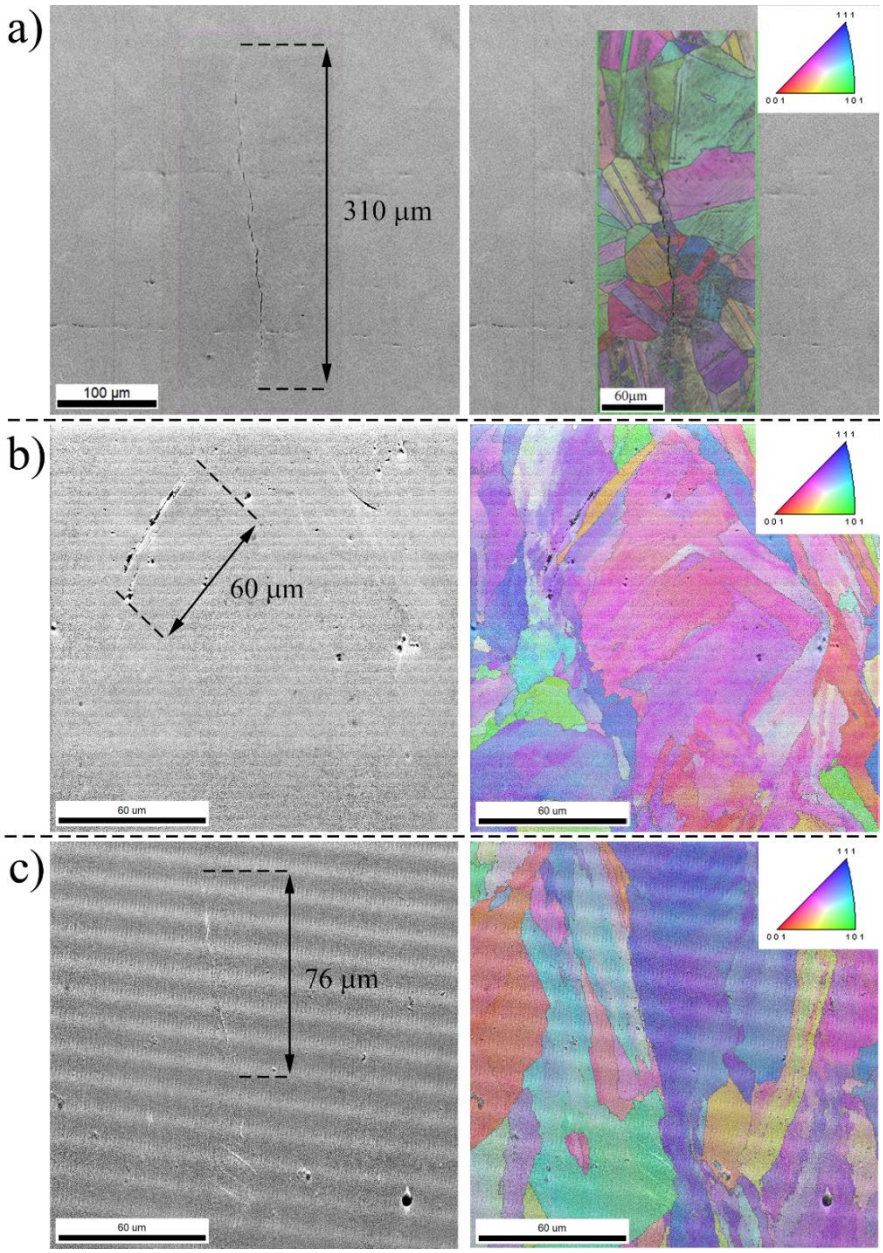

Figure 28: (a) SEM image of a dominant crack in the wrought material with the grain structure overlay, (b) SEM image of a Σ3-TB boundary crack in LB-PBF material with the grain structure overlay, and (c) SEM image of a HAGB crack in LB-PBF material with the grain structure overlay.

Chapter 5: The effects of post-process thermal treatments on the static and cyclic deformation behavior of LB-PBF austenitic stainless steel

The following chapter was partly peer reviewed and accepted for publication in the Solid Freeform Fabrication conference proceedings as well as being recognized as an outstanding paper and selected for publication in JOM. The current version has been submitted and under peer review with the journal.

Heat treatment effects on the crack initiation behavior and fatigue resistance of an additive manufactured austenitic stainless steel

Authors: Jonathan W Pegues, Michael D Roach, Nima Shamsaei

Publication date: NA

Journal: JOM

Volume: NA

Pages: NA

Publisher: TMS, Springer

Heat treatment effects on the crack initiation behavior and fatigue resistance of an additive manufactured austenitic stainless steel

Jonathan W. Pegues [a,b] Michael D. Roach[c] and Nima Shamsaei [a,b]

[a] *Department of Mechanical Engineering, Auburn University, Auburn, AL 36849, USA*

[b] *National Center for Additive Manufacturing Excellence (NCAME), Auburn University, Auburn, AL 36849, USA*

[c] *Department of Biomedical Materials Science, University of Mississippi Medical Center, Jackson, MS 39216, USA*

Tel: 334-844-4839

Email: shamsaei@auburn.edu

Abstract

As additive manufacturing marches towards use in structural applications which can also include fatigue critical parts, the interrelations between the process-structure-property need to be fully characterized. Currently, most additive manufactured components go through extensive post-processing including heat treatment to improve the microstructure and resulting fatigue performance. In this study the effect of stress relief and solution annealing on the tensile and fatigue performance including force and strain-controlled conditions is investigated. Results show that while the strain-life fatigue behavior is not significantly affected by heat treatment, the stress relieved specimens show remarkable enhanced stress-life fatigue resistance. Microstructural analysis suggests the as-fabricated microstructure is beneficial to crack initiation resistance, shielding processed-induced defects from crack initiation. After solution annealing, however, the crack initiation mechanism shifts from nucleating at twin and high angle grain boundaries to defects such as lack of fusion and gas entrapped pores, negatively affecting the fatigue resistance.

Keywords: Laser beam-powder bed fusion; Crack initiation; Microstructure; Twin boundary; Cyclic deformation

5.1 Introduction

Additive manufacturing of parts for end use in fatigue critical applications is currently limited by the presence of processed-induced defects which act as early life crack initiation sites [4, 84, 105, 110]. These defects are particularly detrimental in the high cycle fatigue (HCF) regime where the majority of the fatigue life is spent nucleating a fatigue crack. To date, much of the research has focused on better understanding the role of processed-induced defects on the fatigue resistance of many alloy systems common to additive manufacturing [87, 111-113]. To overcome the detrimental effects of these defects in additive manufactured (AM) materials, researchers have used heat treatments optimized towards additively manufactured materials to improve the as-fabricated microstructure or hot isostatic pressing (HIP) to reduce the defect size to varying degrees of success [114-117].

For additive manufactured (AM) austenitic stainless steels, there have been several studies that report fatigue properties similar to what is observed for their wrought counterparts, while others report lower fatigue performance. Riemer et al. [118] showed that laser beam powder bed fused (LB-PBF) 316L stainless steel (316LSS) could produce fatigue limits comparable to its traditionally processed counterpart without the need for post-process heat treatments. Leuders et al. [119] showed that HIPing 316LSS reduced the ultimate tensile stress (UTS) and the low cycle fatigue (LCF) strength while only producing limited improvements in the HCF regime. Shrestha et al [26] reported lower fatigue strengths as compared to the wrought counterpart which were linked to the presence of large lack-of-fusion (LoF) type defects, as also reported by Liverani et al. [120].

These contrasting results suggest a competition between microstructure and processed-induced defects that can be particularly evident after post-process heat treatments. A previous work

on wrought austenitic stainless steels has revealed that annealing twin boundaries (Σ3-TB) and high angle grain boundaries (HAGB) are susceptible to crack initiation in the intermediate to HCF regime [14-16, 60, 76]. Pegues et al. [121] showed that LB-PBF 304L stainless steel (304LSS) in the stress relieved condition produced improved fatigue resistance compared to its wrought counterpart in both the LCF and HCF regime. This improved fatigue performance was related to the microstructure evolution and reduced Σ3-TB and HAGB densities relative to traditional wrought materials. Due to the susceptibility of grain boundary sensitization at elevated working temperatures, austenitic stainless steels are typically supplied in the cold worked and solution annealed condition. For LB-PBF processes, however, austenitic stainless steels can be fabricated in the desired shape without the need for cold working and subsequent solution annealing.

The present work aims to better understand the process-structure-property (PSP) relationships of an LB-PBF 304LSS alloy targeting the effect of post-process heat treatment on the fatigue resistance. These cause and effect relationships between the microstructure and mechanical performance are critical to understanding how additive manufacturing can be leveraged to fabricate parts with improved mechanical performance and reliability for the use in load-bearing, safety-critical applications.

5.2 Experimental Methods

Square rod specimens were fabricated using an EOS M290 and the parameters outlined in *Table 8*. Two separate builds were fabricated with the first one containing horizontal specimen blanks and the other containing vertical specimen blanks. Due to the high aspect ratio of the specimen blanks (length-to-width), the process parameters for the vertical specimens were adjusted to include a lower scan speed and were fabricated using the carbon fiber rake to prevent build failure. The specimen blanks were machined down to cylindrical uniform gage fatigue (UGF)

specimens following ASTM E606 [52]. Additionally, four horizontal specimens were machined down to non-standard square gage fatigue (SGF) specimens as described elsewhere [17] in order to track fatigue crack initiation (FCI), including nucleation and microstructurally small crack growth. *Figure 29* depicts the orientation of the specimen blanks and fatigue test specimen types taken from the blanks. In this image, the z-axis is parallel with the build direction while the x-axis is parallel to the rake direction and the y-axis is parallel to the gas flow direction.

The UGF specimen geometry was used for quasi-static tensile tests, strain controlled fatigue tests, and force controlled fatigue tests. Under force controlled fatigue testing, the E606 [52] geometry deviates from the suggested E466 [122] shoulder radius for force controlled fatigue testing, however, the extreme ductility of 304LSS results in less sensitivity to this dimension, as pointed out in E466 [122].

The UGF specimens were separated into three groups; horizontal stress relieved (H-SR), vertical stress relieved (V-SR), and vertical solution annealed (V-SA). The H-SR and V-SR were stress relieved at 400°C for 1 hour and furnace cooled and the V-SA specimens were solution annealed at 1040°C for 1 hour followed by water quenching. All heat treatments were performed after machining to the final dimensions followed by removal of the outer surface by hand grinding and polishing in the longitudinal direction of the specimens. The final polishing step resulted in near-mirror surface finishes with mean surface roughness (R_a) less than 1 μm.

The horizontally built SGF specimens were either stress relieved (H-SR) or solution annealed (H-SA) following the procedures outlined for the UGF specimens. These specimens were also hand ground and polished in the longitudinal direction followed by an electropolish using Struers A2 procedure/recipe. This extra polishing step was performed to create a pristine surface

to obtain electron backscatter diffraction (EBSD) maps and monitor the microstructural effects on fatigue crack initiation.

All mechanical testing was performed on an MTS servo-hydraulic load frame with a 100 kN capacity. Strain controlled quasi-static tensile tests were performed at a strain rate of 0.001 s-1 up to 4.5% strain, after which, the extensometer was removed and the test was continued in displacement control at a displacement rate of 0.0125 mm/s until failure. Before testing, the extensometer knife edges were inscribed on the specimens to measure elongation after break for each specimen. The strain after removal of the extensometer was estimated by the incremental changes in displacement according to the linear-variable displacement transducer (LVDT). The stain estimation from the LVDT was used to determine the shape of the resulting stress-strain curve after removal of the extensometer at 4.5% up to elongation after break measured from the inscribed gage marks.

Fatigue tests were conducted either under force or stain controlled conditions. Frequencies were adjusted to give similar average cyclic force/strain rates for all stress/strain levels. Strain controlled tests were conducted up until an approximate 40% drop in peak force beginning after 1,000 fatigue cycles. The specimens were then mechanically separated after the extensometer was removed. Force controlled fatigue tests were conducted with the extensometer attached until the estimated half-life of the specimen. After removal of the extensometer, the tests were continued to final rupture.

5.3 Microstructure

The as-built microstructure of the LB-PBF consists of columnar type grains that extend along the build direction as depicted in the microstructure cube in *Figure 30* (not to scale). The number fraction of the grain boundaries for the plane perpendicular (XY-Plane) and parallel (XZ-

Plane) to the build direction are given in the histograms in *Figure 30*, noting a similar morphology in XZ-Plane and YZ-plane. The grain boundary characterization charts show a high density of low angle grain boundaries (LAGB) and low density of high angle grain boundaries (HAGB). Interestingly, the density of the Σ3-TB is very low for LB-PBF 304LSS which is in stark contrast to what is typically observed for the wrought material [15].

The effect of heat treatment on the average grain size in both the planes perpendicular (⊥) and parallel (//) to the build direction is given in *Table 9* and shows slight increases in grain sizes for the SA condition. These slight changes in grain size are expected for a solution anneal at the soak temperature of 1040°C which is well below the recrystallization temperature and at the low end of the grain growth regime. Interestingly, despite the columnar grain structure, the planes parallel to the build direction were not measured to be significantly larger than the grains perpendicular to the build direction. This is most likely due the high density of the LAGB such that the average grain size for the parallel faces approaches a similar value as the perpendicular faces.

The Kernel Average Orientation (KAM) maps for a horizontally fabricated stress relieved (H-SR) specimen and a horizontally fabricated solution annealed (H-SA) specimen, both perpendicular to the build direction, are shown in *Figure 31*. The KAM map compares the orientation of each kernel in the grain to the kernel at the center of the grain, and thus, gives an indication of the strain gradients and sub-grain structures within the grains [123]. The sub-grain boundaries can be observed as thin green lines and related to sudden very slight changes in misorientation associated with these types of boundaries. More gradual changes in misorientation are indicative of strain gradients present in the grain requiring geometrically necessary dislocations (GND) to accommodate the lattice strain within the grain. Both sub-grain boundaries and GNDs

can restrict the movement of statistically stored dislocations (SSD) and affect the mechanical performance and crack nucleation of a material.

The charts on the left side of *Figure 31* show the distribution of these misorientations with higher values of KAM indicating more variation with the grains which is also observed in the color maps to the right. The decrease in the KAM for the H-SA condition indicates that significant growth of the sub-grain boundaries has occurred along with a reduction in the strain gradient and ultimately the GND structure during the applied SA treatment. The reduction in strain gradients and sub-grain boundaries can be observed in the KAM maps where many of the grains are showing larger areas of blue indicating much lower variation within those grains. These observations along with the measured grain sizes reported in *Table 9*, suggest that the slight change in grain size for the H-SA condition can be attributed to the growth of the LAGB and sub-grain boundaries which would be expected to have higher velocities compared to HAGB [124].

5.4 Deformation Behavior

5.4.1 Quasi-static Tensile

The stress-strain behavior for all additive AM conditions compared to the wrought condition is shown in Figure 32. In the wrought condition, the constitutive stress-strain relationship is characterized by remarkable toughness as indicated by moderate yield strength followed by significant strain hardening leading to high ultimate tensile strength (UTS) and exceptional uniform elongation, strain up to necking. The AM SR condition shows similar tensile behavior to the wrought material with the yield stress and elongation to failure being slightly higher and the strain hardening rate and UTS being slightly lower. Surprisingly, the AM SA condition exhibits much lower yield strength, and UTS as well as much higher elongation to failure than the other

conditions. The toughness of the AM 304LSS material is expected to reduce the sensitivity to processed-induced defects and responsible for the improved fatigue performance reported elsewhere [121].

5.4.2 Cyclic Deformation Behavior

The strain-life (ε-N) and stress-life (σ-N) fatigue results of the UGF specimens for all conditions are given in *Figure 33*. The strain-life fatigue behavior is very similar for all conditions with the exception of the LCF regime, where the LB-PBF material in both SR and SA conditions exhibited slightly better fatigue performance as compared to the wrought counterpart. In the HCF regime, which is typically dominated by the presence of defects, both of the AM conditions showed fatigue lives in the range of what was observed for the wrought material. It should be noted, however, that at $\varepsilon_a = 0.2\%$, the SA-V test failed before 10^6 cycles ($2N_f = 2x10^6$ reversals), while the other conditions were suspended after exceeding 10^6 cycles as runout tests. These results suggest that despite the presence of porosity in the additive manufactured materials, the AM 304LSS microstructure is playing a significant role in delaying the crack initiation behavior [121].

The stress-life behavior, on the other hand, shows improved fatigue resistance for the both the AM H-SR and V-SR conditions and lower fatigue resistance for the AM V-SA condition compared to the wrought material. The AM H-SR and V-SR conditions had runouts at stress amplitudes up to 375 MPa, while at the same stress amplitude the AM SA condition only obtained approximately 2,000 cycles. This reduction in σ-N behavior is interesting considering the small changes in microstructure that was observed for the H-SA condition, suggesting a change in failure mechanism may be responsible for this discrepancy in performance.

The cyclic stress-strain behavior of 304LSS is complex showing various stages of deformation behavior, as shown in the stress amplitude versus number of cycles plots at the top of *Figure 34*. Under the strain controlled condition, there are three general stages of deformation associated with 304LSS for both the wrought and AM materials; initial work hardening, cyclic softening, and secondary hardening [10, 15]. While all the different conditions show similar trends in these deformation stages, the stress H-SR condition requires greater stress to reach the desired constant strain amplitude than both the wrought and SA conditions.

The hysteresis loops at the end of the cyclic softening stage, presented in the lower portion of *Figure 34*, show that for both HCF and LCF conditions, the AM H-SR has less plastic deformation occurring for each cycle despite its higher stress response. Accordingly, the cyclic yield strength of the AM H-SR condition (σ_y' = 424 MPa) is higher than the ones for the wrought (σ_y' = 334 MPa) and AM V-SA (σ_y' = 347 MPa) conditions. The higher cyclic yield strength and less cyclic plastic deformation for AM H-SR is related to the finer sub-grains and GND structure as indicated by the higher KAM values discussed previously. Interestingly, the V-SA exhibits similar cyclic yield strength to the wrought material despite having much finer grain sizes, suggesting that the sub-grains and dislocation structure are more influential to the cyclic yield strength than the grain size. Interestingly, regardless of differences in stress response and plastic deformation, all conditions have similar cycles to failure (i.e. fatigue lives).

5.5 Crack Initiation

5.5.1 Fractography

The fracture surfaces of the LB-PBF materials also revealed some interesting behavior

between the various heat treated conditions types. Interestingly, while some cracks were found to initiate at LoF or gas entrapped pores, a number of others initiated at the surface without the presence of typical additive manufacturing defects. Figure 35 compares several fracture surfaces from force controlled fatigue tests for each AM condition. The main observation from these fracture surfaces is the tendency for a dominant crack to initiate at the surface, propagate approximately 60 – 70% through the cross-sectional area before final rupture. The final fracture of the material occurs in the ductile tearing mode leaving behind a clear crack propagation path and significant plastic deformation shear lip at the final fracture location.

Another interesting observation that can be made from Figure 35 is that for the AM V-SA condition; there are several secondary cracks that can be observed on the fracture surface. Upon closer inspection, these secondary cracks were found to occur mostly at small defects and coalesce with the dominant crack as it propagated through the cross-section. Interestingly, tests subjected to strain-controlled cycling showed extensive secondary cracking on the fracture surfaces while tests subjected to force-controlled cycling had fewer secondary cracks. While some AM SR specimens showed some secondary cracking on the fracture surfaces, the prevalence was much lower than what was observed for AM SA specimens.

A higher propensity of crack initiation at processed-induced defects was observed in strain controlled tests as compared to the force controlled tests. Despite cracks initiating at large defects such as LoF or gas entrapped pores near the surface, the fatigue life was ultimately not affected to the extent observed for other additively manufactured materials. Interestingly, regardless of the crack initiating at defects or microstructure under strain controlled conditions, the fatigue life is not adversely or beneficially affects. This observation suggests that other mechanisms such as

crack growth or deformation may be influencing the ε-N fatigue behavior minimizing the effect of initiation feature type.

5.5.2 Secondary Cracks

To better understand the crack initiation behavior of the AM UGF specimens in the SR and SA conditions, the gage sections of several tested specimens were removed and sectioned longitudinally to collect EBSD maps of the cracked or uncracked defects. The comparison between conditions that promote crack initiation at defects and conditions that promote crack initiation at microstructural features is essential in understanding the effects of heat treatment. *Figure 36* gives a representation of secondary cracks observed for the AM V-SA conditions, for which the loading direction is horizontal with respect to the image. Both cracks show deformation induced martensitic transformation (DIMT) occurring around them as indicated by the green α'-BCC phase. It is unclear whether the DIMT occurs as a prerequisite for crack initiation or develops due to the presence of the crack and the corresponding plastic zone at the crack tip. The kernel average misorientation (KAM) is also given for each crack at the bottom of *Figure 36* showing relatively low KAM values in the austenite (γ-FCC) structure. It is interesting to note that in the DIMT (α'-BCC) zones, the KAM values are observably higher, which would be expected due to the increase in volume during the diffusionless FCC → BCC transformation.

Similar analysis was performed on defects present in the AM H-SR condition and is shown in *Figure 37*. In these cases, however, secondary cracks have not developed from these defects despite their similar size and sharp features. For the AM H-SR specimens under strain control at $\varepsilon_a = 1.0\%$ in Fig. 9a, DIMT is present throughout the microstructure as well as at the defect itself. This contrasts with the AM H-SR condition under force control loading at $\sigma_a = 400$ MPa in *Figure*

*37*b, where there is little to no DIMT present. Comparing the KAM results to the AM V-SA specimens in *Figure 36*, there appears to be a substantial number of sub-grains and strain gradients throughout the microstructure and surrounding the defects in the AM H-SR specimens. The presence of these sub-grain boundaries and the associated GNDs from the strain gradients would be expected to limit the motion of SSDs. It can thus be concluded that this microstructure morphology is beneficial to limit crack initiation at processed-induced defects.

5.5.3 Ex-Situ Crack Initiation

Force-controlled fatigue tests were conducted on both AM H-SR and H-SA SGF specimens at a stress amplitude of σ_a = 330 MPa which produced runouts past 10^6 cycles for AM H-SR and V-SA UGF tests (no H-SA UGF tests were conducted). While one of the AM V-SA specimens reached 10^6 cycles at σ_a = 330 MPa, the other two tests at this stress level failed before reaching 10^5 cycles. This type of scatter is typical for materials in which defects play a significant role in crack initiation and suggest that crack initiation at defects may be the leading cause of the lower fatigue resistance for the AM V-SA specimens.

Figure 38 compares typical cracks that initiated in both AM H-SR and H-SA specimens along with the corresponding phase and KAM maps, loading direction is horizontal to image. The H-SR specimen had cracks initiating from HAGB and Σ3-TB such as the one in Fig. 10a. The KAM shows a lower average value compared to what was observed for the post-mortem defect analysis for the SR condition discussed in *Figure 37*, which is most likely the result of fewer grains being analysed in *Figure 38*. This Σ3-TB crack was first observed at 100,000 cycles with a length of approximately 60 μm and, after an additional 200,000 cycles, the crack was still in the range of

60 μm, as seen in *Figure 38*a. Despite the large number of additional applied cycles, the crack has not propagated outside of the initiating grain and is apparently pinned by the adjacent grain boundaries. Similar observations of crack initiation at Σ3-TB/HAGB with little to no crack propagation after being subjected to additional fatigue cycles were made for other fatigue cracks in the H-SR SGF specimens

In contrast to the AM H-SR SGF specimens, the AM H-SA SGF specimens had numerous cracks initiating from defects such as the example in *Figure 38*b, agreeing with the observations made for V-SA secondary cracks in *Figure 36*. Similar to the V-SA UGF specimens discussed previously, the H-SA SGF specimens have fewer sub-grain boundaries and less variation throughout the grains as evident by the KAM maps in *Figure 38*. Additionally, at 82,000 cycles the crack has propagated most of the way through four additional grains rather than being pinned within the initiating grain, as observed for the H-SR condition. While the crack in this H-SA SGF specimen is still relatively small (21.3 μm) as compared to the crack in H-SR SGF specimen observed at 300,000 cycles, the it has developed a plastic zone ahead of the crack tip as evident by the diagonal shear deformation lines and the DIMT surrounding much of the crack.

5.6 Summary and Conclusions

The increased prevalence of crack initiation at pores and the lower KAM values for the SA specimens suggest that the reduction of the fine sub-grain structure and strain gradients essentially increases the susceptibility of crack initiation at pores. During annealing, these low angle grain boundaries grow much more rapidly than the HAGB such that, on the larger scale, the grain size does not change significantly. However, the results presented in this study suggest that the underlying sub-grain structure is more influential on the fatigue strength of AM 304LSS which are

affected by high temperature solution annealing. While wrought 304LSS has been shown to be highly sensitive to crack initiation at HAGB/Σ3-TB microstructural features, the resulting microstructure of LB-PBF 304LSS has much fewer of these features as evident by the very low density of grain boundaries above 45° in *Figure 30*.

The shift in crack initiation from microstructure to process induced defects was found to detrimentally affect the stress-life fatigue behavior but surprisingly has little to no effect on the strain-life fatigue behavior. This observation suggests that there are competing mechanisms under strain-controlled conditions which minimize the effect of crack initiation at defects and result in similar fatigue performance for all conditions. One such explanation for the similar fatigue lives despite the differences in crack initiation mechanisms might be the crack growth behavior, which could also be influenced by the slight differences in microstructure. The crack growth effects may not be as apparent in the force controlled tests due to the destabilizing nature of the crack as it grows in size and the cyclic deformation which becomes unbounded. Under strain controlled conditions, however, the deformation is strictly limited during each cycle, thus, the crack remains stable throughout the fatigue life and less sensitive to crack initiation. While these observations are supported by the fatigue and cyclic deformation results, more rigorous studies are needed to explicitly explain the observed differences between force and strain controlled fatigue behavior.

The goal of this study was to determine the effects of post-process solution annealing on the mechanical properties of LB-PBF 304LSS. The understanding of these process-structure-property relationships are critical to implementing additive manufactured parts in fatigue critical applications. The following conclusions can be drawn from these results:

1) LB-PBF 304LSS in the stress relieved condition, remarkably, shows improved fatigue resistance compared to the wrought material in both the horizontally and vertically fabricated directions.
2) Solution annealing has a detrimental effect on the σ-N fatigue resistance of LB-PBF 304LSS leading to lower fatigue resistance compared to both the stress relieved conditions and wrought counterpart.
3) The strain-life fatigue behavior of LB-PBF 304LSS is comparable to the wrought counterpart in all tested conditions despite the presence of defects and different cyclic deformation behavior. This suggest that competing mechanisms are contributing to the fatigue resistance such that the effect of crack initiation type is minimized.
4) A shift in the crack initiation mechanism from microstructure to defects is responsible for the decreased σ-N fatigue resistance of the solution annealed LB-PBF 304LSS. Microstructure analysis revealed that a reduction in sub-grains and strain gradients within the grain structure decreases the cyclic yield strength and increases the deformation that occurs near the process-induced defects and increased risk for crack initiation.

Table 8: Process parameters used for the different part orientations.

Direction	Laser Power	Scan Speed	Hatch	Layer	Rake Type
Horizontal	195 W	1083 mm/s	0.09 mm	20 μm	Ceramic
Vertical	195 W	975 mm/s	0.09 mm	20 μm	Carbon Fiber

Table 9: Average grain diameters and corresponding standard deviation for each condition.

	Grain Size (mm)	Stand. Dev. (mm)
H-SR (⊥)	11.06	7.95
H-SA (⊥)	13.63	10.37
H-SR (//)	13.77	10.92
H-SA (//)	14.26	11.55

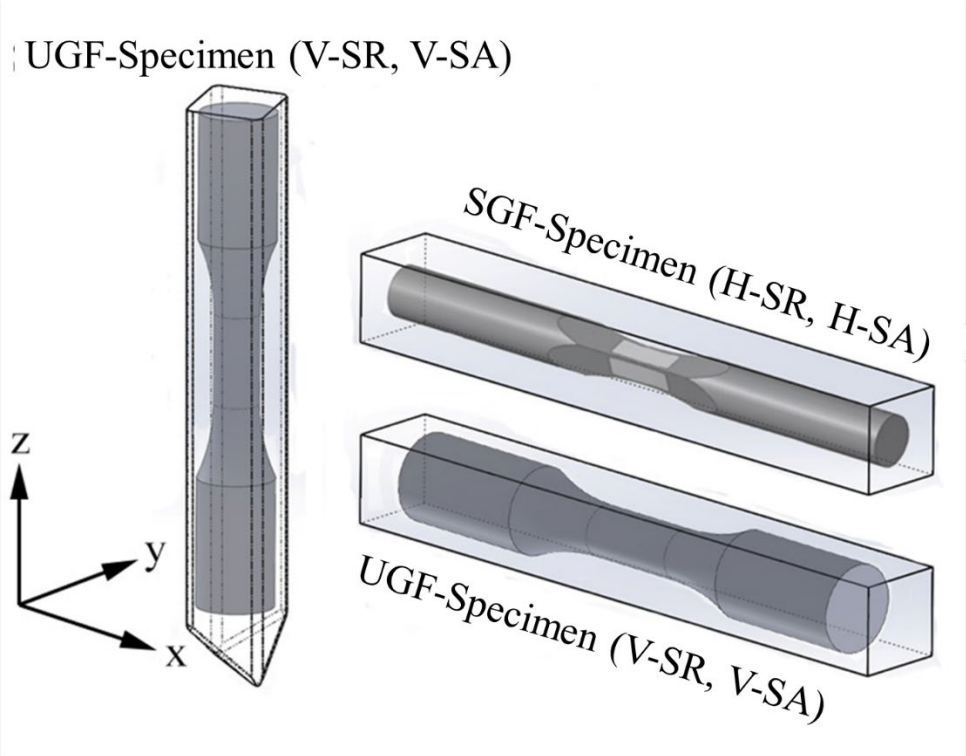

Figure 29: Orientation of the machining blanks and specimen types to be machined with V/H indicating the vertical or horizontal direction and SR/SA indicating stress relief or solution anneal.

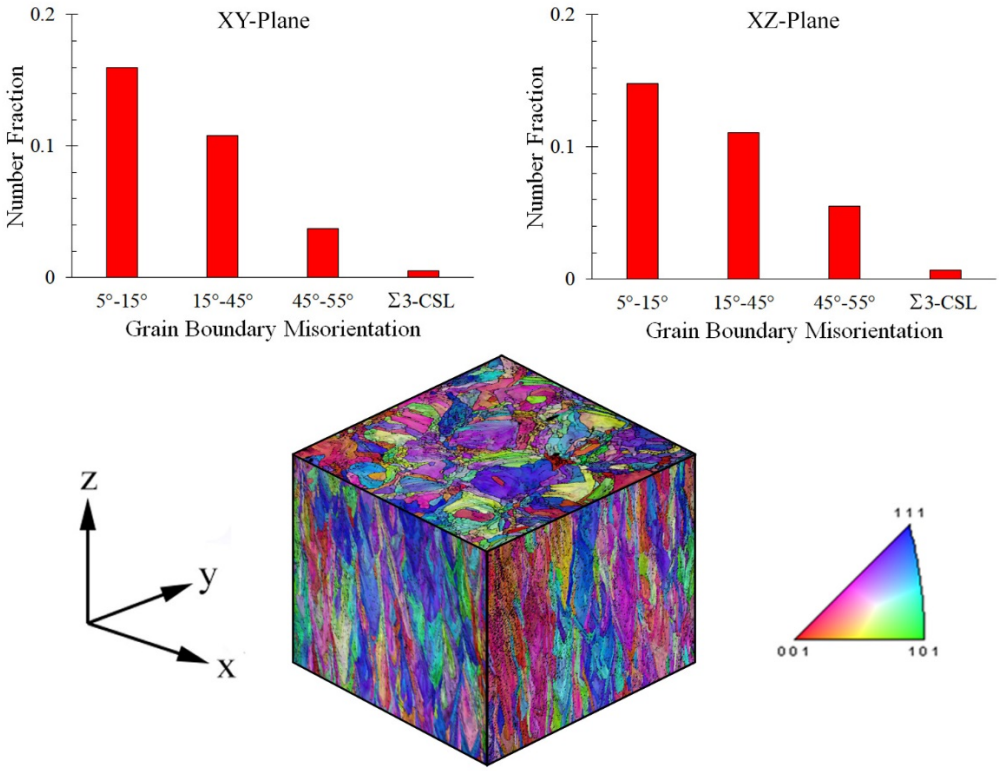

Figure 30: Representation of the stress relieved and solution annealed microstructure and corresponding grain boundary densities.

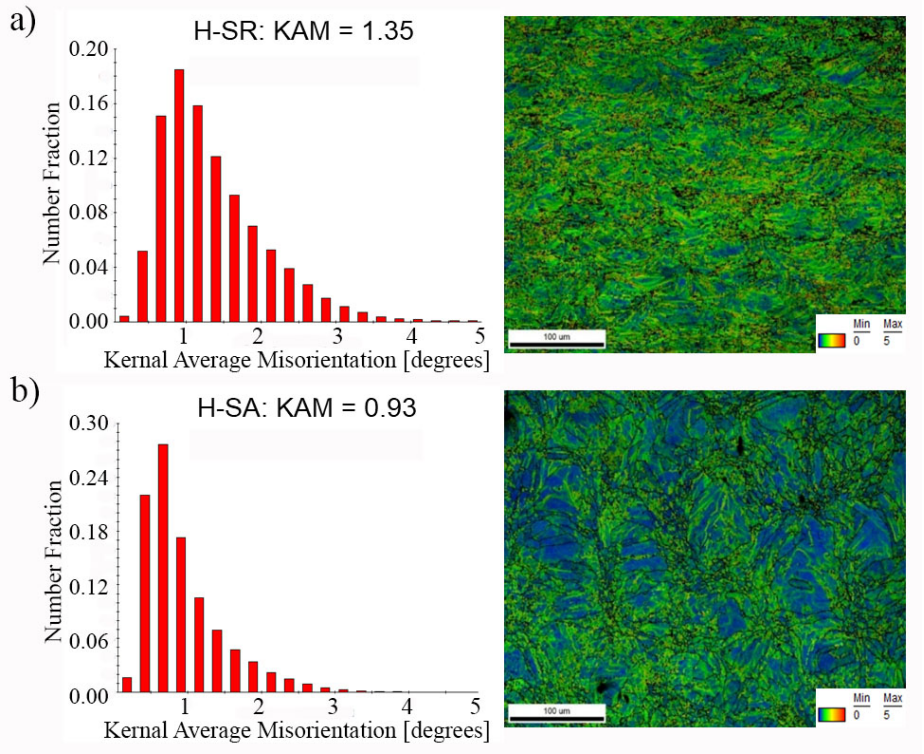

Figure 31: Kernel average misorientation maps for the surface perpendicular to the build direction of the stress relieved (SR-H) and solution annealed (SA-H) horizontally fabricated specimens.

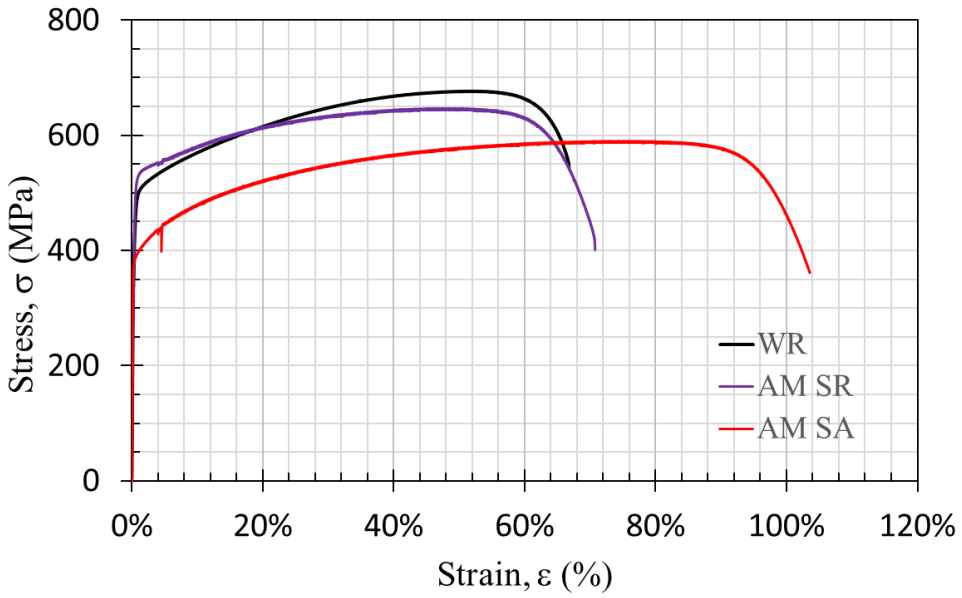

Figure 32: Quasi-static tensile behavior for wrought (WR), additive manufactured (AM) stress relieved (SR), and AM solution annealed (SA) conditions.

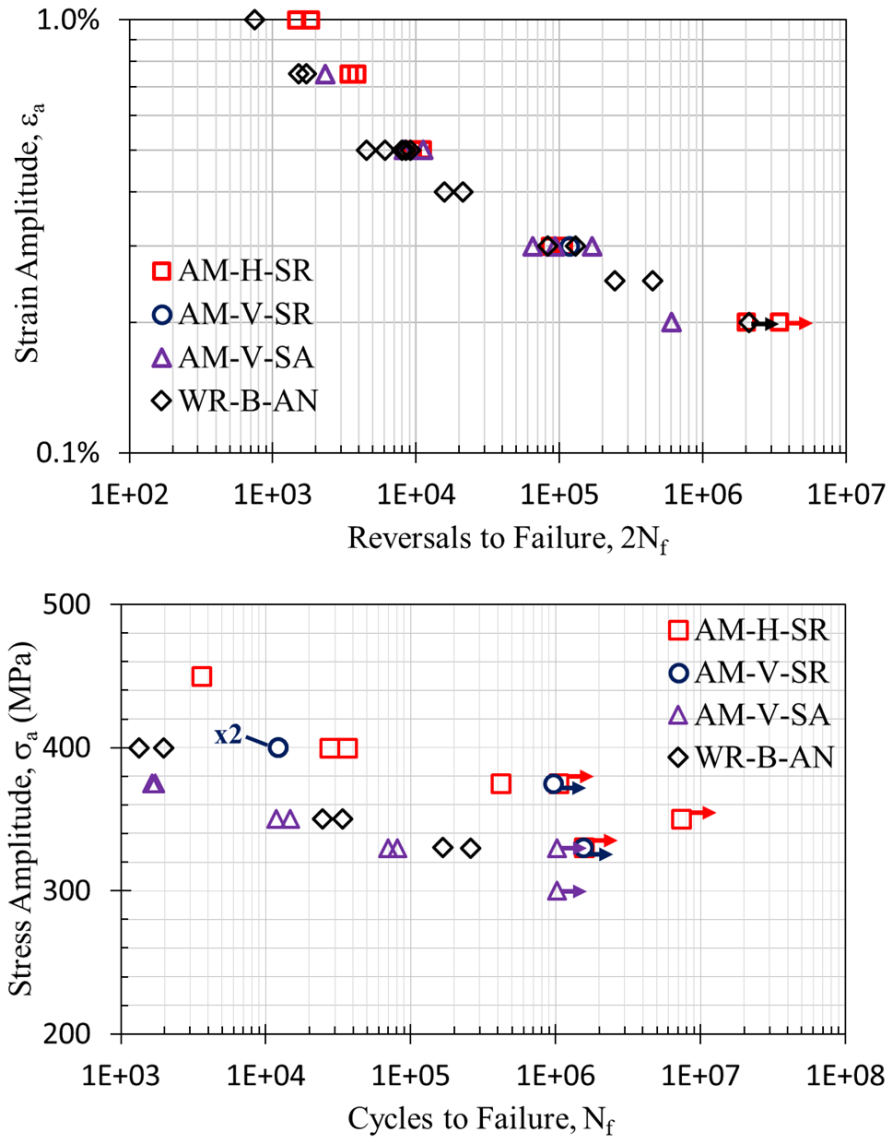

Figure 33: Strain-life and stress-life fatigue data for each condition.

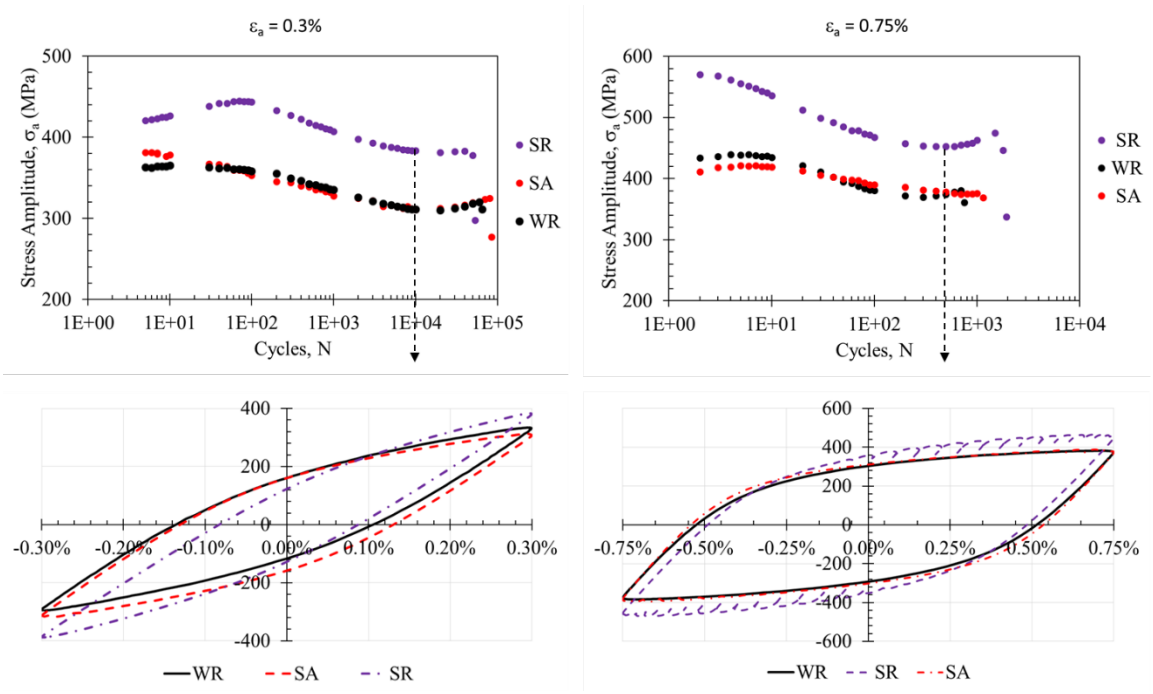

Figure 34: Deformation behavior for strain controlled tests at $\varepsilon_a = 0.35\%$ and $\varepsilon_a = 0.75\%$.

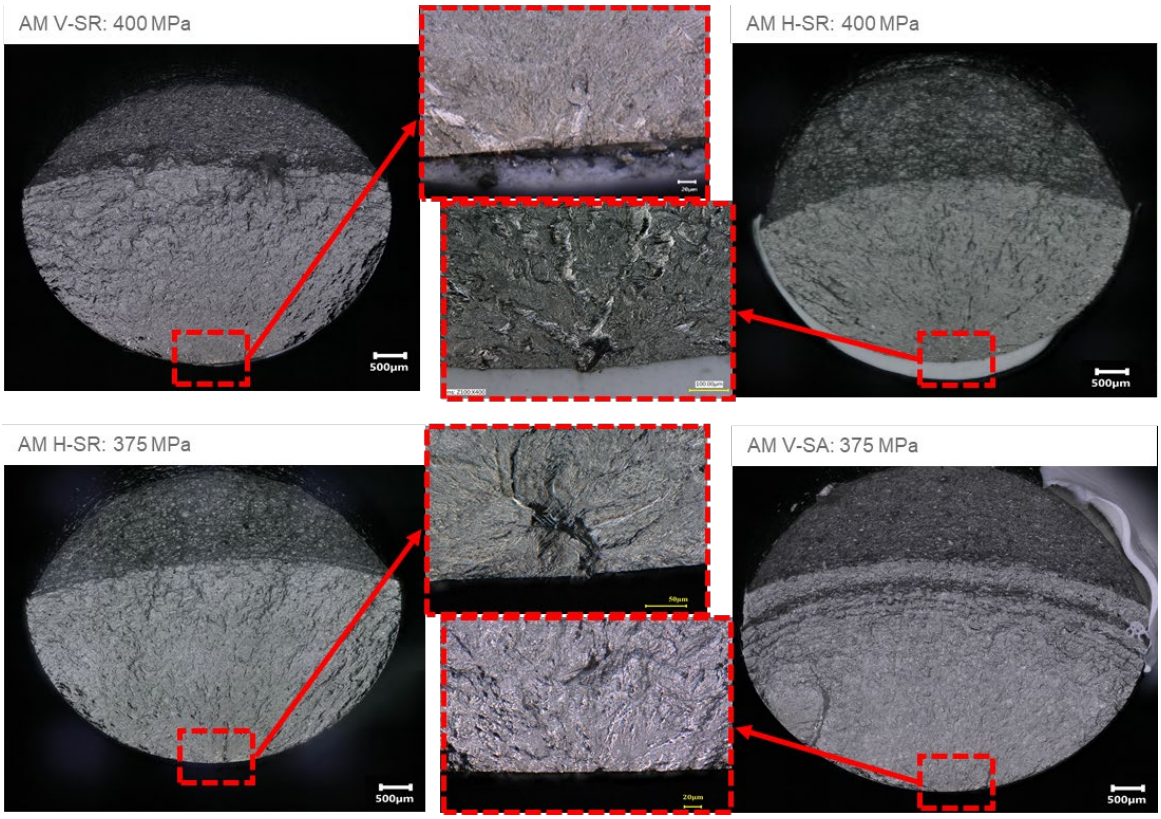

Figure 35: Fracture surfaces from several force controlled fatigue tests for each AM condition.

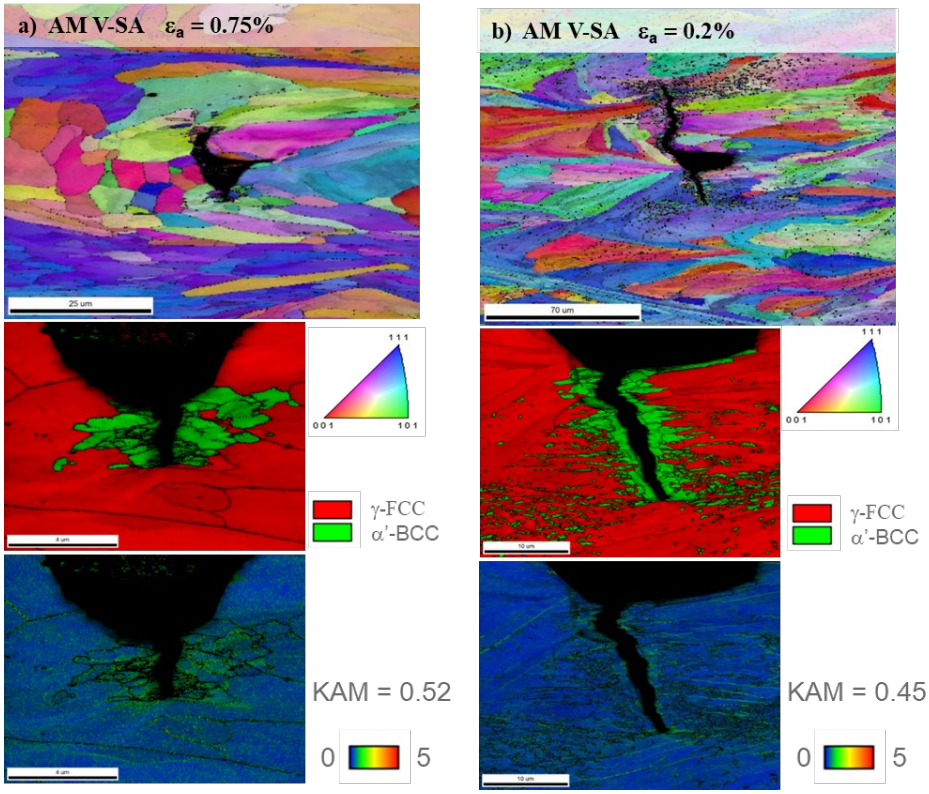

Figure 36: Secondary cracks initiating from defects for AM V-SA specimens tested at a) ε_a = 0.75% and b) ε_a = 0.2%, loading direction is horizontal to the figure.

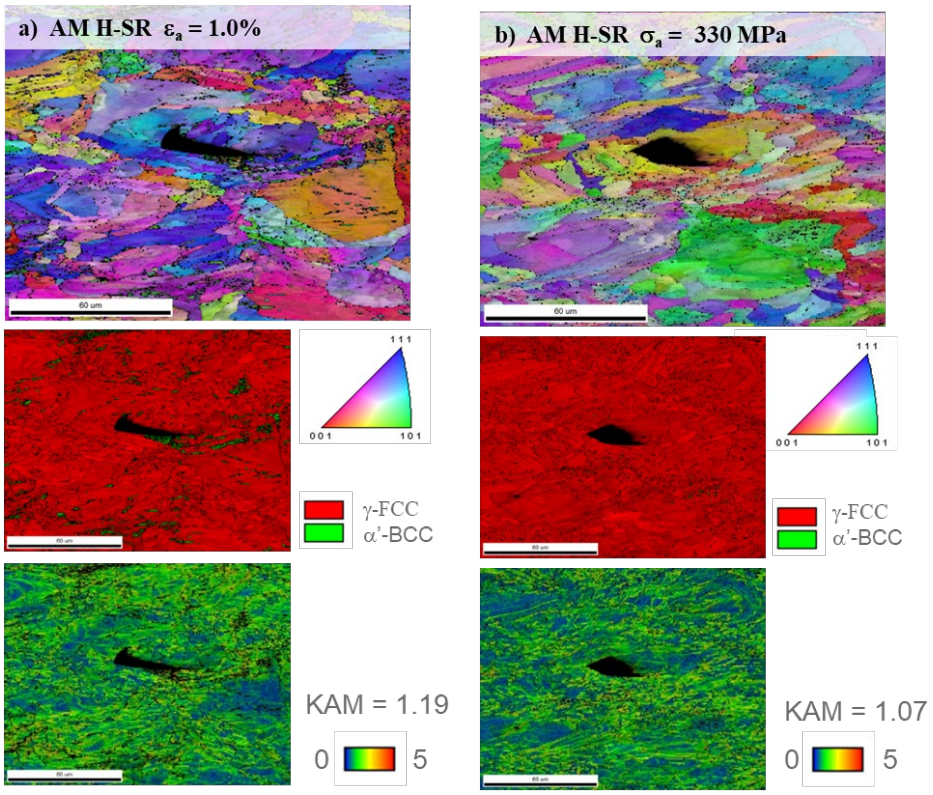

Figure 37: Representative defects in the AM H-SR specimens tested at a) ε_a = 1.0% and b) σ_a = MPa, loading direction is horizontal to the figure.

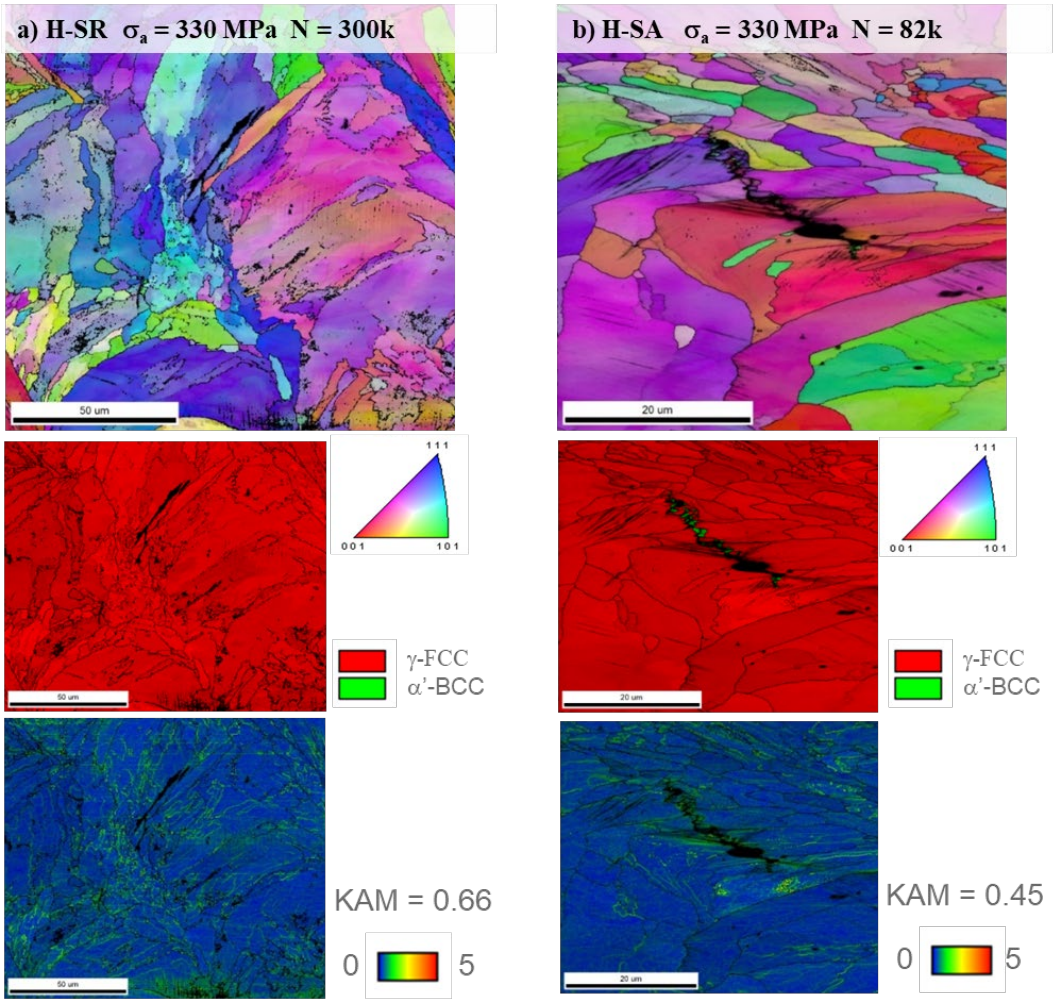

Figure 38: Representative fatigue cracks for AM a) H-SR and b) H-SA specimens, loading direction is horizontal to the figure.

Chapter 6: Summary and Overall Discussion

In this chapter the project objectives and related hypotheses defined in the introduction are revisited individually to detail the findings and significance of the conclusions made in this study. The overall goal of this work is to establish the Process-Structure-Property (PSP) relationships as they affect the fatigue behavior of LB-PBF 304LSS which was accomplished in three main steps: Establishing Structure-Property Relationship of Wrought 304LSS, Establishing Process-Structure Relationship of LB-PBF 304LSS, and finally Establishing Structure-Property Relationship of LB-PBF 304LSS. The need to close knowledge gaps related to the microstructural effects on crack initiation behavior of wrought 304LSS and hone in on an effective design of experiment required initial studies on conventionally process wrought 304LSS. This critical knowledge was then leveraged to elicit the PSP relationships for the LB-PBF material as described in detail in the proceeding sections.

6.1 Structure-Property Relationship of Wrought 304LSS

Objective 1: *Establish Structure-Property Relationships for Wrought 304LSS*

The goal of this objective was to establish the structure-property relationships of a wrought austenitic stainless steel as baseline data for overall goal of establishing the Process-Structure-Property Relationships of LB-PBF 304LSS. Critical information into the mechanisms of failure for conventionally processed conditions is necessary to fully understand the relationship between the unique microstructure of the LB-PBF material and the corresponding fatigue crack behavior. The microstructural effects on the uniaxial fatigue behavior of wrought austenitic stainless steel was characterized through several experimental investigations to understand the

relationship between grain morphology/orientation, deformation behavior, and fatigue failure in order to inform the design of experiments for the LB-PBF material.

Hypothesis 1a: The fatigue behavior of austenitic stainless steels is more sensitive to microstructural features such as grain/twin boundaries, persistent slip bands, and secondary phases than defects such as intermetallic inclusions.

Conclusion 1a:

In Chapter 2, the cyclic rate effects were investigated to understand the relationship between secondary hardening, deformation induced martensitic transformation, and fatigue resistance for low and high cycle fatigue regimes of conventionally processed 304LSS. It was found that the effect of mean strain on the microstructure, cyclic deformation, and fatigue behavior is minimal. The extreme ductility of austenitic stainless steel alloys results in full mean stress relaxation within the first few hundred cycles. The mean strain fatigue specimens also had very similar α' volume fractions after failure as the fully reversed specimens with the same strain amplitude wich resulted in similar secondary hardening behavior of the material.

In addition, it was found that the austenite to martensite transformation in wrought 304LSS can even occur at very low strain amplitudes. The α' phase was observed in fatigue specimens with strain amplitudes as low as 0.25%. The area fraction of α' was correlated to the amount of total secondary hardening and shown to have observable effects on the cyclic deformation behavior of the material. Increases in the strain rate and the corresponding elevated temperature reduces the rate of which secondary hardening occurs. Tests at lower strain rates experienced less adiabitic heating and exhibited greater strain hardening behavior than tests at higher strain rates. This is due to the sensitivity of martensite formation to the adiabatic heating under cyclic loading in the M_s - M_d temperature range. This effect was found to improve the fatigue

resistance for higher strain rate tests, specifically in the low cycle fatigue regime. The stress at failure was essentially the same for similar strain amplitudes, and thus, the increase in temperature at higher strain rates resulted in lower rates of secondary hardening, and higher number of reversals needed to reach failure.

These learned Structure-Property relationships for wrought 304LSS and the effect of testing environments provided necessary information to guide the remaining testing procedures aimed at elucidating the Process-Structure-Property relationships of LB-PBF 304LSS. Furthermore, in Chapter 3, the Structure-Property relationships determined in Chapter 2 were leveraged to design ex-situ experimental techniques targeting the crack initiation behavior including crack nucleation and short crack propagation. Through this exhaustive experimental program, the influence of microstructural features on crack initiation was determined for a stress amplitude in the intermediate fatigue regime. It was revealed that even at stress amplitudes within the transition fatigue life regime, twin boundaries and grain boundaries with similar orientation characteristics to Σ3-TB were the leading crack initiation feature despite the presence of DIMT. Once a crack propagated to a size larger than the average grain size, localized plasticity at the crack tip results in martensite formation.

Twin boundaries predominately cracked on the surface at an angle close to 45° to the loading direction while slip bands were nearly perpendicular (90°) to the loading direction. Grain boundary cracks showed a tendency to initiate on the surface at both 45° and 90° in relation to the loading direction. The dominant crack initiation mechanisms resulted in the hypothesis that methods to control specific grain and twin boundaries could lead to significant improvements in the fatigue resistance of austenitic SS. For the case of wrought 304LSS, the limitations of heat treatment and conventional forming mechanisms result in very little grain boundary

control. These challenges can be overcome, however, through AM techniques in which the high solidification rates can result in more direct microstructural control.

The combined results from Chapters 2 & 3 were necessary to elucidate the preferential crack initiation mechanisms as well as the very early stages of microstructurally short crack growth of 304LSS. Fully understanding the deformation behavior of cyclically loaded 304LSS and its effects on crack initiation lead directly to the hypothesis that the fatigue resistance of 304LSS could be improved through minimizing the microstructural features typically responsible for crack initiation.

6.2 Process-Structure Relationship of LB-PBF 304LSS

Objective 2: *Establish Process-Structure Relationships of LB-PBF 304LSS*

The second objective was to establish the Process-Structure relationships of 304LSS alloy fabricated by LB-PBF. Due to the heat treatment limitations of austenitic stainless steels, the wrought material is typically supplied in the solution annealed condition and cold working of the material is required to improve the strength. Strengthening through cold working, however, can lead to severe reductions in ductility, introduce second phases (DIMT), and promote early life fatigue cracking. While other methods exist to improve strength while maintaining high ductility, such as angular extrusion, these methods are costly with limited production volumes. Discoveries into the Structure-Property relationships of wrought 304LSS suggested that LB-PBF may provide the means to fabricate 304LSS with improved mechanical properties, particularly under cyclic loading conditions. The combined effect of AM processing and post-processing parameters on the resulting microstructure were evaluated in Chapters 4 and 5.

Hypothesis 2a: The as-fabricated microstructure of LB-PBF austenitic stainless steels will contain minimal Σ3 boundaries as a result of the high cooling rates.

Conclusion 2a:

The as-fabricated LB-PBF microstructure was found to consist of minimal Σ3-TB and HAGB as a result of the high solidification rates and epitaxial grain growth. This contrasts with the wrought microstructure which was shown to consist of high density of Σ3-TB and HAGB. Despite the columnar grain growth, the grain size is much finer than the conventional wrought 304LSS. In addition, the presence of sub-grain structures and strain gradients within the grains of LB-PBF microstructures provide strengthening mechanisms without costly reductions in ductility.

Hypothesis 2b: Thermal treatments such as solution annealing can be used to recover the AM microstructure to that of the wrought counterpart.

Conclusion 2b: Solution annealing for 1 hour and 3 hours did not recover the AM microstructure similar to the wrought counterpart. The LB-PBF microstructural grain growth was not significant for grains showing greater than 5° misorientation which resulted in similar grain boundary characteristics to the stress relieved or non-heat treated conditions. However, the sub-grain structure did show significant growth indicating the network of dislocations (tilt boundaries) were mostly recovered from the grain interiors. Additionally, the strain gradients within the grains, which are analogous to residual stresses, were reduced. This reduction in strain gradients results in a reduction of geometrically necessary dislocations and fewer obstacles for the dislocations during deformation.

6.3 Structure-Property Relationship of LB-PBF 304LSS

Objective 3: *Structure-Property Relationships of LB-PBF 304LSS*

The third objective aimed to understand the deformation behavior of LB-PBF 304LSS under both force- and strain-controlled fatigue loading. The effect of process induced defects, surface condition, microstructural characteristics, and thermal treatment were considered to firmly affect the monotonic and cyclic mechanical properties of LB-PBF 304LSS.

Hypothesis 3a: The cyclic mechanical properties of the LB-PBF 304LSS in the machined/polished and as-fabricated thermal treatment condition (non-heat treated) will be improved as compared to those of the wrought counterpart.

Conclusion 3a: Chapter 4 revealed that while most AM materials are susceptible to early fatigue failures related to crack initiation at process-induced defects, austenitic SSs can be successfully fabricated via LB-PBF to offer superior strength, ductility, and fatigue resistance compared to their wrought counterparts. Particularly, under stress based fatigue loadings, the improvement in fatigue life was found to be between 1 to 3 orders of magnitude for a given stress amplitude. This type of enhancement in fatigue resistance has not been observed in other AM materials and signifies a shift in the crack initiation mechanisms and how they can be implemented to additively manufacture materials that mechanically out perform their wrought counterparts by leveraging the Process-Structure Property relationships.

Interestingly such improvements in fatigue performance were not observed for strain-life behavior which showed remarkable consistency between specimens fabricated by wrought and LB-PBF methods. To better understand this contrasting behavior between loading types, as well

as further establish the Process-Strucure-Property relationships, several heat treatments were conducted on the LB-PBF material.

Hypothesis 3b: The cyclic mechanical properties will become more comparable to the ones for the wrought counterpart for the LB-PBF specimens that undergo similar post-process thermal treatments.

Conclusion 3b: Solution annealing of LB-PBF 304LSS resulted in reduced stress-life fatigue performance which was more comparable to the wrought counterpart. The shift in fatigue performance, while expected, came with some surprise considering the solution anneal treatment did not result in a similar microstructure compared to the wrought material. Fractography analysis revealed a strong shift from crack initiation at microstructural features to the process-induced defects present in the LB-PBF material. Interestingly, the sensitivity to defects in the solution annealed condition was greater for strain-based fatigue loadings leading to a large amount of secondary cracking. Again, while the fatigue performance under stress-based conditions was greatly affected by the process/post-process, the strain-based testing showed consistent performance across all conditions.

Objective 4: *Avoid the Typical Failure Mechanisms of 304LSS through the Additive Manufacturing Process*

The final objective was to establish the structure-property relationships of the LB-PBF 304LSS through systematic experimental investigation focused on the crack initiation and microstructurally short crack growth behavior. The ex-situ experimental approach established in Chapter 3 was implemented to better understand the crack initiation mechanisms for the unique microstructure of the AM material.

Hypothesis 4a: The crack initiation mechanisms of LB-PBF will be similar to that of the wrought counterparts, however, the shortage of such dominant microstructural features of LB-PBF 304LSS will result in their improved fatigue resistance.

Conclusion 4a: The fatigue resistance of the LB-PBF 304LSS was shown to be comparable or even greater than the wrought counterpart in the as-fabricated or stress relieved condition, and was somewhat related to the lower densities of the typical crack initiation features for this material. The dominant cracks were found to occur preferentially at HAGB and Σ3-TB, however, the minimal densities of these features resulted in improved fatigue resistance. Additionally, the high solidification rate of the LB-PBF material lead to finer grain sizes and high densities of sub-grains and strain gradients. This unique combination of strengthening mechanisms resulted in unprecedented fatigue performance not typically observed for AM materials. The significance of these observations and their impact on additive manufacturing as a viable means to fabricate materials that surpass their conventionally processed counterparts is described in detail in the following future works section.

Chapter 7: Future Works

The true potential of additive manufacturing has been restricted by the effects of process induced defects which has limited the ability to leverage some of the best aspects of this manufacturing technique such as localized thermal input control. This work has laid the foundation to better understand these process-structure-property relationships for LB-PBF 304LSS which is less sensitive to process induced defects and offers early insight into how AM can be an effective tool to fabricate materials with improved mechanical performance.

Conventional wrought manufacturing techniques typically result in a mostly homogenous microstructure, without direct localized control. This is not particularly beneficial to part performance as components, even in the simplest of cases, are often complex in addition to the complicated real world service loading conditions. These behaviors often lead to areas of stress concentrations as well as stresses that are multiaxial in nature. The ability to recognize critical locations in fatigue and fracture critical components and functionally grade the microstructure to provide improved fatigue performance can lead to the design and fabrication of components that are inherently safer and more reliable.

More in-depth studies focusing on various process/post-process effects on the resulting microstructure, dislocation density, and deformation characteristics as well as the local behavior at notches and under more realistic loading are needed to fully establish an effective process window for LB-PBF 304LSS. The following sections lay out some of the natural research progressions from this work to address some of the previously mentioned needs.

7.1 Tailored Microstructures for Functionally Graded Parts

The natural progression of this work is to translate these findings to take advantage of the intimate relationship between thermal history and local microstructure to fabricate tailored

microstructures or even functionally graded parts. The interactions between the feedstock and process conditions with the resulting microstructure offers the ability to adjust microstructure locally, which has not been available through conventional manufacturing processes. The incident energy density and the local microstructure are intimately related such that AM methods have the capability of direct control of the microstructure. Previous works on LB-PBF Ti-6Al-4V have shown that this type of microstructural control is indeed obtainable and advantageous for improving the mechanical performance of the material [6].

Understanding these Process-Structure relationships can provide the capability to fabricate parts with various grain morphologies aimed at improving the microstructure in respect to the loading condition. Establishing the design space in which LB-PBF is capable of altering/controlling the microstructure without adversely affecting the mechanical performance is necessary. After determining the allowed design space and the microstructures attainable through the LB-PBF process, the effects of these microstructures on mechanical performance can be further evaluated. Based on these evaluations, a database of Process-Structure-Property results can be generated, ultimately leading to the ability to select process conditions for a desired mechanical performance.

After fully understanding the PSP relationships, the true potential of AM may be realized and this can be exemplified through the fabrication of tailored microstructures and functionally graded parts. Increasing or decreasing the incident energy density can lead to lower/higher cooling rates which in turn can lead to coarser/finer microstructures, respectively. For cases such as high cycle fatigue, where the fatigue life is dominated by crack initiation, a finer microstructure and reduced slip length can lead to improved crack initiation resistance translating to higher fatigue strengths. On the other hand, for areas where resistance to crack growth is more critical, the

parameters can be adjusted to give a coarser microstructure which is more capable of deflecting a propagating crack.

While the ability to tailor the microstructures in-situ is a lofty goal for AM, the results of this work suggest that this type of fabrication for performance is achievable through additive manufacturing. It is important, however, not to downplay the effect of internal porosity which is also intimately related to the local thermal input. Deviating outside of an effective process window could result in defects dominating the fatigue behavior despite the improved microstructure.

7.2 Local Behavior at Notches

The local behavior at notches is another important consideration for fatigue analysis as actual components are not uniform throughout and can contain several notch features that drive local plastic deformation. As notches are particularly sensitive to crack initiation, notch type fatigue specimens would be prime candidates for more in-depth studies on tailored microstructures/functionally graded parts. By incorporating the Process-Structure understandings (process map for particular microstructures) additional ex-stiu/in-situ studies can be performed to observe the effectiveness of the tailored microstructure at resisting crack initiation and the subsequent crack growth. This study would lend itself to more real world applications and further improve the understanding of Process-Structure-Property relationships of LB-PBF 304LSS.

7.3 Realistic Loading Conditions

Under real world service conditions the loading is almost never as simple as the case of constant amplitude uniaxial loading. In fact, even under uniaxial loading, the stresses at stress concentrators are often multiaxial. This is compounded even further when accounting for the variable loading nature of structural components when in service. As such, understanding how the

material responds to multiaxial and variable amplitude loading is of great concern and one that the unique microstructural evolution of AM may contribute to improved understanding.

Some of the most reliable multiaxial fatigue models consider the critical plane of a material, i.e. the plane that is subjected to the highest stresses. In this regards, AM may offer the ability to fabricate critical parts aligned with the most beneficial microstructural direction or even design of the microstructure to minimize the effect of the loading on the critical plane. For instance aligning the textured microstructure such that the direction with the highest resistance to slip is along the same line as the critical plane of the material. Thus, fabricating multiaxial test specimens with various orientations in respect to the build direction can enlighten the Process-Structure-Property relationships for more realistic loading conditions.

7.4 Fatigue Modeling

The results from this work will also be useful for better understanding the lower scale damage mechanisms to improve simulation packages targeted at these lower scale levels. There are several fatigue modelling approaches that differentiate the microscale from the mesoscale in order to make more accurate predictions on the fatigue behavior of metals. Often these approaches rely on in-depth studies into the physical nature controlling the various micro-scale stages such as crack initiation and microstructurally short crack growth. These fatigue stages, i.e. crack initiation and MSC growth, are challenging to model due to the limited understanding in their development and difficulties in observing these reactions at the respective scales. The work presented in this study provides valuable information to these areas and can drive new studies into modelling the observed behaviors to deliver more accurate predictions and safe product designs.

References

[1] N. Shamsaei, A. Yadollahi, L. Bian, S.M. Thompson, An overview of Direct Laser Deposition for additive manufacturing; Part II: Mechanical behavior, process parameter optimization and control, Additive Manufacturing 8 (2015) 12-35.

[2] S.M. Thompson, L. Bian, N. Shamsaei, A. Yadollahi, An overview of Direct Laser Deposition for additive manufacturing; Part I: Transport phenomena, modeling and diagnostics, Additive Manufacturing 8 (2015) 36-62.

[3] A.J. Sterling, B. Torries, N. Shamsaei, S.M. Thompson, D.W. Seely, Fatigue behavior and failure mechanisms of direct laser deposited Ti–6Al–4V, Materials Science and Engineering: A 655 (2016) 100-112.

[4] A. Yadollahi, N. Shamsaei, Additive manufacturing of fatigue resistant materials: Challenges and opportunities, International Journal of Fatigue 98 (2017) 14-31.

[5] A. Yadollahi, N. Shamsaei, S.M. Thompson, A. Elwany, L. Bian, Effects of building orientation and heat treatment on fatigue behavior of selective laser melted 17-4 PH stainless steel, International Journal of Fatigue 94 (2017) 218-235.

[6] J. Gockel, J. Beuth, K. Taminger, Integrated control of solidification microstructure and melt pool dimensions in electron beam wire feed additive manufacturing of Ti-6Al-4V, Additive Manufacturing 1-4 (2014) 119-126.

[7] P.A. Kobryn, S.L. Semiatin, Microstructure and texture evolution during solidification processing of Ti–6Al–4V, Journal of Materials Processing Technology 135(2) (2003) 330-339.

[8] M. Masoomi, J.W. Pegues, S.M. Thompson, N. Shamsaei, A numerical and experimental investigation of convective heat transfer during laser-powder bed fusion, Additive Manufacturing 22 (2018) 729-745.

[9] J.W. Pegues, Effect of microstructure on the fatigue behavior of type 304L stainless steel including mean strain and cyclic rate effects, Mississippi State University2016.

[10] J.W. Pegues, S. Shao, N. Shamsaei, J. Schneider, R.D. Moser, Cyclic strain rate effect on martensitic transformation and fatigue behavior of an austenitic stainless steel, Fatigue & Fracture of Engineering Materials & Structures (2017) n/a-n/a.

[11] J. Beddoes, J.G. Parr, Introduction to stainless steels, 3, (1999).

[12] J.R. Davis, Stainless steels, ASM international1994.

[13] C. Blochwitz, W. Tirschler, Twin boundaries as crack nucleation sites, Crystal Research and Technology 40(1-2) (2005) 32-41.

[14] A. Heinz, P. Neumann, Crack initiation during high cycle fatigue of an austenitic steel, Acta Metallurgica et Materialia 38(10) (1990) 1933-1940.

[15] J.W. Pegues, M.D. Roach, N. Shamsaei, Influence of microstructure on fatigue crack nucleation and microstructurally short crack growth of an austenitic stainless steel, Materials Science and Engineering: A 707 (2017) 657-667.

[16] M.D. Roach, S.I. Wright, Investigations of twin boundary fatigue cracking in nickel and nitrogen-stabilized cold-worked austenitic stainless steels, Materials Science and Engineering: A 607 (2014) 611-620.

[17] M.D. Roach, S.I. Wright, J.E. Lemons, L.D. Zardiackas, An EBSD based comparison of the fatigue crack initiation mechanisms of nickel and nitrogen-stabilized cold-worked austenitic stainless steels, Materials Science and Engineering: A 586 (2013) 382-391.

[18] I. Roth, M. Kübbeler, U. Krupp, H.-J. Christ, C.-P. Fritzen, Crack initiation and short crack growth in metastable austenitic stainless steel in the high cycle fatigue regime, Procedia Engineering 2(1) (2010) 941-948.

[19] P. Villechaise, L. Sabatier, J. Girard, On slip band features and crack initiation in fatigued 316L austenitic stainless steel: Part 1: Analysis by electron back-scattered diffraction and atomic force microscopy, Materials Science and Engineering: A 323(1-2) (2002) 377-385.

[20] M.D. Sangid, The physics of fatigue crack initiation, International Journal of Fatigue 57 (2013) 58-72.

[21] M. Michiuchi, H. Kokawa, Z. Wang, Y. Sato, K. Sakai, Twin-induced grain boundary engineering for 316 austenitic stainless steel, Acta materialia 54(19) (2006) 5179-5184.

[22] M. Shimada, H. Kokawa, Z. Wang, Y. Sato, I. Karibe, Optimization of grain boundary character distribution for intergranular corrosion resistant 304 stainless steel by twin-induced grain boundary engineering, Acta Materialia 50(9) (2002) 2331-2341.

[23] J. Armijo, Intergranular corrosion of nonsensitized austenitic stainless steels, Corrosion 24(1) (1968) 24-30.

[24] E.L. Hall, C.L. Briant, Chromium depletion in the vicinity of carbides in sensitized austenitic stainless steels, Metallurgical Transactions A 15(5) (1984) 793-811.

[25] M. Milad, N. Zreiba, F. Elhalouani, C. Baradai, The effect of cold work on structure and properties of AISI 304 stainless steel, Journal of Materials Processing Technology 203(1-3) (2008) 80-85.

[26] R. Shrestha, J. Simsiriwong, N. Shamsaei, S.M. Thompson, L. Bian, Effect of Build Orientation on the Fatigue Behavior of Stainless Steel 316L Manufactured via a Laser-Powder Bed Fusion Process, Solid Freeform Fabrication 2016: Proceedings of the 26th Annual International Solid Freeform Fabrication Symposium (2016) 12.

[27] M.S.F. de Lima, S. Sankaré, Microstructure and mechanical behavior of laser additive manufactured AISI 316 stainless steel stringers, Materials & Design 55 (2014) 526-532.

[28] W.E. Luecke, J.A. Slotwinski, Mechanical properties of austenitic stainless steel made by additive manufacturing, Journal of research of the National Institute of Standards and Technology 119 (2014) 398.

[29] P. Ganesh, R. Giri, R. Kaul, P.R. Sankar, P. Tiwari, A. Atulkar, R. Porwal, R. Dayal, L. Kukreja, Studies on pitting corrosion and sensitization in laser rapid manufactured specimens of type 316L stainless steel, Materials & Design 39 (2012) 509-521.

[30] Y. Murakami, Metal fatigue: effects of small defects and nonmetallic inclusions, Academic Press2019.

[31] L. Gardner, The use of stainless steel in structures, Progress in Structural Engineering and Materials 7(2) (2005) 45-55.

[32] G. Gedge, Structural uses of stainless steel — buildings and civil engineering, Journal of Constructional Steel Research 64(11) (2008) 1194-1198.

[33] D. Ye, Investigation of cyclic deformation behavior in the surface layer of 18Cr–8Ni austenitic stainless steel based on Vickers microhardness measurement, Materials Chemistry and Physics 93(2) (2005) 495-503.

[34] G. Baudry, A. Pineau, Influence of strain-induced martensitic transformation on the low-cycle fatigue behavior of a stainless steel, Materials Science and Engineering 28(2) (1977) 229-242.

[35] M. Bayerlein, H.-J. Christ, H. Mughrabi, Plasticity-induced martensitic transformation during cyclic deformation of AISI 304L stainless steel, Materials Science and Engineering: A 114 (1989) L11-L16.

[36] J. Colin, A. Fatemi, S. Taheri, Cyclic hardening and fatigue behavior of stainless steel 304L, Journal of Materials Science 46(1) (2011) 145-154.

[37] S. Hecker, M. Stout, K. Staudhammer, J. Smith, Effects of strain state and strain rate on deformation-induced transformation in 304 stainless steel: Part I. Magnetic measurements and mechanical behavior, Metallurgical Transactions A 13(4) (1982) 619-626.

[38] D. Hennessy, G. Steckel, C. Altstetter, Phase transformation of stainless steel during fatigue, Metallurgical Transactions A 7(3) (1976) 415-424.

[39] F. Lecroisey, A. Pineau, Martensitic transformations induced by plastic deformation in the Fe-Ni-Cr-C system, Metallurgical and Materials Transactions B 3(2) (1972) 391-400.

[40] J.A. Lichtenfeld, C.J. Van Tyne, M.C. Mataya, Effect of strain rate on stress-strain behavior of alloy 309 and 304L austenitic stainless steel, Metallurgical and Materials Transactions A 37(1) (2006) 147-161.

[41] L. Murr, K. Staudhammer, S. Hecker, Effects of strain state and strain rate on deformation-induced transformation in 304 stainless steel: Part II. Microstructural study, Metallurgical Transactions A 13(4) (1982) 627-635.

[42] G.B. Olson, M. Cohen, A mechanism for the strain-induced nucleation of martensitic transformations, Journal of the Less Common Metals 28(1) (1972) 107-118.

[43] A.G. Pineau, R.M. Pelloux, Influence of strain-induced martensitic transformations on fatigue crack growth rates in stainless steels, Metallurgical Transactions 5(5) (1974) 1103-1112.

[44] J. Venables, The martensite transformation in stainless steel, The Philosophical Magazine: A Journal of Theoretical Experimental and Applied Physics 7(73) (1962) 35-44.

[45] T. Angel, Formation of martensite in austenitic stainless steels, J. Iron Steel Inst. 177 (1954) 165-174.

[46] G. Eickleman, F. Hull, The Effects of Composition on the Temperature of Spontaneous Transformation of Austenite to Martensite in 18/8 Type Stainless Steels, Trans. Am. Soc. Metals 45 (1953) 77-104.

[47] J. Patel, M. Cohen, Criterion for the action of applied stress in the martensitic transformation, Acta metallurgica 1(5) (1953) 531-538.

[48] G. Huang, D. Matlock, G. Krauss, Martensite formation, strain rate sensitivity, and deformation behavior of type 304 stainless steel sheet, Metallurgical transactions A 20(7) (1989) 1239-1246.

[49] R.I. Stephens, A. Fatemi, R.R. Stephens, H.O. Fuchs, Metal Fatigue in Engineering, John Wiley & Sons2000.

[50] G.B. Olson, M. Cohen, Kinetics of strain-induced martensitic nucleation, Metallurgical Transactions A 6(4) (1975) 791.

[51] D. Ye, S. Matsuoka, N. Nagashima, N. Suzuki, The low-cycle fatigue, deformation and final fracture behaviour of an austenitic stainless steel, Materials Science and Engineering: A 415(1–2) (2006) 104-117.

[52] Standard Test Method for Strain-Controlled Fatigue Testing.

[53] Y. Shen, X. Li, X. Sun, Y. Wang, L. Zuo, Twinning and martensite in a 304 austenitic stainless steel, Materials Science and Engineering: A 552 (2012) 514-522.

[54] J. Colin, A. Fatemi, S. Taheri, Fatigue behavior of stainless steel 304L including strain hardening, prestraining, and mean stress effects, Journal of Engineering Materials and Technology 132(2) (2010) 021008.

[55] K. Tsuzaki, T. Maki, I. Tamura, KINETICS OF α'-MARTENSITE FORMATION DURING FATIGUE DEFORMATION IN METASTABLE AUSTENITIC STAINLESS STEEL, Le Journal de Physique Colloques 43(C4) (1982) C4-423-C4-428.

[56] H. Chamati, N.I. Papanicolaou, Y. Mishin, D.A. Papaconstantopoulos, Embedded-atom potential for Fe and its application to self-diffusion on Fe(100), Surface Science 600(9) (2006) 1793-1803.

[57] G.E. Dieter, Mechanical Metallurgy, 3rd ed., McGraw-Hill, Bostan, MA, 1986.

[58] K. Tokaji, T. Ogawa, The growth behaviour of microstructurally small fatigue cracks in metals, ESIS 13 (1992).

[59] F. Hahnenberger, M. Smaga, D. Eifler, Microstructural investigation of the fatigue behavior and phase transformation in metastable austenitic steels at ambient and lower temperatures, International Journal of Fatigue 69 (2014) 36-48.

[60] U. Krupp, I. Roth, H.J. Christ, M. Kübbeler, C.P. Fritzen, In situ SEM observation and analysis of martensitic transformation during short fatigue crack propagation in metastable austenitic steel, Advanced Engineering Materials 12(4) (2010) 255-261.

[61] J.M. Moyer, G.S. Ansell, The volume expansion accompanying the martensite transformation in iron-carbon alloys, Metallurgical Transactions A 6(9) (1975) 1785.

[62] J.J. Roa, G. Fargas, E. Jiménez-Piqué, A. Mateo, Deformation mechanisms induced under high cycle fatigue tests in a metastable austenitic stainless steel, Materials Science and Engineering: A 597 (2014) 232-236.

[63] J. Dash, H.M. Otte, The martensite transformation in stainless steel, Acta Metallurgica 11(10) (1963) 1169-1178.

[64] P.M. Kelly, The martensite transformation in steels with low stacking fault energy, Acta Metallurgica 13(6) (1965) 635-646.

[65] S. Suresh, R.O. Ritchie, Near-Threshold Fatigue Crack Propagation: A Perspective on the Role of Crack Closure, Brown Univ., Providence, RI (USA). Div. of Engineering; Lawrence Berkeley Lab., CA (USA), 1983.

[66] Z.J. Zhang, P. Zhang, L.L. Li, Z.F. Zhang, Fatigue cracking at twin boundaries: Effects of crystallographic orientation and stacking fault energy, Acta Materialia 60(6–7) (2012) 3113-3127.

[67] S.I. Wright, D.P. Field, Recent studies of local texture and its influence on failure, Materials Science and Engineering: A 257(1) (1998) 165-170.

[68] H.-F. Chai, C. Laird, Mechanisms of cyclic softening and cyclic creep in low carbon steel, Materials Science and Engineering 93 (1987) 159-174.

[69] A. Kelly, K.M. Knowles, Crystallography and Crystal Defects, John Wiley & Sons2012.

[70] P.L. Mangonon, G. Thomas, The martensite phases in 304 stainless steel, Metallurgical Transactions 1(6) (1970) 1577-1586.

[71] R. Lagneborgj, The martensite transformation in 18% Cr-8% Ni steels, Acta Metallurgica 12(7) (1964) 823-843.

[72] K.S. Chan, Roles of microstructure in fatigue crack initiation, International Journal of Fatigue 32(9) (2010) 1428-1447.

[73] D.L. McDowell, K. Gall, M.F. Horstemeyer, J. Fan, Microstructure-based fatigue modeling of cast A356-T6 alloy, Engineering Fracture Mechanics 70(1) (2003) 49-80.

[74] S. Pearson, Initiation of fatigue cracks in commercial aluminium alloys and the subsequent propagation of very short cracks, Engineering Fracture Mechanics 7(2) (1975) 235-247.

[75] K. Tanaka, T. Mura, A theory of fatigue crack initiation at inclusions, Metallurgical Transactions A 13(1) (1982) 117-123.

[76] P. Neumann, A. Tonnessen, Cyclic deformation and crack initiation, Fatigue'87 1 (1987) 3-22.

[77] R.E. Hook, J.P. Hirth, The deformation behavior of isoaxial bicrystals of Fe-3%Si, Acta Metallurgica 15(3) (1967) 535-551.

[78] W.H. Kim, C. Laird, Crack nucleation and stage I propagation in high strain fatigue—II. mechanism, Acta Metallurgica 26(5) (1978) 789-799.

[79] P. Zhang, Z.J. Zhang, L.L. Li, Z.F. Zhang, Twin boundary: Stronger or weaker interface to resist fatigue cracking?, Scripta Materialia 66(11) (2012) 854-859.

[80] S.I. Wright, R.J. Larsen, Extracting twins from orientation imaging microscopy scan data, Journal of Microscopy 205(3) (2002) 245-252.

[81] L.L. Li, P. Zhang, Z.J. Zhang, H.F. Zhou, S.X. Qu, J.B. Yang, Z.F. Zhang, Strain localization and fatigue cracking behaviors of Cu bicrystal with an inclined twin boundary, Acta Materialia 73 (2014) 167-176.

[82] Y.-J. Liang, D. Liu, H.-M. Wang, Microstructure and mechanical behavior of commercial purity Ti/Ti–6Al–2Zr–1Mo–1V structurally graded material fabricated by laser additive manufacturing, Scripta Materialia 74 (2014) 80-83.

[83] S. Tammas-Williams, I. Todd, Design for additive manufacturing with site-specific properties in metals and alloys, Scripta Materialia 135 (2017) 105-110.

[84] M. Seifi, M. Gorelik, J. Waller, N. Hrabe, N. Shamsaei, S. Daniewicz, J.J. Lewandowski, Progress towards metal additive manufacturing standardization to support qualification and certification, Jom 69(3) (2017) 439-455.

[85] P. Li, D. Warner, J. Pegues, M. Roach, N. Shamsaei, N. Phan, Towards predicting differences in fatigue performance of laser powder bed fused Ti-6Al-4V coupons from the same build, International Journal of Fatigue 126 (2019) 284-296.

[86] H. Masuo, Y. Tanaka, S. Morokoshi, H. Yagura, T. Uchida, Y. Yamamoto, Y. Murakami, Influence of defects, surface roughness and HIP on the fatigue strength of Ti-6Al-4V manufactured by additive manufacturing, International Journal of Fatigue 117 (2018) 163-179.

[87] S. Romano, A. Brückner-Foit, A. Brandão, J. Gumpinger, T. Ghidini, S. Beretta, Fatigue properties of AlSi10Mg obtained by additive manufacturing: Defect-based modelling and prediction of fatigue strength, Engineering Fracture Mechanics 187 (2018) 165-189.

[88] R. Shrestha, N. Shamsaei, M. Seifi, N. Phan, An investigation into specimen property to part performance relationships for laser beam powder bed fusion additive manufacturing, Additive Manufacturing 29 (2019) 100807.

[89] Y. Yamashita, T. Murakami, R. Mihara, M. Okada, Y. Murakami, Defect analysis and fatigue design basis for Ni-based superalloy 718 manufactured by selective laser melting, International Journal of Fatigue 117 (2018) 485-495.

[90] P. Neumann, A. Tonnessen, Cyclic deformation and crack initiation, Fatigue'87. 1 (1987) 3-22.

[91] M. Roach, S. Wright, Investigations of twin boundary fatigue cracking in nickel and nitrogen-stabilized cold-worked austenitic stainless steels, Materials Science and Engineering: A 607 (2014) 611-620.

[92] M. Roach, S. Wright, J. Lemons, L. Zardiackas, An EBSD based comparison of the fatigue crack initiation mechanisms of nickel and nitrogen-stabilized cold-worked austenitic stainless steels, Materials Science and Engineering: A 586 (2013) 382-391.

[93] J.P. Hirth, The influence of grain boundaries on mechanical properties, Metallurgical Transactions 3(12) (1972) 3047-3067.

[94] P.D. Nezhadfar, A. Zarei-Hanzaki, S.S. Sohn, H.R. Abedi, The microstructure evolution and room temperature deformation behavior of ferrite-based lightweight steel, Materials Science and Engineering: A 665 (2016) 10-16.

[95] T. Richeton, I. Tiba, S. Berbenni, O. Bouaziz, Analytical expressions of incompatibility stresses at Σ3⟨ 111⟩ twin boundaries and consequences on single-slip promotion parallel to twin plane, Philosophical Magazine 95(1) (2015) 12-31.

[96] L. Li, P. Zhang, Z. Zhang, H. Zhou, S. Qu, J. Yang, Z. Zhang, Strain localization and fatigue cracking behaviors of Cu bicrystal with an inclined twin boundary, Acta Materialia 73 (2014) 167-176.

[97] K. Abd-Elghany, D. Bourell, Property evaluation of 304L stainless steel fabricated by selective laser melting, Rapid Prototyping Journal 18(5) (2012) 420-428.

[98] B.M. Morrow, T.J. Lienert, C.M. Knapp, J.O. Sutton, M.J. Brand, R.M. Pacheco, V. Livescu, J.S. Carpenter, G.T. Gray, Impact of defects in powder feedstock materials on microstructure of 304L and 316L stainless steel produced by additive manufacturing, Metallurgical and Materials Transactions A 49(8) (2018) 3637-3650.

[99] A. Standard, E606-92," Standard Practice for Strain-Controlled Fatigue Testing," Annual Book of ASTM Standards 3 (2004).

[100] J. Pegues, K. Leung, A. Keshtgar, L. Airoldi, N. Apetre, N. Iyyer, N. Shamsaei, EFFECT OF PROCESS PARAMETER VARIATION ON MICROSTRUCTURE AND MECHANICAL PROPERTIES OF ADDITIVELY MANUFACTURED TI-6AL-4V, Solid Freeform Fabrication 2017: Proceedings of the 28th Annual International (2017) 14.

[101] N. Raghavan, S. Simunovic, R. Dehoff, A. Plotkowski, J. Turner, M. Kirka, S. Babu, Localized melt-scan strategy for site specific control of grain size and primary dendrite arm spacing in electron beam additive manufacturing, Acta Materialia 140 (2017) 375-387.

[102] Z. Sun, X. Tan, S.B. Tor, C.K. Chua, Simultaneously enhanced strength and ductility for 3D-printed stainless steel 316L by selective laser melting, NPG Asia Materials 10(4) (2018) 127.

[103] J. Pegues, S. Shao, N. Shamsaei, J. Schneider, R. Moser, Cyclic strain rate effect on martensitic transformation and fatigue behaviour of an austenitic stainless steel, Fatigue & Fracture of Engineering Materials & Structures 40(12) (2017) 2080-2091.

[104] E. Astm, 8: Standard Test Method for Tensile Testing of Metallic Materials, Annual book of ASTM standards 3 (1997).

[105] A. Fatemi, R. Molaei, J. Simsiriwong, N. Sanaei, J. Pegues, B. Torries, N. Phan, N. Shamsaei, Fatigue behaviour of additive manufactured materials: An overview of some recent experimental studies on Ti-6Al-4V considering various processing and loading direction effects, Fatigue & Fracture of Engineering Materials & Structures 42(5) (2019) 991-1009.

[106] J.M. Jeon, J.M. Park, J.-H. Yu, J.G. Kim, Y. Seong, S.H. Park, H.S. Kim, Effects of microstructure and internal defects on mechanical anisotropy and asymmetry of selective laser-melted 316L austenitic stainless steel, Materials Science and Engineering: A 763 (2019) 138152.

[107] M. Filippini, S. Beretta, L. Patriarca, G. Pasquero, S. Sabbadini, Defect tolerance of a gamma titanium aluminide alloy, Procedia Engineering 10 (2011) 3677-3682.

[108] P. Li, D. Warner, J. Pegues, M. Roach, N. Shamsaei, N. Phan, Investigation of the Mechanism by which Hot Isostatic Pressing Improves the Fatigue Performance of Powder Bed Fused Ti-6Al-4V, International Journal of Fatigue (2018).

[109] L. Patriarca, M. Filippini, S. Beretta, Digital image correlation-based analysis of strain accumulation on a duplex γ-TiAl, Intermetallics 75 (2016) 42-50.

[110] A.B. Spierings, T.L. Starr, K. Wegener, Fatigue performance of additive manufactured metallic parts, Rapid Prototyping Journal 19(2) (2013) 88-94.

[111] S. Beretta, S. Romano, A comparison of fatigue strength sensitivity to defects for materials manufactured by AM or traditional processes, International Journal of Fatigue 94 (2017) 178-191.

[112] S. Siddique, M. Imran, M. Rauer, M. Kaloudis, E. Wycisk, C. Emmelmann, F. Walther, Computed tomography for characterization of fatigue performance of selective laser melted parts, Materials & Design 83 (2015) 661-669.

[113] E. Wycisk, A. Solbach, S. Siddique, D. Herzog, F. Walther, C. Emmelmann, Effects of Defects in Laser Additive Manufactured Ti-6Al-4V on Fatigue Properties, Physics Procedia 56 (2014) 371-378.

[114] N.T. Aboulkhair, I. Maskery, C. Tuck, I. Ashcroft, N.M. Everitt, Improving the fatigue behaviour of a selectively laser melted aluminium alloy: Influence of heat treatment and surface quality, Materials & Design 104 (2016) 174-182.

[115] P. Li, D. Warner, J. Pegues, M. Roach, N. Shamsaei, N. Phan, Investigation of the mechanisms by which hot isostatic pressing improves the fatigue performance of powder bed fused Ti-6Al-4V, International Journal of Fatigue 120 (2019) 342-352.

[116] M. Muhammad, J.W. Pegues, N. Shamsaei, M. Haghshenas, Effect of heat treatments on microstructure/small-scale properties of additive manufactured Ti-6Al-4V, The International Journal of Advanced Manufacturing Technology (2019) 1-12.

[117] S. Shao, M.J. Mahtabi, N. Shamsaei, S.M. Thompson, Solubility of argon in laser additive manufactured α-titanium under hot isostatic pressing condition, Computational Materials Science 131 (2017) 209-219.

[118] A. Riemer, S. Leuders, M. Thöne, H. Richard, T. Tröster, T. Niendorf, On the fatigue crack growth behavior in 316L stainless steel manufactured by selective laser melting, Engineering Fracture Mechanics 120 (2014) 15-25.

[119] S. Leuders, T. Lieneke, S. Lammers, T. Tröster, T. Niendorf, On the fatigue properties of metals manufactured by selective laser melting – The role of ductility, Journal of Materials Research 29(17) (2014) 1911-1919.

[120] E. Liverani, S. Toschi, L. Ceschini, A. Fortunato, Effect of selective laser melting (SLM) process parameters on microstructure and mechanical properties of 316L austenitic stainless steel, Journal of Materials Processing Technology 249 (2017) 255-263.

[121] J.W. Pegues, M.D. Roach, N. Shamsaei, Additive Manufacturing of Fatigue Resistant Austenitic Stainless Steels by Understanding Process-Structure-Property Relationships, Material Research Letters (2019 (Accepted)).

[122] Standard Practice for Conducting Force Controlled Constant Amplitude Axial Fatigue Tests of Metallic Materials.

[123] C. Man, Z. Duan, Z. Cui, C. Dong, D. Kong, T. Liu, S. Chen, X. Wang, The effect of sub-grain structure on intergranular corrosion of 316L stainless steel fabricated via selective laser melting, Materials Letters 243 (2019) 157-160.

[124] F. Humphreys, A unified theory of recovery, recrystallization and grain growth, based on the stability and growth of cellular microstructures—I. The basic model, Acta Materialia 45(10) (1997) 4231-4240.